Dissolution corrosion of 316L austenitic stainless steels in contact with static liquid lead-bismuth eutectic (LBE) at 500 °C

Manuscript Details

Manuscript number	JNM_2016_324
Title	Dissolution corrosion of 316L austenitic stainless steels in contact with static liquid lead-bismuth eutectic (LBE) at 500degC
Article type	Full Length Article

Abstract

This work addresses the dissolution corrosion behaviour of 316L austenitic stainless steels. For this purpose, solution-annealed and cold-deformed 316L steels were simultaneously exposed to oxygen-poor (< 10-8 mass%) static liquid lead-bismuth eutectic (LBE) for 253-3282 h at 500C. Corrosion was consistently more severe for the cold-drawn steels than the solution-annealed steel, indicating the importance of the steel thermomechanical state. The thickness of the dissolution-affected zone was non-uniform, and sites of locally-enhanced dissolution were occasionally observed. The progress of LBE dissolution attack was promoted by the interplay of certain steel microstructural features (grain boundaries, deformation twin laths, precipitates) with the dissolution corrosion process. The identified dissolution mechanisms were selective leaching leading to steel ferritization, and non-selective leaching; the latter was mainly observed in the solution-annealed steel. The maximum corrosion rate decreased with exposure time and was found to be inversely proportional to the depth of dissolution attack.

Manuscript category	Structural materials
Corresponding Author	Konstantina Lambrinou
Order of Authors	Konstantina Lambrinou, Evangelia Charalampopoulou, Tom Van der Donck, Rémi Delville, Dominique Schryvers
Suggested reviewers	Alfons Weisenburger, Stuart Maloy, Annette Heinzel

Submission Files Included in this PDF

File Name [File Type]

Cover Letter_FINAL.docx [Cover Letter]

Response to Comments on JNM_2016_324_FINAL.docx [Response to Reviewers]

Manuscript_MARKED-UP_FINAL.docx [Revised Manuscript with Changes Marked]

GRAPHICAL ABSTRACT_ULTIMATE.docx [Graphical Abstract]

Manuscript_CLEAN_FINAL.docx [Manuscript File]

FIGURE 1_ULTIMATE.docx [Figure]

FIGURE 2_ULTIMATE.docx [Figure]

FIGURE 3_FINAL.docx [Figure]

FIGURE 4_ULTIMATE.docx [Figure]

FIGURE 5_ULTIMATE.docx [Figure]

FIGURE 6_ULTIMATE.docx [Figure]

FIGURE 7_ULTIMATE.docx [Figure]

FIGURE 8_ULTIMATE.docx [Figure]

FIGURE 9_ULTIMATE.docx [Figure]

FIGURE 10_ULTIMATE.docx [Figure]

FIGURE 11_ULTIMATE.docx [Figure]

FIGURE 12_ULTIMATE.docx [Figure]

FIGURE 13_ULTIMATE.docx [Figure]

FIGURE 14_ULTIMATE.docx [Figure]

FIGURE 15_ULTIMATE.docx [Figure]

FIGURE 16_ULTIMATE.docx [Figure]

FIGURE 17_ULTIMATE.docx [Figure]

FIGURE 18_ULTIMATE.docx [Figure]

FIGURE 19_ULTIMATE.docx [Figure]

FIGURE 20_ULTIMATE.docx [Figure]

TABLE 1_ULTIMATE.docx [Table]

Highlights_ULTIMATE.docx [Highlights]

To view all the submission files, including those not included in the PDF, click on the manuscript title on your EVISE Homepage, then click 'Download zip file'.

Mol, 01/04/2017

Dear Editor,

We would, hereby, like to submit the 2nd revision of Manuscript JNM_2016_324 entitled: "Dissolution corrosion of 316L austenitic stainless steels in contact with static liquid lead-bismuth eutectic (LBE) at 500°C" to the Journal of Nuclear Materials for publication as regular article. The 2nd revision of Manuscript JNM_2016_324 has addressed all additional comments of Reviewer #2 and implemented the requested minor modifications. The work presented in this Manuscript is original, not considered for publication elsewhere, and sheds new light on diverse aspects of the dissolution corrosion behaviour of 316L austenitic stainless steels exposed to a heavy liquid metal (i.e., oxygen-poor, static liquid LBE). This study is expected to be of interest for researchers dealing with the degradation of stainless steels in contact with heavy liquid metal coolants. The authors hope that the Manuscript will help to illustrate the interplay of the dissolution corrosion process with the steel microstructure, emphasising the importance of the steel thermomechanical history when selecting steels intended for service in heavy liquid metal media. It is the aspiration of the authors to contribute with their findings to the state-of-the-art know-how needed in the deployment of future generation nuclear systems (Gen-IV lead-cooled fast reactors, fusion) with lead-alloy coolants (Pb, Pb-Bi, Pb-Li), and of other technologies using heavy liquid metals, e.g., concentrated solar power systems. Sincerely yours,

Dr. Konstantina Lambrinou on behalf of all authors

2nd Revision of Manuscript JNM-2016-324

Mol, 01/04/2017

Dear Editor,

Manuscript JNM-2016-324 has been revised for the 2nd time, taking into account the additional recommendations of Reviewer #2. The authors hope that the revised Manuscript meets the high standards of the Journal of Nuclear Materials. The recommendations and remarks made by Reviewer #2 are addressed below point-by-point, using blue characters for clarity. All new changes are highlighted in green in the revised Manuscript, while the changes performed during the 1st revision are highlighted in yellow, so as to facilitate the assessment of the overall revision. Sincerely yours,

Dr. Konstantina Lambrinou on behalf of all authors

Reviewer #2:

The paper was substantially changed and shortened. Unfortunate the authors did not provide a marked up version of the manuscript making it difficult to review all the changes made.
Answer: the authors are grateful for the appreciation of their efforts during the 1st revision of Manuscript JNM-2016-324. However, the authors do not understand the second comment of Reviewer #2, since a marked-up version of the Manuscript has been submitted during the 1st revision. In the marked-up version of the 1st revision, the performed changes were highlighted in yellow. This can be easily confirmed by checking the previous submission (1st revision); therefore, the authors believe that Reviewer #2 must have overlooked the marked-up version of the Manuscript by mistake and has looked at the clean version instead.

Some minor issues should still be consider:
Please provide references for the use of LBE in CSP applications to be consistent with the references for nuclear applications. Also other applications might be listed if such exist to show its wide applications.
Answer: since the Manuscript's primary focus is on heavy liquid metal-cooled nuclear systems, such as the ADS irradiation facility MYRRHA, and not on CSP systems, the addition of a single review article as reference to the use of LBE in CSP applications was deemed sufficient:
L.A. Weinstein, J. Loomis, B. Bhatia, D.M. Bierman, E.N. Wang, G. Chen, Concentrating solar power, Chemical Reviews **115** (2015) 12797-12838
The above article appears as Ref. [6] in the revised Manuscript.

Experimental: Were those actually different heats or just different treatment conditions. I assume the material came from the same heat but 3 different treatments? :" Three different 316L austenitic stainless steel heats (1 solution-annealed, 2 cold-drawn)"? Don't use the word "heats" if you don't mean heats. I assume you mean different thermal mechanical processing? But maybe they are different heats. Please specify.

Answer: This work exposed three different 316L austenitic stainless steel heats to oxygen-poor static LBE at 500°C. This was stated in section '2.1. Materials' as follows: "The solution-annealed heat, henceforth designated 316LSA, was a plate (15 mm thickness; EUROTRANS-DEMETRA heat [52]), solution-annealed in the 1050-1100°C range, followed by a water quench. The cold-drawn heats, henceforth designated 316LH1 and 316LH2, were cylindrical rods (∅ 10 mm): 316LH1 was solution-annealed at 1060°C for 4 h and water-quenched prior to cold deformation, while the heat treatment of 316LH2 was not provided by the steel supplier." Solution-annealed heat 316LSA was supplied by Industeel, ArcelorMittal, S.A.; cold-drawn heat 316LH1 was supplied by Aceros Inoxidables OLARRA, S.A.; and 316LH2 cold-drawn heat was supplied by Sidero Staal nv. In order to emphasise that this work used 3 different steel heats, the three steel suppliers are also mentioned in the revised Manuscript.

This statement is confusing: "α-ferrite is the product of the low-temperature transformation (727-738°C) of δ-ferrite, which forms at high temperatures (>1394°C), but is retained in the steel microstructure, even after the solution annealing treatment, in the form of its low-temperature counterpart α-ferrite [53,54]."
Why not say you found ferrite (no alpha and delta) and say it is likely retained from the high temperature delta phase and called delta ferrite.
Answer: This phrase has been revised as follows: "α-ferrite results from the low-temperature (727-738°C) transformation of its high-temperature (>1394°C) polymorph δ-ferrite that is retained in the steel microstructure even after the solution annealing treatment [54,55]".

The question remains why only the solution annealed materials shows it?
If it is indeed from the high temperature regime why don't the other materials show it?
Answer: As mentioned in the answer to an earlier comment, this work exposed three steel heats to oxygen-poor static LBE at 500°C. The fact that ferrite appears only in the solution-annealed 316LSA heat and not in the cold-drawn 316LH1 & 316LH2 heats reflects differences in the steel production and might be associated with local compositional inhomogeneities that are more common in industrial-size steel heats such as the EUROTRANS-DEMETRA (316LSA) heat. The fact that ferrite is absent from the 316LH1 & 316LH2 heats, while it is present in the 316LSA heat, is additional evidence of the use of 3 different steel heats in this study.

Please label the twin interface in Figure 3d so it is clear where your dislocations pile up.
Answer: Fig. 3d has been labelled with twin boundaries (interfaces) and slip plane directions.

Also how do you know those are not also twins?
Answer: Those are not twins for two reasons: (a) they do not show additional reflections in diffraction, and (b) the dislocation pile-up only becomes visible (unlike twin interfaces) – as depicted here – by slightly tilting the beam off a main zone axis orientation to approach an orientation where some dislocations satisfy the extinction rule ($\vec{g} \cdot \vec{b} = 0$). Moreover, twins are also not known to crisscross along consecutive slip planes, as shown in Fig. 3d.

Seems figure 3b shows very fine twins and 3d shows a large twin about an order of magnitude different in length?
Answer: This remark is correct: Fig. 3b shows very fine twins, whereas Fig. 3d focuses on a large twinless area bound by two twin boundaries. This has been clarified in the revised Manuscript, both in the text and in the caption of Fig. 3. Indeed, some areas (e.g., the areas surrounding the central twin group in Fig. 3a) may be free of twin interfaces over several micrometers, until one encounters the next twin group. Observing dislocation pile-ups within a fine twin is quite challenging and has not been tried in this work.

Dissolution corrosion of 316L austenitic stainless steels in contact with static liquid lead-bismuth eutectic (LBE) at 500°C

Konstantina Lambrinou[a,*], Evangelia Charalampopoulou[a,b], Tom Van der Donck[c], Rémi Delville[a], Dominique Schryvers[b]

[a] *SCK•CEN, Boeretang 200, 2400 Mol, Belgium*

[b] *University of Antwerp, Electron Microscopy for Materials Science (EMAT), Groenenborgerlaan 171, 2020 Antwerpen, Belgium*

[c] *KU Leuven, Department of Materials Engineering, Kasteelpark Arenberg 44, 3001 Leuven, Belgium*

* Corresponding author. Address: SCK•CEN, Boeretang 200, B-2400 Mol, Belgium. Tel.: +32-14-333164. *E-mail address*: klambrin@sckcen.be (K. Lambrinou).

Abstract

This work addresses the dissolution corrosion behaviour of 316L austenitic stainless steels. For this purpose, solution-annealed and cold-deformed 316L steels were simultaneously exposed to oxygen-poor (< 10^{-8} mass%) static liquid lead-bismuth eutectic (LBE) for 253-3282 h at 500°C. Corrosion was consistently more severe for the cold-drawn steels than the solution-annealed steel, indicating the importance of the steel thermomechanical state. The thickness of the dissolution-affected zone was non-uniform, and sites of locally-enhanced dissolution were occasionally observed. The progress of LBE dissolution attack was promoted by the interplay of certain steel microstructural features (grain boundaries, deformation twin laths, precipitates) with the dissolution corrosion process. The identified dissolution mechanisms were selective leaching leading to steel ferritization, and non-selective leaching; the latter was mainly observed in the solution-annealed steel. The maximum corrosion rate decreased with exposure time and was found to be inversely proportional to the depth of dissolution attack.

Keywords: stainless steel; SEM; TEM; de-alloying; intergranular corrosion; pitting corrosion

1. Introduction

One of the principal challenges in the development of Gen-IV lead-cooled fast reactors (Gen-IV LFRs) is the inherent corrosiveness of the primary heavy liquid metal coolant, such as lead (Pb) and lead-bismuth eutectic (LBE), for structural and cladding candidate steels considered for the construction of such reactor systems [1-5]. The inherent corrosiveness of lead-alloys (Pb, LBE, Pb-Li) is also a concern in fusion (tritium breeding blanket concept), in concentrated solar power (CSP) systems using heavy liquid metals [6], and in accelerator-driven systems (ADS) that use heavy liquid metals as spallation targets. An example of ADS technology currently under development at SCK•CEN, Belgium, is the flexible fast-spectrum irradiation facility MYRRHA (multi-purpose hybrid research reactor for high-tech applications), which will use liquid LBE as primary coolant and spallation target [7]. The mitigation of undesirable liquid metal corrosion (LMC) effects in MYRRHA is based on three main pillars, i.e., moderate operating temperatures (< 450°C), active oxygen control and understanding of the steel-specific LMC mechanisms. Active

oxygen control strives to form a protective oxide scale on the steel surface by dissolving precise amounts of oxygen in the heavy liquid metal (HLM) coolant [3,5,8-10]. The concentration of dissolved oxygen in the HLM must ensure the formation of protective oxides on the steels without oxidising the HLM itself (too high oxygen potential) [11]. If, for any reason, the oxygen potential drops below a certain level, the oxide scales will be reduced and the steel will come into direct contact with the HLM [11]; such eventuality is undesirable, as it will result in the steel dissolution corrosion. Dissolution corrosion of austenitic stainless steels, such as the 316L steel studied in this work, involves the loss of steel alloying elements into the heavy liquid metal and the progressive LBE penetration into the steel [12-18]; moreover, LBE dissolution attack can be locally-enhanced, creating deep 'pits' that might result in the premature breaching of thin-walled components, such as heat exchanger and fuel cladding tubes [12,19,20].

Since the MYRRHA candidate structural steel is the 316L stainless steel, it is important for the development of this system to understand all aspects of the LMC behaviour of the 316L grade, including the dissolution corrosion addressed in this study. The literature survey of the LMC behaviour of 316L and compositionally-similar steels (e.g., 316, 1.4571, 304L) in contact with liquid LBE revealed that, even though dissolution corrosion can occur locally at oxygen-saturated LBE and at temperatures as low as 400°C, it becomes particularly promoted at high temperatures ($T \geq 450$°C) and low LBE oxygen concentrations ($C_O < 10^{-8}$ mass%) [5,12-18,21-49]. Dissolution corrosion at elevated temperatures is promoted because the solubility of the main steel alloying elements (i.e., Ni, Cr, Fe) in the liquid LBE increases with temperature [50]. Low LBE oxygen concentrations favour dissolution corrosion by suppressing the formation of protective oxide scales. Based on the above, this study exposed 316L steels to oxygen-poor, static LBE ($C_O < 10^{-8}$ mass%) at 500°C to ensure the manifestation of dissolution corrosion. Despite the aggressive exposure conditions, the relevance of this study for the development of MYRRHA is manifold: first, one cannot exclude high-temperature transients ($T \geq 500$°C) during the system operation or oxygen-depleted zones of static LBE, i.e., similar service conditions as those tested here; second, the oxide scale might lose its local protectiveness with time due to chemical or mechanical damage, resulting in local dissolution attack [12,13,51,52]; third, the adopted testing approach allows the assessment of the maximum dissolution rate, which is important for establishing safety margins for the reliable use of thin-walled components.

This study aims at the in-depth understanding of the 316L steel dissolution corrosion behaviour in the absence of a protective oxide, an event that cannot be excluded in a real system, at least locally. To make this work relevant for the 316L steel grade and not for a single steel heat only, different heats must be simultaneously exposed to the same exposure conditions, so as to study the effect of the steel thermomechanical state and microstructure on its dissolution corrosion behaviour. This know-how is not only valuable for the optimum design of nuclear systems, such as MYRRHA, but also in view of the scarcity of studies addressing the effect of microstructure and thermomechanical state of the 316L steel grade on its compatibility with LBE.

2. Experimental

2.1. Materials

Three different 316L austenitic stainless steel heats (1 solution-annealed, 2 cold-drawn) were exposed to oxygen-poor static liquid LBE in this work. The solution-annealed heat, henceforth designated 316LSA, was a plate (15 mm thickness; EUROTRANS-DEMETRA heat [53]; Industeel, ArcelorMittal, S.A.) solution-annealed in the 1050-1100°C range, followed by a water quench. The cold-drawn steel heats, henceforth designated 316LH1 (Aceros Inoxidables OLARRA, S.A.) and 316LH2 (Sidero Staal nv), were cylindrical rods (∅ 10 mm): 316LH1 was solution-annealed at 1060°C for 4 h and water-quenched prior to cold deformation, while the heat treatment of 316LH2 was not provided by the steel supplier. Usually, solution annealing of austenitic stainless steels is conducted above 1040°C for short times (several minutes) to bring chromium carbides into solution in the austenite and control grain growth [54]. The degree of cold work of 316LH1 and 316LH2 heats was not provided by the suppliers. Table 1 shows that the chemical compositions of the three heats agreed with the AISI 316L grade specification.

The microstructure of the as-received steel heats was first assessed by light optical microscopy (LOM) on steel specimens that were chemically etched with Carpenters' reagent (8.5 g $FeCl_3$, 2.4 g $CuCl_2$, 122 ml HCl, 6 ml HNO_3, 122 ml ethanol) for ~1 min. LOM images of etched 316LSA, 316LH1 and 316LH2 samples are shown in Fig. 1. The average grain size of the three steels was: 45 μm in 316LH1, 65 μm in 316LH2, and varied locally between 30 and 45 μm in 316LSA. The cold-drawn heats 316LH1 and 316LH2 exhibit deformation twins and other features typical for cold-deformed steels. The solution-annealed 316LSA heat shows δ-ferrite stringers parallel to the rolling direction. The phase composition of the as-received 316L steels was determined by X-ray diffraction (XRD; Seifert 3003, GE), using a Cu *K*α radiation source (operating conditions: 40 kV, 40 mA). The XRD patterns (Fig. 2) were acquired in the 30-90° 2θ range with a step size of 0.02° and a time of 2s per step. The only identified phase in all heats was austenite (face-centred cubic, *fcc*; $Fm\bar{3}m$; JCPDS file: 01-071-4649) except for solution-annealed 316LSA, which contained a small fraction of α-ferrite (body-centred cubic, *bcc*; $Im\bar{3}m$; JCPDS file: 03-065-4899). α-ferrite results from the low-temperature (727-738°C) transformation of its high-temperature (>1394°C) polymorph δ-ferrite that is retained in the steel microstructure even after the solution annealing treatment [54,55]. The term δ-ferrite is herein used to denote the high-temperature origin of this steel precipitate.

The microstructure of the as-received cold-drawn steels was characterised on the nanoscale by means of transmission electron microscopy (TEM). The TEM (JEM-3010, JEOL, Japan) was operated at 300 kV using a side-entry type double tilt specimen holder with angular ranges of ±30°. Samples for TEM investigation were prepared from ∅ 3 mm disks punched out of a thin steel slab (~200 μm). These were mechanically polished to 100-130 μm thickness and

electropolished to perforation in a Struers Tenupol 3 (operating conditions: 30 V, 0.2 A, -40°C), using an electrolyte made of 95% CH_3OH (methanol) and 5% $HClO_4$ (perchloric acid).

Fig. 3 shows the two main modes of plastic deformation encountered in all thin foils extracted from the cold-drawn steels, here illustrated for 316LH2: twin and slip deformations. It is known that 316L austenitic stainless steels are *fcc* alloys with relatively low stacking fault energies [56], allowing easy nucleation of deformation twins. Fig. 3a is a bright field (BF) image of a typical set of fine parallel twins laths, while selected-area diffraction over several twin laths (circle in Fig. 3b) along the <1$\bar{1}$0> orientation showed that the twinning plane is {111} (Fig. 3c), in agreement with the reported twinning mode for an *fcc* lattice. Slip in *fcc* crystals occurs in {111} close-packed planes along <110> directions. Fig. 3d shows dislocation pile-up on the {$\bar{1}$11} and {1$\bar{1}$1} slip planes observed near a <110> direction in a large twinless zone confined between two twin boundaries. Fig. 3e was obtained by beam tilting in the {100} plane slightly off the zone axis orientation, where the high density of diffracting dislocations does not allow clear visualization of the slip planes. The observed orientation, close to a 2-beam condition, allows the visualization of two <110> slip planes, while the third one does not show diffraction contrast, since it satisfies the extinction criterion $\vec{g} \cdot \vec{b} = 0$, where $\vec{g}$ is the diffraction vector and $\vec{b} = a/\sqrt{}$<110> is the Burgers vector for an *fcc* lattice. In conclusion, TEM revealed that the as-received cold-drawn 316LH1 and 316LH2 steels were characterized by a high density of twins and dislocations, with higher dislocation density near twin boundaries. Moreover, the two deformation modes (slip and twinning) occurred along the expected close-packed planes. Since fine-scale twinning leads to steel grain fragmentation, it is expected that twin boundaries act as barrier for dislocation motion, resulting to dislocation pile-up.

2.2. Sample Geometry, Dimensions & Surface Finish

The geometry and dimensions of the 316L steel specimens tested in this study are shown in Fig. 4b. Specimens were connected with each other by screw threads (M3); only the last specimen in each set of specimens per test was without thread on one side to minimize machining. All specimens had the following dimensions: ∅ 9 mm, length 10 mm. The specimens were polished with down to 3 μm diamond paste just prior to testing to reduce the surface roughness caused by machining. Even though a mild near-surface steel deformation induced by polishing cannot be excluded, adopting a standardised polishing procedure ensured that the surface quality of all specimens was comparable. The polished specimens were cleaned with acetone and ethanol in an ultrasonic bath, followed by blow-drying with mildly hot air, before specimen insertion to the LBE bath. The visual specimen impression prior to exposure was that of a mirror finish without any trace of ethanol/acetone drying marks. All tests exposed simultaneously specimens made of the three steel heats used in this work (316LSA, 316LH1, 316LH2); for this purpose, sets of specimens connected to each other were introduced in the test setup from a dedicated opening on the lid (Figs. 4a-4b) by means of an 80 cm-long sample holder made of 316L steel.

2.3. Experimental Setup

A schematic representation of the test setup is presented in Fig. 4a. The setup consisted of a stainless steel autoclave with an inner alumina (Al_2O_3) liner (inner diameter 7.4 cm, height 14.3 cm). The alumina liner prevented the direct contact of the steel walls with the LBE volume used for the steel exposure, avoiding its contamination with steel alloying elements that could decrease the instantaneous steel dissolution rates. A small amount of LBE between autoclave walls and alumina liner ensured good thermal conductivity and better temperature control during testing. The stainless steel autoclave was externally heated and thermally insulated to minimise heat losses. The temperature and LBE oxygen concentration were monitored during testing. A thermocouple type K (not pre-oxidised or otherwise protected) monitored the temperature; this thermocouple was connected to the controller that regulated the LBE temperature during testing. The reliability of its output was compared to the output of a second thermocouple type K that measured the temperature on the walls of the stainless steel autoclave. The second thermocouple was connected to an alarm controller that brought the system to a power-down, if the autoclave temperature exceeded a predefined setpoint. Electrochemical oxygen sensors (Bi/Bi_2O_3 reference electrode) fabricated at SCK•CEN monitored the LBE oxygen concentration; Fig. 4c gives a detailed description of these sensors. The oxygen sensor accuracy was previously evaluated [57,58] and was found to improve with temperature. The three-sigma deviation on the measured by the sensors electric potential difference was about 4 mV [57]. At 500°C, this standard deviation results in ~12% error on the LBE oxygen concentration, which is calculated from the measured by the sensors electric potential difference. The LBE oxygen concentration was calculated using the following equations [57]:

$$\Delta U - \Delta U_{th} = -0.34756 + 2.5217\times10^{-4}\cdot T - 4.3087\times10^{-5}\cdot T\cdot \ln C_O \quad (1)$$

$$\Delta U_{th} = -6.91\times10^{-3} + 1.762\times10^{-5}\cdot T \quad (2)$$

where ΔU is the electric potential difference measured by the oxygen sensor in V, ΔU_{th} is the thermoelectric potential between stainless steel and Mo wire in V, T is the absolute temperature in K, and C_O is the LBE oxygen concentration in mass%.

The autoclave lid had various openings to insert specimens, oxygen sensor, thermocouple, and to allow the inlet/outlet of the conditioning gas (Figs. 4a-4b). Specimen insertion in the LBE bath was done via a dedicated tube welded on the lid, under leak-tight conditions, with the help of a stainless steel valve (1-piece 40 series ball valve; 12 mm Swagelok tube fitting; SS-45S12MM). A pre-oxidized stainless steel tube supplied the reducing conditioning gas at a distance of ~2.5 cm from the steel specimens and close (< 1 cm) to the bottom of the LBE bath. Gas supply close to the bath bottom resulted in mild LBE mixing, making the test conditions 'quasi-static' rather than truly static. The conditioning gas (HYTEC 5: Ar-5%H_2, Rapid Industrial Gases Ltd., UK) was a certified gas made of 95% Ar with 5% H_2 and minor oxygen-containing impurities (O_2 < 10 ppm, H_2O < 10 ppm).

2.4. Exposure Conditions

316L steel specimens were exposed to oxygen-poor (mostly C_O < 10^{-8} mass%), static LBE at 500°C for the following times: 253, 501, 1000, 1003, 2055 and 3282 hours. All tests exposed 4 steel specimens simultaneously (1 specimen per heat plus an additional specimen arbitrarily selected from one of the 3 heats), except for the longest test (3282 h) that tested a set of 9 steel specimens (3 specimens per heat). The distance of the specimens from the bottom of the LBE bath was 1 cm for the longest exposure (3282 h) and 6 cm for all other exposures.

Each test used ~5 kg of 'fresh' LBE, so as to ensure that LBE contamination from an earlier test did not affect the results of the next one. The main impurities in the as-received LBE (analysed as 55.3% Bi, 44.7% Pb) were Si (< 2700 mg/kg), F (< 90 mg/kg), Ag (~19 mg/kg), S (< 9 mg/kg), Cu (~7 mg/kg), Ni (< 3.2 mg/kg), Hg (~2.4 mg/kg), Fe (< 2.4 mg/kg), Nb (< 2.4 mg/kg) and Ge (< 2.1 mg/kg). The ratio of the steel specimen surface to the LBE volume used for testing varied between 0.023 and 0.051 cm^{-1} for the tests that exposed 4 and 9 specimens, respectively. This calculation takes into account the temperature dependence of the LBE density, ρ_{LBE} [1]:

$$\rho_{LBE}\ (kg/m^3) = 11096\text{-}1.3236 \cdot T \quad (3)$$

where T is the absolute temperature in K.

In all tests, the exposure temperature was kept constant at ±2°C from the targeted temperature of 500°C, while continuous purging with Ar-5%H_2 maintained a low LBE oxygen concentration (mostly C_O < 10^{-8} mass%). The evolution of LBE oxygen concentration during all tests is shown in Fig. 5. Since the LBE oxygen concentration varied roughly between 5×10^{-13} and 2×10^{-8} mass% during the performed tests, the formation of certain oxides, such as Cr_2O_3 (stable above 10^{-15} mass% at 500°C [11]) and $FeCr_2O_4$ (stable above 10^{-12} mass% at 500°C [11]), could, in principle, not be excluded. An LBE preconditioning treatment lowered the oxygen concentration below 10^{-8} mass% prior to the insertion of the steel specimens in the LBE bath (Fig. 6). This minimised steel oxidation that would probably delay the occurrence of dissolution corrosion. Despite the low C_O during sample insertion, the immersed steel specimens acted as oxygen getters, further reducing the C_O (Fig. 6), which suggests that steel oxidation was not completely prevented.

2.5. Post-Test Analysis

Metallographic cross-sections were prepared from all exposed 316L steel specimens; a mirror surface finish was achieved by polishing the specimen cross-sections with 1 μm diamond paste in the last step. Some of the polished cross-sections underwent an additional polishing step using a colloidal silica (OPS) suspension, which created a subtle surface relief on the steel cross-sections, facilitating the study of the interplay of the dissolution corrosion process with the steel microstructure by LOM (Axio Scope.A1, ZEISS International). The 316L dissolution corrosion behaviour was primarily studied by LOM, scanning electron microscopy (SEM; JSM-6610LV, JEOL, Japan) and energy dispersive X-ray spectroscopy (EDS; XFlash detector 4010, Bruker AXS GmbH, Germany). A more in-depth study of specific areas involved the deployment of high-resolution

electron backscatter diffraction (EBSD; Hikari XP EBSD camera, EDAX, USA, on a FEI Nova NanoSEM 450, FEI, USA); in select cases, thin foils were made by focused ion beam (FIB; FEI Helios Nanolab 650, FEI, USA) and investigated by TEM (JEM-3010, JEOL, Japan). Corrosion quantification was attempted by measuring (a) the surface recession by LOM, i.e., comparing the initial specimen diameter with the diameter of the unaffected steel, and (b) the thickness of the dissolution-affected zone by SEM. The first method was unsuccessful due to the limited resolution of light optical profilometry that was used to measure the initial specimen diameter. This work reports only on the thickness of the dissolution-affected zone, as measured by SEM on 1-3 cross-sections per specimen. Depending on the time-dependent severity of attack, SEM pictures were taken at magnifications that allowed the accurate quantification of corrosion. The pictures were able to reconstruct the whole cross-section and the thickness of the dissolution-affected zone was measured on many (randomly-chosen) locations per picture. Typically, 200-500 measurements were collected per cross-section to ensure reliable statistics. Apart from the thickness of the dissolution-affected zone, another parameter used to quantify corrosion in this study was the percentage of the steel specimen surface that was affected by dissolution.

3. Results & Discussion

3.1. General Observations of Corrosion Damage

The evolution of damage with exposure time is depicted in the SEM images of Fig. 7 for one of the cold-drawn steels (316LH1; the results were similar to those acquired from 316LH2) and Fig. 8 for the solution-annealed steel 316LSA. The dissolution front, i.e., the interface between the dissolution-affected zone and the unaffected steel, was in general more perturbed in the cold-drawn steel than the solution-annealed one, for all exposure times. Moreover, the cold-drawn steel was more prone to locally-enhanced dissolution attack, exhibiting a non-negligible number of pit-like features similar the one shown in Fig. 7f. Even though these features did not form as the result of conventional pitting corrosion, they will hereafter be referred to as 'pits' due to the fact that the depth of attack at their location was much deeper than the depth of attack in their immediate vicinity. The thickness of the dissolution-affected zone increased with exposure time for all steel heats, as expected. At any exposure time, corrosion was invariably deeper in the cold-drawn steels than in the solution-annealed one, underlying the importance of the steel thermomechanical state. Moreover, the percentage of the steel specimen surface affected by corrosion increased with the exposure time for all steel heats. After 253 h, 90% of the specimen surface of the solution-annealed 316LSA steel and 80% of the cold-drawn 316LH1 and 316LH2 steels was affected by dissolution corrosion. After 501 h, 100% of the specimen surface of the 316LSA and 90% of the 316LH1 and 316LH2 was affected. In all exposures longer than 1000 h, 100% of the surface of all steel specimens was affected by dissolution attack.

Figs. 7 and 8 show that LBE dissolution attack does not progress perpendicular to the specimen surface, but constantly changes direction, following paths of preferential ingress into the base or

unaffected steel. These paths include grain boundaries, deformation twins, and various steel precipitates, the formation and orientation of which is associated with the steel production and deformation processes, respectively. The interplay between the steel microstructure and the dissolution process is largely responsible for the intricacy of the dissolution front and the non-uniform thickness of the dissolution-affected zone. The effect of the steel microstructure on the dissolution corrosion behaviour of 316L steels is extensively addressed in section 3.4.

Differences in the thickness of the dissolution-affected zone were observed on all specimen cross-sections, irrespective of the exposure time and the steel heat. Very often, this thickness was observed to vary significantly over relatively short distances, as shown in Figs. 7a and 7e, suggesting that dissolution attack started at a different moment in areas separated by only a few micrometres. In first instance, differences in the time dissolution attack begins on the steel surface could be associated with the local vulnerability of the oxide scale. Despite the fact the tests performed in this study were designed to promote dissolution corrosion, one cannot assume the complete absence of an oxide film from the steel surface: whether this is a native oxide (possibly reforming in the time between sample polishing and immersion to the LBE bath) or forms upon specimen immersion in the LBE bath (see Fig. 6), one expects that dissolution attack will start as soon as this oxide film is locally degraded. This means that the incubation period for LBE dissolution attack will vary across the specimen surface, a fact that would explain to a certain extent the observed differences in the thickness of the dissolution-affected zone.

It falls outside the scope of this study to discuss possible causes of oxide scale failure, also in view of that fact that the evidence of oxide scale formation was very limited. An example of oxide scale formation is given in Fig. 7f, where discontinuous FeCr-containing oxide scales (only the Fe and Cr maps are shown, but EDS confirmed that the Fe/Cr-enriched layer was an oxide) were found on top of a deep (~258 µm) 'pit'. The origin of these oxides is not clear; however, Schroer et al. [12] had previously suggested that oxides might form above the dissolution-affected zone by the oxidation of steel alloying elements that are leached out of the steel. The same authors proposed that defective oxides act as sinks for outward diffusing steel alloying elements, maintaining concentration gradients that are favourable for the further steel depletion and keeping oxygen away from the depletion zone. In another study, Schroer et al. [13] suggested that LBE penetrations become very poor in oxygen as dissolution attack deepens, eventually inhibiting the reprecipitation of Cr-based oxides inside the depletion zone. This promotes the outward diffusion of Cr, which results in the formation of Cr-containing oxides similar to the ones observed in Fig. 7f on top of the depletion zone.

The formation of 'pits' similar to that in Fig. 7f is a concern for the reliable use of austenitic stainless steels in LBE-cooled nuclear systems, especially for thin-walled components such as heat exchanger tubes and fuel cladding tubes. Locally-enhanced dissolution, herein named dissolution 'pitting', has been reported to occur under a seemingly intact oxide scale, even in conditions of flowing, adequately-oxygenated LBE. The underlying cause of the occurrence of dissolution

'pitting' in 316L steels exposed to liquid LBE is the local failure of the oxide scale [12-14,17,18,21,59]. Oxide scale failure allows the LBE permeation to the oxide/steel interface, which is often enriched in highly-soluble species such as Cr and/or Ni [13,14]. The latter might account for the quick lateral expansion of the 'pit' and explain its typically large diameter (Fig. 7f). Once nucleated, the 'pit' grows by various possible mechanisms [12,13] and resealing by oxidation is practically impossible. The frequency of dissolution 'pitting' increases as the T and LBE flow velocity increase and the LBE C_O decreases, in agreement with the theories attributing its occurrence to local oxide failure, which is also promoted at high temperatures, high LBE flow velocities and low LBE oxygen concentrations. This study also demonstrates that the local steel microstructure can trigger dissolution 'pitting' (see section 3.4.2).

Dissolution corrosion usually started by LBE intergranular penetration into the grain boundaries with access to the steel surface (Figs. 9a-9c). Prior studies on the intergranular penetration of liquid metals into solid metals, in the absence of external stresses, suggested the existence of a wetting transition temperature, T_w, above which the liquid metal wets the grain boundaries and below which it diffuses into the grain boundaries [60-63]. The driving force for intergranular penetration is the reduction in the overall energy of the system, which is achieved when the surface energy of the solid/liquid interfaces (γ_{sl}) is smaller than the energy of the initial grain boundary (γ_{gb}), i.e., when $2\gamma_{sl} \leq \gamma_{gb}$. It falls outside the scope of this work to determine whether the intergranular LBE penetration into the exposed 316L steels qualifies as wetting or diffusion, also in view of the complexity of a dedicated investigation; such investigation is usually conducted by exposing pure (solid) metals to liquid metals saturated in the metals they contact, hence the steel/LBE system is clearly too complex to address, due to the presence of impurities in both steel and LBE and the forbidding cost of producing model alloys of high purity.

Intergranular LBE penetration into the near-surface layer of grains (Figs. 9a-9c) is followed by the further LBE penetration into the steel along preferential LBE ingress paths. The appearance of the dissolution-affected zone in the early stages of attack is very intricate, almost 'lace-like', whereupon planes of LBE penetration cross-link with grains that are intergranularly attacked (Fig. 9b). As dissolution corrosion advances, the continuous interplay of the steel microstructure with the dissolution process ensures the propagation of damage deeper into the steel (Fig. 10). This is reflected in the continuous change in the direction of attack, depending on the local orientation of the favourable paths for LBE ingress into the unaffected steel (Fig. 10).

3.2. Kinetic Data

Increasing the exposure time from 253 h to 3282 h increased the maximum depth of dissolution attack from 21 µm to 152 µm for the 316LSA steel, from 33 µm to 346 µm for the 316LH1 steel, and from 48 µm to 265 µm for the 316LH2 steel. The evolution of the maximum depth of dissolution attack as function of the exposure time is shown in Fig. 11a. As already mentioned, the maximum dissolution depth provides an estimate of the maximum dissolution rate of 316L steels at 500°C, which is important for the lifetime prediction of thin-walled components. The

experimental data were fitted based on a model that assumes a decrease in the dissolution rate, $\frac{dx}{dt}$, with the depth of dissolution, x, according to the following equation:

$$\frac{dx}{dt} = Kx^a \quad (4)$$

where K and a are two constants. Integration of equation (4) gives:

$$x = A(t - t_0)^c \quad (5)$$

where $c = \frac{1}{-a+1}$, $A = \left(\frac{K}{c}\right)^c$, and t_0 is the incubation time. Fitting of the three variables *A*, *c* and t_0, for both maximum and average dissolution depth, was performed using the Levenberg-Marquardt iteration algorithm. Note that $c \approx 0.5$ for the maximum depth, which means that the maximum dissolution rate is inversely proportionate to the dissolution depth:

$$\frac{dx}{dt} \approx \frac{K}{x} \quad (6)$$

The above analysis shows that LBE dissolution attack is decelerated as the dissolution depth increases, probably due to the fact that the outward diffusion of steel alloying elements must occur through an increasingly thicker dissolution zone. The instantaneous maximum dissolution rate decreased from 6.62×10^{-2}, 1.50 and 2.09×10^{-1} μm/h after 253 h to 1.75×10^{-2}, 4.56×10^{-2} and 3.58×10^{-2} μm/h after 3282 h for the 316LSA, 316LH1 and 316LH2 steels, respectively. The fact that 316LH1 dissolves faster than 316LH2 might partly be attributed to the fact that 316LH1 was finer-grained than 316LH2, as dissolution corrosion advances via intergranular LBE penetration. On the other hand, the faster attack in the cold-drawn steels as compared to the solution-annealed steel is associated with the acceleration of the dissolution process by the presence of deformation-induced defects in the steel microstructure (see section 3.4.2).

Yamaki et al. [15] have previously exposed specimens of the EUROTRANS-DEMETRA 316L steel heat, i.e., the 316LSA steel in this work, to oxygen-poor static LBE at 500°C for 170-3045 h. They reported linear dissolution kinetics and observed two modes of dissolution attack, a slower and a faster one. The determined by Yamaki et al. [15] corrosion rate for the faster mode was 147 μm/year, while the maximum dissolution rate determined for the 316LSA steel is 187 μm/year. The 21% faster dissolution rates observed in this work compared to the work of Yamaki et al. [15] might be associated with the fact they used a less reducing gas during testing (i.e., Ar-4%H_2 instead of the Ar-5%H_2 used here). In fact, Yamaki et al. [15] reported that the LBE oxygen concentration was kept at $C_O < 10^{-8}$ mass%, but did not actually measure it by oxygen sensors, so a direct comparison of the C_O conditions between the two studies is impossible. An indication that the exposure conditions were more reducing in the present work is that the maximum dissolution depth was ~100 μm after 3282 h, while Yamaki et al. [15] reported this to be ~60 μm after 3045 h. It is also worthwhile mentioning that linearity seems to be maintained up to a critical dissolution zone thickness, which is estimated to be ~70 μm in this study; for thicker dissolution zones, the rate decreases and the outward elemental diffusion becomes the rate-limiting step.

This agrees with the findings of Yamaki et al. [15] who suggested linear kinetics for dissolution depths < 60 µm.

Yamaki et al. [15] reported an incubation time of 112 h for the faster dissolution mode, while this study estimated the incubation time to be ~25 h; this might also be related with the fact that the exposure conditions were more reducing in this work than in the work by Yamaki et al. [15]. The different incubation times – with an uncertainty due to the limited data – determined for the maximum dissolution depth was 244 h, 161 h and 25 h for 316LH1, 316LH2 and 316LSA, respectively. It is not yet clear why the incubation time varied so much between steel heats. One might assume that this is caused by the different protectiveness of oxide scales on cold-deformed vs. solution-annealed steels; however, this assumption merits further investigation.

Prolonging the exposure from 253 h to 3282 h increased the average depth of dissolution attack from 6.5±3.9 µm to 73.5±13.3 µm for the 316LSA steel, from 12.9±6.6 µm to 286.8±29.7 µm for the 316LH1 steel, and from 18.1±8.5 µm to 177.5±25.5 µm for the 316LH2 steel (Fig. 11b). The scatter in the dissolution zone thickness values can partly be associated with the fact that the LBE oxygen concentration differed from test to test (Fig. 5). Moreover, during each test, local LBE oxygen concentration gradients cannot be excluded, due to the lack of efficient LBE mixing. Also, the observed scatter in dissolution depth can be associated with the local vulnerability of the oxide scale, steel microstructure (section 3.4) and steel chemical composition (section 3.3).

3.3. Dissolution Mechanisms: Selective Leaching vs. Non-Selective Leaching

3.3.1. Selective Leaching and Steel Ferritization

Dissolution attack usually started with intergranular LBE penetration, followed by the selective leaching of the Ni, Mn and Cr from the affected grains; the Fe-based residual grains were then consumed by LBE at a slower pace. Selective leaching of Ni, Mn and Cr is driven by the greater solubility of these elements in LBE when compared to the solubility of Fe. Martinelli et al. [64] has experimentally assessed the maximum solubility of Ni in LBE to be ~2.98 mass% at 500°C; the suggested Ni solubility (in mass%) in the 415-900°C range is given by the following equation:

$$\log S_{\mathrm{Ni}} = 1.7 \pm 0.08 - \frac{1009}{T} \quad (7)$$

where *T* is the absolute temperature in K.

Gossé [65] has performed a thermodynamic assessment of the Ni, Cr and Fe solubility limits in LBE in contact with the $Fe_{0.71}Cr_{0.18}Ni_{0.11}$ model alloy, which is compositionally similar to the 316L steel. He found that the Ni solubility is the highest; the Cr solubility is 10^2 times lower than that of Ni in the 227-727°C range; and the Fe solubility is 10^3 times lower than that of Ni at 227°C, this gap reducing with temperature. The Ni, Cr and Fe solubilities (in at.%) can be calculated using equations (8)-(10), where *T* is the absolute temperature in K:

$$\log S_{\mathrm{Ni}} = -11.904 + \frac{12662.2}{T} - \frac{6209 \times 10^3}{T^2} + \frac{794.55 \times 10^6}{T^3} + 2.725 \times 10^{-3} T \quad (232\text{-}900°C) \quad (8)$$

$$\log S_{Cr} = -1.2582 - \frac{2269.2}{T} \quad (230\text{-}900°C) \quad (9)$$

$$\log S_{Fe} = 0.2224 - \frac{4104.2}{T} \qquad (126\text{-}900°C) \qquad (10)$$

The Ni, Cr and Fe solubilities at 500°C were calculated using equations (8)-(10) and converted to mass%; according to these calculations, the Ni, Cr and Fe solubilities are 2.30×10^{-1}, 1.60×10^{-3} and 2.19×10^{-4}, respectively. Even though the Ni solubility in LBE decreases when other elements (Cr, Fe) are also dissolved in the HLM, it remains high and capable of driving the Ni dissolution process. EDS line scans illustrating the selective leaching of Ni, Mn and Cr from intergranularly-attacked grains are shown in Figs. 12c and 14d. The selective removal of Ni, Mn and Cr increases the Fe content of the affected grains relative to the unaffected steel. The same EDS line scans show grain boundary decoration by Pb and Bi. A consequence of the selective removal of the austenite stabilizers Ni and Mn is steel ferritization, i.e., the transformation of the original austenitic (*fcc*) grains to ferritic (*bcc*) ones. A TEM proof of ferritization is provided in Figs. 9d-9f. Usually, ferritization is accompanied by grain refinement of the dissolution-affected zone with respect to the grain size of the unaffected steel (Figs. 15c-15d).

3.3.2. Non-Selective Leaching

Non-selective leaching was mainly observed locally in the solution-annealed 316LSA steel (Figs. 13b-13d). Interestingly, the alternation of areas of selective leaching with areas of non-selective leaching often occurred over a short distance (Fig. 13). This was quite puzzling and explaining it by suggesting a periodic failure of the oxide scale on the steel surface would be farfetched. The short-range transition from selective to non-selective leaching is currently attributed to local variations in the steel chemical composition. Compositional fluctuations in industrial-size steel heats are associated with interdendritic segregation during solidification from the melt, and are maintained during hot rolling of the casting [55]. It has been previously suggested [12,13,59] that there is a threshold concentration of highly-soluble elements, such as Ni, above which selective leaching is promoted and below which non-selective leaching prevails. However, recent ongoing studies have shown that steel compositional differences are associated with differences in the local steel deformability and, hence, in the local steel susceptibility to dissolution attack. The study of steel chemical banding on 316L dissolution corrosion is still ongoing and its results will be reported when this study is complete.

3.4. Effect of Steel Microstructure

3.4.1. Three-Dimensionality of Steel Microstructure

Corrosion quantification often involves measuring the depth of attack on metallographic cross-sections that give a two-dimensional impression of the three-dimensional steel microstructure. This may introduce errors in the estimation of the true corrosion rate, as the path of LBE ingress is non-linear and corrosion evolves by interconnecting LBE penetrations in the 3D steel volume. Interconnectivity is achieved by cross-linking paths of preferential LBE penetration into the base steel, such as grain boundaries and deformation twins (Figs. 10, 12, 14). Examples of the way LBE dissolution attack relies on the three-dimensionality of the steel microstructure to further

advance are shown in Fig. 14. Often, 'bridges' connect the main dissolution-affected zone with 'islands' of affected grains several micrometres from the main dissolution front (Figs. 14a-14b).

3.4.2. Grain Boundaries and Deformation Twin Boundaries

LBE dissolution attack usually starts with LBE intergranular penetration, especially in the case of selective leaching (Figs. 9, 12, 13a). Since grain boundaries are characterised by atomic disorder and many defects (dislocations, point defects, small voids, impurities), they become favourable paths for LBE penetration, presumably because they ensure faster elemental diffusion than the comparatively defect-free grain bulk [66]. As observed in this study, finer-grained steels are characterised by higher dissolution rates than coarser-grained ones (Fig. 11). The steel grain size distribution must thus be optimized before a 316L steel can be used in contact with LBE.

The LOM investigation of the dissolution front in cold-drawn steels revealed LBE penetrations that followed parallel, closely-spaced striations within the same grain (Figs. 15a-15b). The high-resolution EBSD study of such a grain showed that the micro-volumes confined between two consecutive striations had a different crystallographic orientation than the grain bulk (Fig. 15c). EBSD confirmed the ferritization of the dissolution-affected zone, illustrating grain refinement of the dissolution-affected zone with respect to the grain size of the unaffected steel (Fig. 15d). In order to elucidate the nature of the closely-spaced striations in the grain of Fig. 15c, two thin foils were prepared by FIB for further TEM study: one taken exactly at the dissolution front (area 1, Fig. 16a) and one away from the dissolution front (area 2, Fig. 16a), both along the same set of striations. The SEM image of Fig. 16b shows the FIB foil from area 1, revealing that an LBE penetration follows the edge of a set of parallel thin lines in the steel. Since these lines were also visible in the cross-section of Fig. 16a, it appeared they were actually planes extending deep into the base steel below the plane of the cross-section in Fig. 16a. The observed gaps are partly formed during FIBing, since LBE is easier to remove by ion beam milling than the steel, creating cavities in spaces filled by LBE. The gaps might have also formed by the post-freezing expansion of the LBE residues, which is associated with the formation of a mixture of phases β (Pb_7Bi_3) and γ (Bi with 0.4% Pb); after some time, the close-packed β-phase transforms into the less dense γ-phase, resulting in the opening of LBE-filled spaces [67]. The FIB foil from area 1 was studied by TEM, after thinning to electron transparency. Fig. 17a provides an overview of this foil. A selected area diffraction pattern (SADP) taken over the area outlined by a circle in Fig. 17a showed set of twins in the $<1\bar{1}0>$ orientation (Fig. 17b). This SADP is identical to the pattern in Fig. 3c, be it with a lower intensity and thus finer twin width for one of the variants, confirming the {111} twin nature. The FIB foil taken from area 2 showed the same set of twins as in area 1; the orientation of this set of twins was confirmed by selected area diffraction (not shown here).

Several BF images were taken at higher magnification along the LBE penetration path from the foil in area 1 and were assembled (Fig. 17c) to cover the zone within the rectangular frame in Fig. 17a. Several EDS point analyses were done along the LBE penetration and its surroundings (Fig. 17e): sites A-C correspond to pure LBE locations, while sites D-F correspond to unaffected steel

locations (i.e., no depletion in Ni or Cr). The overview BF image of Fig. 17c illustrates the mechanism of LBE penetration between twin laths: LBE travels in the direction parallel to the close-packed twinning planes, while remaining bounded by the two neighbouring twin boundaries and leaching out steel alloying elements only within the attacked twin lath. At several locations, steps are observed at the borders between LBE penetration and stainless steel matrix. The orientation of such steps with respect to the {111} twin plane is reflected in Fig. 17d: traces of slip planes at an angle of ~70° with the trace of the {111} twin plane are visible in some of the twin laths on the left hand side of Fig. 17d. The angle is consistent with the theoretical angle between close-packed planes {111} and {11$\bar{1}$} along this zone axis. It appears that the steps are aligned parallel to the direction of the slip plane traces visible within the twin laths. The following mechanism can thus be tentatively proposed to describe the twin lath-facilitated LBE penetration in cold-worked 316L steels: LBE penetration starts from a preferential site within a narrow twin lath. While the LBE penetration remains constrained between consecutive twin walls at the penetration front, it can bear its way into a neighbouring twin lath by following close-packed slip planes crossing the twin walls along the length of the LBE penetration, where a faster diffusion of dissolved steel species is possible.

Experimental evidence of the contribution of the steel microstructure to dissolution 'pitting' is provided in Fig. 18. LOM located a 'pit' (maximum depth ~84 µm) in an area where the depth of dissolution did not exceed ~28 µm (Figs. 18a-18b). The surface relief achieved by OPS polishing revealed that the 'pit' growth was guided by the local convergence of certain boundaries in the steel. These boundaries were associated with large (160-220 µm) grains that resulted in a much deeper dissolution attack locally compared with the depth of attack in the immediate vicinity of the 'pit'. EBSD confirmed that these boundaries were twin boundaries (Fig. 18d), while EDS analysis of the same area identified the areas where LBE was present (Fig. 18e – Bi map).

3.4.3. Steel Precipitates

Manganese sulphide (MnS), oxides and δ-ferrite precipitates are often encountered in 316L stainless steels; hence, their interaction with the dissolution corrosion process is interesting, as it has been suggested that "near-surface inclusions, such as MnS or slag (i.e., oxide) particles, might account for the local breakdown of the protective oxide scales formed on 316L stainless steels during their exposure to liquid LBE" [13]. Fig. 19 shows typical examples of the observed lack of interaction between MnS, oxides and δ-ferrite precipitates and LBE. First, MnS inclusions remained immune to LBE dissolution attack even after prolonged exposures, as suggested by the presence of intact particles at large distances from the dissolution front (Fig. 19a). This means that MnS was practically insoluble in LBE at 500°C; therefore, particles close to the steel surface could not contribute to the local breakdown of oxide scales and the onset of 'pitting' by their own dissolution in LBE. It is possible, however, that the MnS/steel interface facilitated the LBE ingress into the steel, thus contributing to the onset of dissolution attack for inclusions situated close to the steel surface. Such hypothesis merits further investigation.

Oxide precipitates were also resilient to LBE dissolution attack, remaining intact while the steel matrix that envelops them is severely attacked (Fig. 19c). Elongated (stringer-like) oxide ('slag') precipitates aligned parallel to the steel rolling direction were only observed in the solution-annealed 316LSA steel. EDS elemental analysis showed them to be Al_2O_3-based with variable Mg, Si and Ca contents (Fig. 19d). Oxide 'stringers' were often observed in the centre of nodular perturbations of the dissolution front (Fig. 19c). This suggests that the oxide/steel interface is a path of preferential LBE ingress into the steel; once LBE decorates that interface, the dissolution front advances locally, forming nodular perturbations along the length of the oxide 'stringer'.

The interaction of δ-ferrite with LBE is similar to that of oxide inclusions: δ-ferrite resists better LBE dissolution attack than the base steel (Figs. 19e-19f), and the δ-ferrite/steel interface is a path of preferential LBE ingress into the steel. The better compatibility of δ-ferrite with LBE can be associated with the fact it contains less highly-soluble alloying elements than the base steel (i.e., ~9% Cr in δ-ferrite as opposed to 10-14% Ni, 2% Mn and 16-18% Cr in the base steel).

3.4.4. 'Notches'

Selective leaching of the austenite stabilizers Ni and Mn results in ferritization, i.e., the phase transformation of austenite (*fcc*) to ferrite (*bcc*). The *fcc*-to-*bcc* phase transformation is probably accompanied by a volumetric change, which will cause stress triaxiality in the immediate vicinity of sharp protuberances of the dissolution front, such as the ones shown in Fig. 20. Whether the volumetric change is expansion [67] or contraction, the stress field around sharp protrusions of the dissolution front is characterised by a stress intensity factor K_I that depends on the externally-applied load and the size of the protrusion, in agreement with linear-elastic fracture mechanics. When K_I approaches a critical value, K_c, fracture occurs due to unstable crack growth [68]. Such features may be considered as internal steel 'notches' that act as stress concentrators in notch-sensitive metals (e.g., pure Fe), interacting with dislocation motion under an externally-applied load that exceeds the yield strength, and initiating brittle failure [69]. Even though 316L steels (*fcc* alloys) are probably notch-insensitive, they suffer irradiation embrittlement [70-73], becoming notch-sensitive in service. Hence, the presence of corrosion-induced sharp notches (Fig. 20) is expected to be a concern for irradiated 316L steels and, in particular, for thin-walled components, where unstable crack propagation might easily lead to failure.

Even non-irradiated austenitic stainless steels show a greater propensity towards brittle fracture after dissolution-induced ferritization, as reported by Müller et al. [19] and Schroer et al. [12], but the cracks are arrested in the ductile austenitic matrix of the unaffected steel. This is not surprising considering that the dissolution-affected zone is ferritized and that ferritic steels (e.g., T91 and similar steels) are known to be susceptible to liquid metal embrittlement (LME) [74-76]. The onset of brittle fracture in the LME-prone dissolution-affected zone is expected to propagate fast in irradiation-hardened steels, as the capacity of the steel matrix to blunt cracks reduces in a neutron environment. Naturally, these assumptions must be validated by means of a dedicated study on the potential synergy of dissolution corrosion, LME, and irradiation.

4. Conclusions

In this work, different 316L austenitic stainless steel heats, both solution-annealed and cold-deformed, were exposed to oxygen-poor (C_O < 10^{-8} mass%), static liquid LBE for 253-3282 h at 500°C, so as to understand the grade-specific dissolution corrosion behaviour of 316L steels. Under the specific exposure conditions (T = 500°C, C_O < 10^{-8} mass%), dissolution corrosion was the prevailing liquid metal corrosion mechanism, indicating that any possible oxide scales were not protective. The dissolution zone thickness was non-uniform and deep pit-like features formed in various locations on the steel surface; some of the 'pits' were covered by FeCr-containing oxide residues. The main findings of this work could be summarised as follows:

1. Corrosion was invariably deeper in the cold-drawn steels than in the solution-annealed one for identical exposure conditions. The higher susceptibility of the cold-drawn steels to dissolution attack was associated with the presence of deformation-induced defects, such as twin laths, that acted as paths of preferential LBE ingress into the steel.
2. The prevailing dissolution mechanism for all steels was selective leaching of Ni, Mn and Cr, which resulted in ferritization of the dissolution-affected zone. Non-selective leaching was observed in the solution-annealed steel together with selective leaching. The manifestation of non-selective leaching in the solution-annealed steel was attributed to compositional inhomogeneities typical of industrial-size steel heats.
3. Analysis of the experimental data showed that the maximum dissolution rate was inversely proportionate to the dissolution depth. Deceleration of dissolution corrosion is observed when the dissolution zone exceeds a critical thickness (~70 μm), i.e., when the outward diffusion of dissolved elements becomes the rate-limiting step. The short incubation times (25-250 h) confirmed the effectiveness of the testing approach in promoting dissolution.
4. A strong interplay of the dissolution corrosion process with the steel microstructure was observed, whereupon LBE penetration occurred along preferential paths in the steel, such as grain boundaries and deformation twins. Dissolution corrosion progressed fastest in the finer-grained cold-drawn steel and slowest in the solution-annealed steel.

Acknowledgments

The authors would like to acknowledge the following 316L stainless steel suppliers: Industeel, ArcelorMittal Group, for the 316LSA plate procured and characterised in the FP6 EUROTRANS-DEMETRA project (Contract no. FI6W-CT-2004-516520); OLARRA Aceros Inoxidables, Spain, for the 316LH1 rod; and SIDERO STAAL nv, Belgium, for the 316LH2 rod. K. Lambrinou would like to thank J. Joris for technical support during the launching and follow up of all corrosion tests, J. Lim for the manufacturing and calibration of the oxygen sensors used in these tests, T. Lapauw for the XRD measurements on the pristine steels, and S. Van den Broeck for the FIB sample preparation. Special thanks to S. Gavrilov for fruitful and intense discussions. The authors gratefully acknowledge the funding provided in the framework of the ongoing development of the MYRRHA

irradiation facility. The research leading to these results falls within the framework of the European Energy Research Alliance Joint Programme on Nuclear Materials (EERA JPNM).

References

[1] F.J. Martín-Muñoz, A. Heinzel, A. Weisenburger, G. Müller, S. Gavrilov, K. Lambrinou, Compatibility of structural materials with lead-bismuth eutectic and lead: Standardisation of data, corrosion mechanism and rate, in: Handbook on lead-bismuth eutectic alloy and lead properties, materials compatibility, thermal hydraulics and technologies, 2015 edition, OECD/NEA, 2015, pp. 431-485.

[2] N. Li, Lead-alloy coolant technology and materials – technology readiness level evaluation, Prog. Nucl. Energ. 50 (2008) 140-151.

[3] J. Zhang, A review of steel corrosion by liquid lead and lead-bismuth, Corros. Sci. 51 (2009) 1207-1227.

[4] J. Konys, W. Krauss, C. Schroer, H. Steiner, Z. Voß, O. Wedemeyer, Corrosion of structural materials in liquid lead alloys for nuclear applications, Corrosion 63 (2007) 1124-1137.

[5] A. Weisenburger, C. Schroer, A. Jianu, A. Heinzel, J. Konys, H. Steiner, G. Müller, C. Fazio, A. Gessi, S. Babayan, A. Kobzova, L. Martinelli, K. Ginestar, F. Balbaud-Célerier, F.J. Martín-Muñoz, L. Soler-Crespo, Long term corrosion on T91 and AISI1 316L steel in flowing lead alloy and corrosion protection barrier development: Experiments and models, J. Nucl. Mater. 415 (2011) 260-269.

[6] L.A. Weinstein, J. Loomis, B. Bhatia, D.M. Bierman, E.N. Wang, G. Chen, Concentrating solar power, Chem. Rev. 115 (2015) 12797-12838.

[7] H. Aït Abderrahim, D. De Bruyn, G. Van den Eynde, S. Michiels, Transmutation of high-level nuclear waste by means of accelerator driven system, in: R. Stock (Ed.), Encyclopedia of Nuclear Physics and its Applications, 1st edition, 2013, Wiley-VCH Verlag GmbH & Co. KGaA, pp. 689-704.

[8] C. Schroer, O. Wedemeyer, J. Konys, Aspects of minimizing steel corrosion in liquid lead-alloys by addition of oxygen, Nucl. Eng. Des. 241 (2011) 4913-4923.

[9] M. Caro, K. Woloshun, F. Rubio, S.A. Maloy, P. Hosemann, Heavy liquid metal corrosion of structural materials in advanced nuclear materials, JOM 65 (2013) 1057-1066.

[10] P. Hosemann, R. Dickerson, P. Dickerson, N. Li, S.A. Maloy, Transmission electron microscopy (TEM) on oxide layers formed on D9 stainless steel in lead bismuth eutectic (LBE), Corros. Sci. 66 (2013) 196-202.

[11] C. Schroer, J. Konys, Physical chemistry of corrosion and oxygen control in liquid lead and lead-bismuth eutectic, Wissenschaftliche Berichte FZKA 7364, Forschungszentrum Karlsruhe in der Helmholtz-Gemeinschaft, 2007, pp. 17-28.

[12] C. Schroer, O. Wedemeyer, J. Novotny, A. Skrypnik, J. Konys, Selective leaching of nickel and chromium from type 316 austenitic steel in oxygen-containing lead-bismuth eutectic (LBE), Corros. Sci. 84 (2014) 113-124.

[13] C. Schroer, E. Nold, J. Konys, Micro-analysis of 316L stainless-steel after long-term exposure to lead-bismuth eutectic at 550°C, in: Proc. European Corrosion Congress (EUROCORR 2009), CEFRACOR, 2010, Vol. 3, pp. 2062-2069.
[14] C. Schroer, J. Konys, Quantification of the long-term of steels T91 and 316L in oxygen-containing flowing lead-bismuth eutectic at 550°C, J. Eng. Gas Turb. Power 132 (2010) 082901-1 – 082901-7.
[15] E. Yamaki, K. Ginestar, L. Martinelli, Dissolution mechanism of 316L in lead-bismuth eutectic at 500°C, Corros. Sci. 53 (2011) 3075-3085.
[16] Y. Kurata, Corrosion behaviour of cold-worked austenitic stainless steels in liquid lead-bismuth eutectic, J. Nucl. Mater. 448 (2014) 239-249.
[17] V. Tsisar, C. Schroer, O. Wedemeyer, A. Skrypnik, J. Konys, Corrosion behavior of austenitic steels 1.4970, 316L and 1.4571 in flowing LBE at 450 and 550°C with 10^{-7} mass% dissolved oxygen, J. Nucl. Mater. 454 (2014) 332-342.
[18] M. Roy, L. Martinelli, K. Ginestar, J. Favergeon, Dissolution and oxidation behaviour of various austenitic steels and Ni rich alloys in lead-bismuth eutectic at 520°C, J. Nucl. Mater. 468 (2016) 153-163.
[19] G. Müller, A. Heinzel, J. Konys, G. Schumacher, A. Weisenburger, F. Zimmermann, V. Engelko, A. Rusanov, V. Markov, Behavior of steels in flowing liquid PbBi eutectic alloy at 420-600°C after 4000-7200 h, J. Nucl. Mater. 335 (2004) 163-168.
[20] M. Kondo, M. Takahashi, Metallurgical analysis of a tube ruptured in the lead bismuth corrosion test facility, J. Nucl. Sci. Technol. 43 (2006) 174-178.
[21] C. Schroer, O. Wedemeyer, J. Novotny, A. Skrypnik, J. Konys, Long-term service of austenitic steel 1.4571 as a container material for flowing lead-bismuth eutectic, J. Nucl. Mater. 418 (2011) 8-15.
[22] Y. Kurata, M. Futukawa, S. Saito, Corrosion behavior of steels in liquid lead-bismuth with low oxygen concentrations, J. Nucl. Mater. 373 (2008) 164-178.
[23] D. Sapundjiev, S. Van Dyck, W. Bogaerts, Liquid metal corrosion of T91 and A316L materials in Pb-Bi eutectic at temperatures 400-600°C, Corros. Sci. 48 (2006) 577-594.
[24] Ph. Deloffre, A. Terlain, F. Barbier, Corrosion and deposition of ferrous alloys in molten lead-bismuth, J. Nucl. Mater. 301 (2002) 35-39.
[25] G. Benamati, C. Fazio, H. Piankova, A. Rusanov, Temperature effect on the corrosion mechanism of austenitic and martensitic steels in lead-bismuth, J. Nucl. Mater. 301 (2002) 23-27.
[26] F. Gnecco, E. Ricci, C. Bottino, A. Passerone, Corrosion behaviour of steels in lead-bismuth at 823 K, J. Nucl. Mater. 335 (2004) 185-188.
[27] Y. Kurata, M. Futakawa, Excellent corrosion resistance of 18Cr-20Ni-5Si steel in liquid Pb-Bi, J. Nucl. Mater. 325 (2004) 217-222.
[28] Y. Kurata, Corrosion experiments and materials developed for the Japanese HLM systems, J. Nucl. Mater. 415 (2011) 254-259.

[29] Y. Kurata, S. Saito, Temperature dependence of corrosion of ferritic/martensitic and austenitic steels in liquid lead-bismuth eutectic, Mater. Trans. 50 (2009) 2410-2417.
[30] Y. Kurata, M. Futukawa, S. Saito, Comparison of the corrosion behavior of austenitic and ferritic/martensitic steels exposed to static liquid Pb-Bi at 450 and 550°C, J. Nucl. Mater. 343 (2005) 333-340.
[31] F.J. Martín-Muñoz, L. Soler-Crespo, D. Gómez-Briceño, Assessment of the influence of surface finishing and weld joints on the corrosion/oxidation behaviour of stainless steels in lead bismuth eutectic, J. Nucl. Mater. 416 (2011) 80-86.
[32] O. Yeliseyeva, V. Tsisar, G. Benamati, Influence of temperature on the interaction mode of T91 and AISI 316L steels with Pb-Bi melt saturated by oxygen, Corros. Sci. 50 (2008) 1672-1683.
[33] F.J. Martín, L. Soler, F. Hernández, D. Gómez-Briceño, Oxide layer stability in lead-bismuth at high temperature, J. Nucl. Mater. 335 (2004) 194-198.
[34] Ph. Deloffre, A. Terlain, Influence of Zn as a spallation product on the behaviour of martensitic steel T91 and austenitic steel 316L in liquid Pb-Bi, J. Nucl. Mater. 335 (2004) 244-248.
[35] G. Benamati, A. Gessi, P-Z. Zhang, Corrosion experiments in flowing LBE at 450°C, J. Nucl. Mater. 356 (2006) 198-202.
[36] A. Gessi, G. Benamati, Corrosion experiments of steels in flowing Pb at 500°C and in flowing LBE at 450°C, J. Nucl. Mater. 376 (2008) 269-273.
[37] K. Kikuchi, Y. Kurata, S. Saito, M. Futakawa, T. Sasa, H. Oigawa, E. Wakai, K. Miura, Corrosion-erosion test of SS316 in flowing Pb-Bi, J. Nucl. Mater. 318 (2003) 348-354.
[38] S. Saito, K. Kikuchi, D. Hamaguchi, M. Tezuka, M. Miyagi, H. Kokawa, S. Watanabe, Corrosion-erosion test of SS316L grain boundary engineering material (GBEM) in lead bismuth flowing loop, J. Nucl. Mater. 431 (2012) 91-96.
[39] F.J. Martín-Muñoz, L. Soler-Crespo, D. Gómez-Briceño, Corrosion behaviour of martensitic and austenitic steels in flowing lead-bismuth eutectic, J. Nucl. Mater. 416 (2011) 87-93.
[40] I.V. Gorynin, G.P. Karzov, V.G. Markov, V.S. Lavrukhin, V.A. Yakovlev, Structural materials for power plants with heavy liquid metals as coolants, in: Proc. Heavy Liquid Metal Coolants in Nuclear Technology (HLMC-98), 1999, Vol. 1, pp. 120-132.
[41] G. Ilinčev, D. Kárník, M. Paulovič, A. Doubková, The impact of the composition of structural steels on their corrosion stability in liquid Pb-Bi at 500 and 400°C with different oxygen concentrations, J. Nucl. Mater. 335 (2004) 210-216.
[42] M. Takahashi, K. Ishikawa, T. Suzuki, S. Yoshida, T. Yano, H. Sekimoto, N. Sawada, K. Hata, S. Qiu, M. Imai, Experimental study on flow technology and steel corrosion of lead-bismuth, in: Proc. 10th International Conference on Nuclear Engineering (ICONE 10-22226), 2002, Vol. 2, pp. 607-615.
[43] M. Kondo, M. Takahashi, N. Sawada, K. Hata, Corrosion of steels in lead-bismuth flow, J. Nucl. Sci. Technol. 43 (2006) 107-116.

[44] M. Takahashi, M. Kondo, N. Sawada, K. Hata, Corrosion of steels in lead-bismuth flow, in: Proc. Global 2003 Int'l Conf. Nuclear Science and Technology, Nov. 16-23, 2003, New Orleans, LA, USA.
[45] M. Kondo, M. Takahashi, T. Suzuki, K. Ishikawa, K. Hata, S. Qiu, H. Sekimoto, Metallurgical study on erosion and corrosion behaviors of steels exposed to liquid lead-bismuth flow, J. Nucl. Mater. 343 (2005) 349-359.
[46] A. Doubková, F. Di Gabriele, P. Brabec, E. Keilová, Corrosion behavior of steels in flowing lead-bismuth under abnormal conditions, J. Nucl. Mater. 376 (2008) 260-264.
[47] J. Zhang, N. Li, Y. Chen, A.E. Rusanov, Corrosion behaviors of US steels in flowing lead-bismuth eutectic (LBE), J. Nucl. Mater. 336 (2005) 1-10.
[48] F. Balbaud-Celerier, P. Deloffre, A. Terlain, A. Rusanov, Corrosion of metallic materials in flowing liquid lead-bismuth, J. Phys. IV 12 (2002) Pr8-177 – Pr8-190.
[49] G. Müller, A. Heinzel, J. Konys, G. Schumacher, A. Weisenburger, F. Zimmermann, V. Engelko, A. Rusanov, V. Markov, Results of steel corrosion tests in flowing liquid Pb/Bi at 420-600°C after 2000 h, J. Nucl. Mater. 301 (2002) 40-46.
[50] N. Li, Active control of oxygen in molten lead-bismuth eutectic to prevent steel corrosion and coolant contamination, J. Nucl. Mater. 300 (2002) 73-81.
[51] J. Zhang, N. Li, Review of the studies on fundamental issues in LBE corrosion, J. Nucl. Mater. 373 (2008) 351-377.
[52] K. Lambrinou, V. Koch, G. Coen, J. Van den Bosch, C. Schroer, Corrosion scales on various steels after exposure to liquid lead–bismuth eutectic, J. Nucl. Mater. 450 (2014) 244-255.
[53] J. Van den Bosch, A. Almazouzi, EUROTRANS-DEMETRA-Task 4.1.2: Reference materials procurement, dispatching and characterisation, Restricted Contract Report SCK•CEN-R-4197, 2005.
[54] Metals Handbook, Desk Edition, second ed., J.R. Davis, Davis & Associates (Eds.), ASM International, 1998, pp. 153-173 and 375-379.
[55] G. Krauss, Steels: Processing, structure, and performance, fourth ed., ASM International®, Ohio, USA, 2008, pp. 161-175 and 510-512.
[56] R.E. Schramm, R.P. Reed, Stacking fault energies of seven commercial austenitic stainless steels, Metall. Trans. A 6 (1975) 1345-1351.
[57] J. Lim, A. Mariën, K. Roseel, A. Aerts, J. Van den Bosch, Accuracy of potentiometric oxygen sensors with Bi/Bi_2O_3 reference electrode for use in liquid LBE, J. Nucl. Mater. 429 (2012) 270-275.
[58] J. Lim, G. Manfredi, A. Mariën, J. Van den Bosch, Performance of potentiometric oxygen sensors with LSM-GDC composite electrode in liquid LBE at low temperatures, Sensor. Actuator. B 188 (2013) 1048-1054.

[59] V. Tsisar, C. Schroer, O. Wedemeyer, A. Skrypnik, J. Konys, Long-term corrosion of austenitic steels in flowing LBE at 400°C and 10^{-7} mass% dissolved oxygen in comparison with 450 and 550°C, J. Nucl. Mater. 468 (2016) 305-312.
[60] N. Marié, K. Wolski, M. Biscondi, Grain boundary penetration of nickel by liquid bismuth as a film of nanometric thickness, Scripta Mater. 43 (2000) 943-949.
[61] N. Marié, K. Wolski, M. Biscondi, Intergranular penetration and embrittlement of solid nickel through bismuth vapour condensation at 700°C, J. Nucl. Mater. 296 (2001) 282-288.
[62] K. Wolski, V. Laporte, Grain boundary diffusion and wetting in the analysis of intergranular penetration, Mater. Sci. Eng. A 495 (2008) 138-146.
[63] D. Empl, L. Felberbaum, V. Laporte, D. Chatain, A. Mortensen, Dihedral angles in Cu-1 wt.% Pb: grain boundary energy and grain boundary triple line effects, Acta Mater. 57 (2009) 2527-2537.
[64] L. Martinelli, Nickel solubility limit in liquid lead-bismuth eutectic, J. Nucl. Mater. 400 (2010) 232-239.
[65] S. Gossé, Thermodynamic assessment of solubility and activity of iron, chromium, and nickel in lead bismuth eutectic, J. Nucl. Mater. 449 (2014) 122-131.
[66] M. Mizouchi, Y. Yamazaki, Y. Iijima, K. Arioka, Low temperature grain boundary diffusion of chromium in SUS316 and 316L stainless steels, Mater. Trans. 45 (2004) 2945-2950.
[67] P. Hosemann, D. Frazer, E. Stergar, K. Lambrinou, Twin boundary-accelerated ferritization of austenitic stainless steels in liquid lead-bismuth eutectic, Scripta Mater. 118 (2016) 37-40.
[68] J.M. Barsom, S.T. Rolfe, Fracture and fatigue control in structures – Applications in fracture mechanics, third ed., ASTM Manual Series: MNL 41, ASTM International, West Conshohocken, USA, 1999, pp. 10-14.
[69] K. Lambrinou, Factors affecting the bulk embrittlement of Pb-free solder joints, in: G. Grossmann, Ch. Zardini (Eds.), ELFNET Handbook on Failure Mechanisms & Testing Methods for Lead-Free Solder Interconnects, Springer, 2011, pp. 19-63.
[70] K. Farrell, T.S. Byun, Tensile properties of candidate SNS target container materials after proton and neutron irradiation in the LANSCE accelerator, J. Nucl. Mater. 296 (2001) 129-138.
[71] S.A. Maloy, M.R. James, W.R. Johnson, T.S. Byun, K. Farrell, M.B. Toloczko, Comparison of fission neutron and proton/spallation neutron irradiation effects on the tensile behaviour of type 316 and 304 stainless steel, J. Nucl. Mater. 318 (2003) 283-291.
[72] C. Pokor, Y. Brechet, P. Dubuisson, J.-P. Massoud, X. Averty, Irradiation damage in 304 and 316 stainless steels: experimental investigation and modelling. Part II: Irradiation induced hardening, J. Nucl. Mater. 326 (2004) 30-37.
[73] J.D. Elen, P. Fenici, Fast neutron irradiation hardening of austenitic stainless steel at 250°C, J. Nucl. Mater. 191-194 (1992) 766-770.
[74] J. Van den Bosch, P. Hosemann, A. Almazouzi, S.A. Maloy, Liquid metal embrittlement of silicon enriched steel for nuclear applications, J. Nucl. Mater. 398 (2010) 116-121.

[75] G. Coen, J. Van den Bosch, A. Almazouzi, J. Degrieck, Investigation of the effect of lead-bismuth eutectic on the fracture properties of T91 and 316L, J. Nucl. Mater. 398 (2010) 122-128.
[76] T. Auger, G. Lorang, Liquid metal embrittlement susceptibility of T91 steel by lead-bismuth, Scripta Mater. 52 (2005) 1323-1328.

GRAPHICAL ABSTRACT

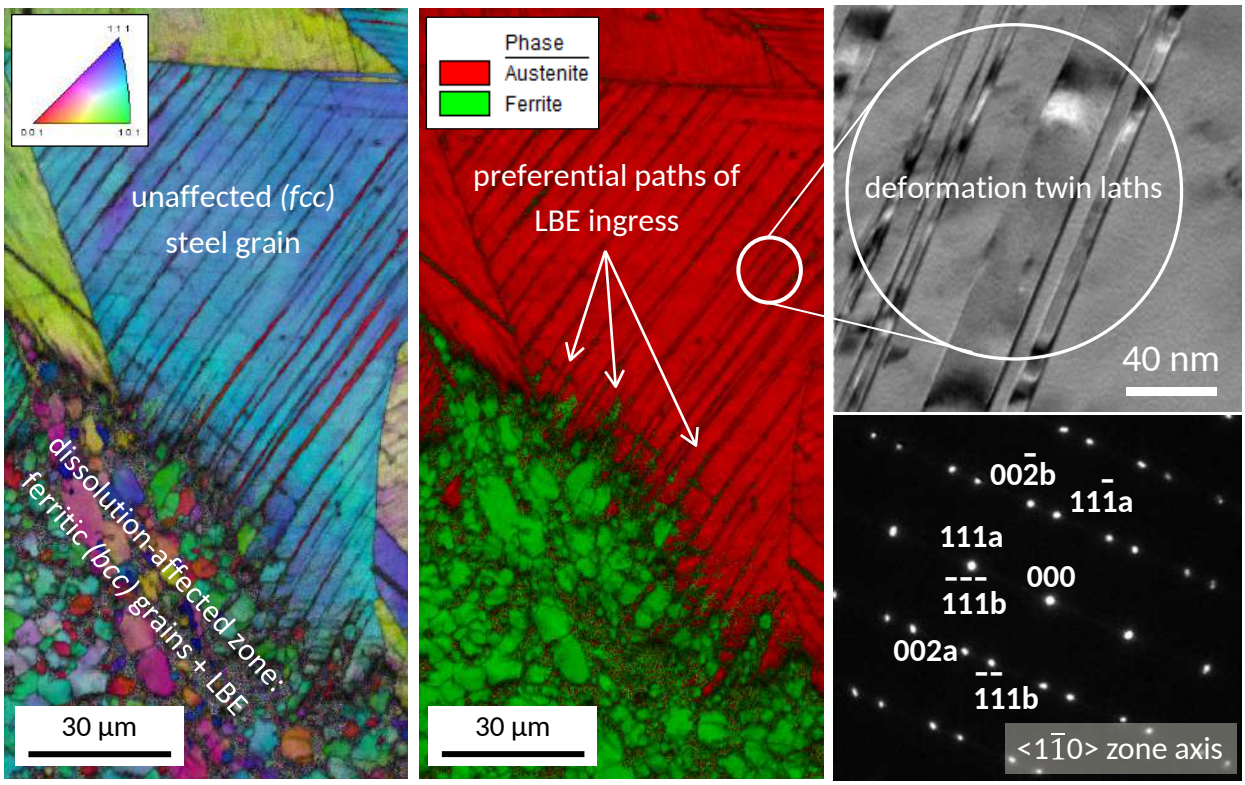

Dissolution corrosion of 316L austenitic stainless steels in contact with static liquid lead-bismuth eutectic (LBE) at 500°C

Konstantina Lambrinou[a,*], Evangelia Charalampopoulou[a,b], Tom Van der Donck[c], Rémi Delville[a], Dominique Schryvers[b]

[a] *SCK•CEN, Boeretang 200, 2400 Mol, Belgium*

[b] *University of Antwerp, Electron Microscopy for Materials Science (EMAT), Groenenborgerlaan 171, 2020 Antwerpen, Belgium*

[c] *KU Leuven, Department of Materials Engineering, Kasteelpark Arenberg 44, 3001 Leuven, Belgium*

* Corresponding author. Address: SCK•CEN, Boeretang 200, B-2400 Mol, Belgium. Tel.: +32-14-333164. *E-mail address*: klambrin@sckcen.be (K. Lambrinou).

Abstract

This work addresses the dissolution corrosion behaviour of 316L austenitic stainless steels. For this purpose, solution-annealed and cold-deformed 316L steels were simultaneously exposed to oxygen-poor (< 10^{-8} mass%) static liquid lead-bismuth eutectic (LBE) for 253-3282 h at 500°C. Corrosion was consistently more severe for the cold-drawn steels than the solution-annealed steel, indicating the importance of the steel thermomechanical state. The thickness of the dissolution-affected zone was non-uniform, and sites of locally-enhanced dissolution were occasionally observed. The progress of LBE dissolution attack was promoted by the interplay of certain steel microstructural features (grain boundaries, deformation twin laths, precipitates) with the dissolution corrosion process. The identified dissolution mechanisms were selective leaching leading to steel ferritization, and non-selective leaching; the latter was mainly observed in the solution-annealed steel. The maximum corrosion rate decreased with exposure time and was found to be inversely proportional to the depth of dissolution attack.

Keywords: stainless steel; SEM; TEM; de-alloying; intergranular corrosion; pitting corrosion

1. Introduction

One of the principal challenges in the development of Gen-IV lead-cooled fast reactors (Gen-IV LFRs) is the inherent corrosiveness of the primary heavy liquid metal coolant, such as lead (Pb) and lead-bismuth eutectic (LBE), for structural and cladding candidate steels considered for the construction of such reactor systems [1-5]. The inherent corrosiveness of lead-alloys (Pb, LBE, Pb-Li) is also a concern in fusion (tritium breeding blanket concept), in concentrated solar power (CSP) systems using heavy liquid metals [6], and in accelerator-driven systems (ADS) that use heavy liquid metals as spallation targets. An example of ADS technology currently under development at SCK•CEN, Belgium, is the flexible fast-spectrum irradiation facility MYRRHA (multi-purpose hybrid research reactor for high-tech applications), which will use liquid LBE as primary coolant and spallation target [7]. The mitigation of undesirable liquid metal corrosion (LMC) effects in MYRRHA is based on three main pillars, i.e., moderate operating temperatures (< 450°C), active oxygen control and understanding of the steel-specific LMC mechanisms. Active

oxygen control strives to form a protective oxide scale on the steel surface by dissolving precise amounts of oxygen in the heavy liquid metal (HLM) coolant [3,5,8-10]. The concentration of dissolved oxygen in the HLM must ensure the formation of protective oxides on the steels without oxidising the HLM itself (too high oxygen potential) [11]. If, for any reason, the oxygen potential drops below a certain level, the oxide scales will be reduced and the steel will come into direct contact with the HLM [11]; such eventuality is undesirable, as it will result in the steel dissolution corrosion. Dissolution corrosion of austenitic stainless steels, such as the 316L steel studied in this work, involves the loss of steel alloying elements into the heavy liquid metal and the progressive LBE penetration into the steel [12-18]; moreover, LBE dissolution attack can be locally-enhanced, creating deep 'pits' that might result in the premature breaching of thin-walled components, such as heat exchanger and fuel cladding tubes [12,19,20].

Since the MYRRHA candidate structural steel is the 316L stainless steel, it is important for the development of this system to understand all aspects of the LMC behaviour of the 316L grade, including the dissolution corrosion addressed in this study. The literature survey of the LMC behaviour of 316L and compositionally-similar steels (e.g., 316, 1.4571, 304L) in contact with liquid LBE revealed that, even though dissolution corrosion can occur locally at oxygen-saturated LBE and at temperatures as low as 400°C, it becomes particularly promoted at high temperatures ($T \geq 450$°C) and low LBE oxygen concentrations ($C_O < 10^{-8}$ mass%) [5,12-18,21-49]. Dissolution corrosion at elevated temperatures is promoted because the solubility of the main steel alloying elements (i.e., Ni, Cr, Fe) in the liquid LBE increases with temperature [50]. Low LBE oxygen concentrations favour dissolution corrosion by suppressing the formation of protective oxide scales. Based on the above, this study exposed 316L steels to oxygen-poor, static LBE ($C_O < 10^{-8}$ mass%) at 500°C to ensure the manifestation of dissolution corrosion. Despite the aggressive exposure conditions, the relevance of this study for the development of MYRRHA is manifold: first, one cannot exclude high-temperature transients ($T \geq 500$°C) during the system operation or oxygen-depleted zones of static LBE, i.e., similar service conditions as those tested here; second, the oxide scale might lose its local protectiveness with time due to chemical or mechanical damage, resulting in local dissolution attack [12,13,51,52]; third, the adopted testing approach allows the assessment of the maximum dissolution rate, which is important for establishing safety margins for the reliable use of thin-walled components.

This study aims at the in-depth understanding of the 316L steel dissolution corrosion behaviour in the absence of a protective oxide, an event that cannot be excluded in a real system, at least locally. To make this work relevant for the 316L steel grade and not for a single steel heat only, different heats must be simultaneously exposed to the same exposure conditions, so as to study the effect of the steel thermomechanical state and microstructure on its dissolution corrosion behaviour. This know-how is not only valuable for the optimum design of nuclear systems, such as MYRRHA, but also in view of the scarcity of studies addressing the effect of microstructure and thermomechanical state of the 316L steel grade on its compatibility with LBE.

2. Experimental

2.1. Materials

Three different 316L austenitic stainless steel heats (1 solution-annealed, 2 cold-drawn) were exposed to oxygen-poor static liquid LBE in this work. The solution-annealed heat, henceforth designated 316LSA, was a plate (15 mm thickness; EUROTRANS-DEMETRA heat [53]; Industeel, ArcelorMittal, S.A.) solution-annealed in the 1050-1100°C range, followed by a water quench. The cold-drawn steel heats, henceforth designated 316LH1 (Aceros Inoxidables OLARRA, S.A.) and 316LH2 (Sidero Staal nv), were cylindrical rods (∅ 10 mm): 316LH1 was solution-annealed at 1060°C for 4 h and water-quenched prior to cold deformation, while the heat treatment of 316LH2 was not provided by the steel supplier. Usually, solution annealing of austenitic stainless steels is conducted above 1040°C for short times (several minutes) to bring chromium carbides into solution in the austenite and control grain growth [54]. The degree of cold work of 316LH1 and 316LH2 heats was not provided by the suppliers. Table 1 shows that the chemical compositions of the three heats agreed with the AISI 316L grade specification.

The microstructure of the as-received steel heats was first assessed by light optical microscopy (LOM) on steel specimens that were chemically etched with Carpenters' reagent (8.5 g $FeCl_3$, 2.4 g $CuCl_2$, 122 ml HCl, 6 ml HNO_3, 122 ml ethanol) for ~1 min. LOM images of etched 316LSA, 316LH1 and 316LH2 samples are shown in Fig. 1. The average grain size of the three steels was: 45 μm in 316LH1, 65 μm in 316LH2, and varied locally between 30 and 45 μm in 316LSA. The cold-drawn heats 316LH1 and 316LH2 exhibit deformation twins and other features typical for cold-deformed steels. The solution-annealed 316LSA heat shows δ-ferrite stringers parallel to the rolling direction. The phase composition of the as-received 316L steels was determined by X-ray diffraction (XRD; Seifert 3003, GE), using a Cu *K*α radiation source (operating conditions: 40 kV, 40 mA). The XRD patterns (Fig. 2) were acquired in the 30-90° 2θ range with a step size of 0.02° and a time of 2s per step. The only identified phase in all heats was austenite (face-centred cubic, *fcc*; $Fm\overline{3}m$; JCPDS file: 01-071-4649) except for solution-annealed 316LSA, which contained a small fraction of α-ferrite (body-centred cubic, *bcc*; $Im\overline{3}m$; JCPDS file: 03-065-4899). α-ferrite results from the low-temperature (727-738°C) transformation of its high-temperature (>1394°C) polymorph δ-ferrite that is retained in the steel microstructure even after the solution annealing treatment [54,55]. The term δ-ferrite is herein used to denote the high-temperature origin of this steel precipitate.

The microstructure of the as-received cold-drawn steels was characterised on the nanoscale by means of transmission electron microscopy (TEM). The TEM (JEM-3010, JEOL, Japan) was operated at 300 kV using a side-entry type double tilt specimen holder with angular ranges of ±30°. Samples for TEM investigation were prepared from ∅ 3 mm disks punched out of a thin steel slab (~200 μm). These were mechanically polished to 100-130 μm thickness and

electropolished to perforation in a Struers Tenupol 3 (operating conditions: 30 V, 0.2 A, -40°C), using an electrolyte made of 95% CH_3OH (methanol) and 5% $HClO_4$ (perchloric acid).

Fig. 3 shows the two main modes of plastic deformation encountered in all thin foils extracted from the cold-drawn steels, here illustrated for 316LH2: twin and slip deformations. It is known that 316L austenitic stainless steels are *fcc* alloys with relatively low stacking fault energies [56], allowing easy nucleation of deformation twins. Fig. 3a is a bright field (BF) image of a typical set of fine parallel twins laths, while selected-area diffraction over several twin laths (circle in Fig. 3b) along the <1$\bar{1}$0> orientation showed that the twinning plane is {111} (Fig. 3c), in agreement with the reported twinning mode for an *fcc* lattice. Slip in *fcc* crystals occurs in {111} close-packed planes along <110> directions. Fig. 3d shows dislocation pile-up on the {$\bar{1}$11} and {1$\bar{1}$1} slip planes observed near a <110> direction in a large twinless zone confined between two twin boundaries. Fig. 3e was obtained by beam tilting in the {100} plane slightly off the zone axis orientation, where the high density of diffracting dislocations does not allow clear visualization of the slip planes. The observed orientation, close to a 2-beam condition, allows the visualization of two <110> slip planes, while the third one does not show diffraction contrast, since it satisfies the extinction criterion $\vec{g} \cdot \vec{b} = 0$, where $\vec{g}$ is the diffraction vector and $\vec{b} = a/\sqrt{}$<110> is the Burgers vector for an *fcc* lattice. In conclusion, TEM revealed that the as-received cold-drawn 316LH1 and 316LH2 steels were characterized by a high density of twins and dislocations, with higher dislocation density near twin boundaries. Moreover, the two deformation modes (slip and twinning) occurred along the expected close-packed planes. Since fine-scale twinning leads to steel grain fragmentation, it is expected that twin boundaries act as barrier for dislocation motion, resulting to dislocation pile-up.

2.2. Sample Geometry, Dimensions & Surface Finish

The geometry and dimensions of the 316L steel specimens tested in this study are shown in Fig. 4b. Specimens were connected with each other by screw threads (M3); only the last specimen in each set of specimens per test was without thread on one side to minimize machining. All specimens had the following dimensions: ∅ 9 mm, length 10 mm. The specimens were polished with down to 3 μm diamond paste just prior to testing to reduce the surface roughness caused by machining. Even though a mild near-surface steel deformation induced by polishing cannot be excluded, adopting a standardised polishing procedure ensured that the surface quality of all specimens was comparable. The polished specimens were cleaned with acetone and ethanol in an ultrasonic bath, followed by blow-drying with mildly hot air, before specimen insertion to the LBE bath. The visual specimen impression prior to exposure was that of a mirror finish without any trace of ethanol/acetone drying marks. All tests exposed simultaneously specimens made of the three steel heats used in this work (316LSA, 316LH1, 316LH2); for this purpose, sets of specimens connected to each other were introduced in the test setup from a dedicated opening on the lid (Figs. 4a-4b) by means of an 80 cm-long sample holder made of 316L steel.

2.3. Experimental Setup

A schematic representation of the test setup is presented in Fig. 4a. The setup consisted of a stainless steel autoclave with an inner alumina (Al_2O_3) liner (inner diameter 7.4 cm, height 14.3 cm). The alumina liner prevented the direct contact of the steel walls with the LBE volume used for the steel exposure, avoiding its contamination with steel alloying elements that could decrease the instantaneous steel dissolution rates. A small amount of LBE between autoclave walls and alumina liner ensured good thermal conductivity and better temperature control during testing. The stainless steel autoclave was externally heated and thermally insulated to minimise heat losses. The temperature and LBE oxygen concentration were monitored during testing. A thermocouple type K (not pre-oxidised or otherwise protected) monitored the temperature; this thermocouple was connected to the controller that regulated the LBE temperature during testing. The reliability of its output was compared to the output of a second thermocouple type K that measured the temperature on the walls of the stainless steel autoclave. The second thermocouple was connected to an alarm controller that brought the system to a power-down, if the autoclave temperature exceeded a predefined setpoint. Electrochemical oxygen sensors (Bi/Bi_2O_3 reference electrode) fabricated at SCK•CEN monitored the LBE oxygen concentration; Fig. 4c gives a detailed description of these sensors. The oxygen sensor accuracy was previously evaluated [57,58] and was found to improve with temperature. The three-sigma deviation on the measured by the sensors electric potential difference was about 4 mV [57]. At 500°C, this standard deviation results in ~12% error on the LBE oxygen concentration, which is calculated from the measured by the sensors electric potential difference. The LBE oxygen concentration was calculated using the following equations [57]:

$$\Delta U - \Delta U_{th} = -0.34756 + 2.5217\times10^{-4}\cdot T - 4.3087\times10^{-5}\cdot T\cdot \ln C_O \quad (1)$$

$$\Delta U_{th} = -6.91\times10^{-3} + 1.762\times10^{-5}\cdot T \quad (2)$$

where ΔU is the electric potential difference measured by the oxygen sensor in V, ΔU_{th} is the thermoelectric potential between stainless steel and Mo wire in V, T is the absolute temperature in K, and C_O is the LBE oxygen concentration in mass%.

The autoclave lid had various openings to insert specimens, oxygen sensor, thermocouple, and to allow the inlet/outlet of the conditioning gas (Figs. 4a-4b). Specimen insertion in the LBE bath was done via a dedicated tube welded on the lid, under leak-tight conditions, with the help of a stainless steel valve (1-piece 40 series ball valve; 12 mm Swagelok tube fitting; SS-45S12MM). A pre-oxidized stainless steel tube supplied the reducing conditioning gas at a distance of ~2.5 cm from the steel specimens and close (< 1 cm) to the bottom of the LBE bath. Gas supply close to the bath bottom resulted in mild LBE mixing, making the test conditions 'quasi-static' rather than truly static. The conditioning gas (HYTEC 5: Ar-5%H_2, Rapid Industrial Gases Ltd., UK) was a certified gas made of 95% Ar with 5% H_2 and minor oxygen-containing impurities (O_2 < 10 ppm, H_2O < 10 ppm).

2.4. Exposure Conditions

316L steel specimens were exposed to oxygen-poor (mostly C_O < 10^{-8} mass%), static LBE at 500°C for the following times: 253, 501, 1000, 1003, 2055 and 3282 hours. All tests exposed 4 steel specimens simultaneously (1 specimen per heat plus an additional specimen arbitrarily selected from one of the 3 heats), except for the longest test (3282 h) that tested a set of 9 steel specimens (3 specimens per heat). The distance of the specimens from the bottom of the LBE bath was 1 cm for the longest exposure (3282 h) and 6 cm for all other exposures.

Each test used ~5 kg of 'fresh' LBE, so as to ensure that LBE contamination from an earlier test did not affect the results of the next one. The main impurities in the as-received LBE (analysed as 55.3% Bi, 44.7% Pb) were Si (< 2700 mg/kg), F (< 90 mg/kg), Ag (~19 mg/kg), S (< 9 mg/kg), Cu (~7 mg/kg), Ni (< 3.2 mg/kg), Hg (~2.4 mg/kg), Fe (< 2.4 mg/kg), Nb (< 2.4 mg/kg) and Ge (< 2.1 mg/kg). The ratio of the steel specimen surface to the LBE volume used for testing varied between 0.023 and 0.051 cm^{-1} for the tests that exposed 4 and 9 specimens, respectively. This calculation takes into account the temperature dependence of the LBE density, ρ_{LBE} [1]:

$$\rho_{LBE}\ (kg/m^3) = 11096\text{-}1.3236 \cdot T \quad (3)$$

where T is the absolute temperature in K.

In all tests, the exposure temperature was kept constant at ±2°C from the targeted temperature of 500°C, while continuous purging with Ar-5%H_2 maintained a low LBE oxygen concentration (mostly C_O < 10^{-8} mass%). The evolution of LBE oxygen concentration during all tests is shown in Fig. 5. Since the LBE oxygen concentration varied roughly between 5×10^{-13} and 2×10^{-8} mass% during the performed tests, the formation of certain oxides, such as Cr_2O_3 (stable above 10^{-15} mass% at 500°C [11]) and $FeCr_2O_4$ (stable above 10^{-12} mass% at 500°C [11]), could, in principle, not be excluded. An LBE preconditioning treatment lowered the oxygen concentration below 10^{-8} mass% prior to the insertion of the steel specimens in the LBE bath (Fig. 6). This minimised steel oxidation that would probably delay the occurrence of dissolution corrosion. Despite the low C_O during sample insertion, the immersed steel specimens acted as oxygen getters, further reducing the C_O (Fig. 6), which suggests that steel oxidation was not completely prevented.

2.5. Post-Test Analysis

Metallographic cross-sections were prepared from all exposed 316L steel specimens; a mirror surface finish was achieved by polishing the specimen cross-sections with 1 μm diamond paste in the last step. Some of the polished cross-sections underwent an additional polishing step using a colloidal silica (OPS) suspension, which created a subtle surface relief on the steel cross-sections, facilitating the study of the interplay of the dissolution corrosion process with the steel microstructure by LOM (Axio Scope.A1, ZEISS International). The 316L dissolution corrosion behaviour was primarily studied by LOM, scanning electron microscopy (SEM; JSM-6610LV, JEOL, Japan) and energy dispersive X-ray spectroscopy (EDS; XFlash detector 4010, Bruker AXS GmbH, Germany). A more in-depth study of specific areas involved the deployment of high-resolution

electron backscatter diffraction (EBSD; Hikari XP EBSD camera, EDAX, USA, on a FEI Nova NanoSEM 450, FEI, USA); in select cases, thin foils were made by focused ion beam (FIB; FEI Helios Nanolab 650, FEI, USA) and investigated by TEM (JEM-3010, JEOL, Japan). Corrosion quantification was attempted by measuring (a) the surface recession by LOM, i.e., comparing the initial specimen diameter with the diameter of the unaffected steel, and (b) the thickness of the dissolution-affected zone by SEM. The first method was unsuccessful due to the limited resolution of light optical profilometry that was used to measure the initial specimen diameter. This work reports only on the thickness of the dissolution-affected zone, as measured by SEM on 1-3 cross-sections per specimen. Depending on the time-dependent severity of attack, SEM pictures were taken at magnifications that allowed the accurate quantification of corrosion. The pictures were able to reconstruct the whole cross-section and the thickness of the dissolution-affected zone was measured on many (randomly-chosen) locations per picture. Typically, 200-500 measurements were collected per cross-section to ensure reliable statistics. Apart from the thickness of the dissolution-affected zone, another parameter used to quantify corrosion in this study was the percentage of the steel specimen surface that was affected by dissolution.

3. Results & Discussion

3.1. General Observations of Corrosion Damage

The evolution of damage with exposure time is depicted in the SEM images of Fig. 7 for one of the cold-drawn steels (316LH1; the results were similar to those acquired from 316LH2) and Fig. 8 for the solution-annealed steel 316LSA. The dissolution front, i.e., the interface between the dissolution-affected zone and the unaffected steel, was in general more perturbed in the cold-drawn steel than the solution-annealed one, for all exposure times. Moreover, the cold-drawn steel was more prone to locally-enhanced dissolution attack, exhibiting a non-negligible number of pit-like features similar the one shown in Fig. 7f. Even though these features did not form as the result of conventional pitting corrosion, they will hereafter be referred to as 'pits' due to the fact that the depth of attack at their location was much deeper than the depth of attack in their immediate vicinity. The thickness of the dissolution-affected zone increased with exposure time for all steel heats, as expected. At any exposure time, corrosion was invariably deeper in the cold-drawn steels than in the solution-annealed one, underlying the importance of the steel thermomechanical state. Moreover, the percentage of the steel specimen surface affected by corrosion increased with the exposure time for all steel heats. After 253 h, 90% of the specimen surface of the solution-annealed 316LSA steel and 80% of the cold-drawn 316LH1 and 316LH2 steels was affected by dissolution corrosion. After 501 h, 100% of the specimen surface of the 316LSA and 90% of the 316LH1 and 316LH2 was affected. In all exposures longer than 1000 h, 100% of the surface of all steel specimens was affected by dissolution attack.

Figs. 7 and 8 show that LBE dissolution attack does not progress perpendicular to the specimen surface, but constantly changes direction, following paths of preferential ingress into the base or

unaffected steel. These paths include grain boundaries, deformation twins, and various steel precipitates, the formation and orientation of which is associated with the steel production and deformation processes, respectively. The interplay between the steel microstructure and the dissolution process is largely responsible for the intricacy of the dissolution front and the non-uniform thickness of the dissolution-affected zone. The effect of the steel microstructure on the dissolution corrosion behaviour of 316L steels is extensively addressed in section 3.4.

Differences in the thickness of the dissolution-affected zone were observed on all specimen cross-sections, irrespective of the exposure time and the steel heat. Very often, this thickness was observed to vary significantly over relatively short distances, as shown in Figs. 7a and 7e, suggesting that dissolution attack started at a different moment in areas separated by only a few micrometres. In first instance, differences in the time dissolution attack begins on the steel surface could be associated with the local vulnerability of the oxide scale. Despite the fact the tests performed in this study were designed to promote dissolution corrosion, one cannot assume the complete absence of an oxide film from the steel surface: whether this is a native oxide (possibly reforming in the time between sample polishing and immersion to the LBE bath) or forms upon specimen immersion in the LBE bath (see Fig. 6), one expects that dissolution attack will start as soon as this oxide film is locally degraded. This means that the incubation period for LBE dissolution attack will vary across the specimen surface, a fact that would explain to a certain extent the observed differences in the thickness of the dissolution-affected zone.

It falls outside the scope of this study to discuss possible causes of oxide scale failure, also in view of that fact that the evidence of oxide scale formation was very limited. An example of oxide scale formation is given in Fig. 7f, where discontinuous FeCr-containing oxide scales (only the Fe and Cr maps are shown, but EDS confirmed that the Fe/Cr-enriched layer was an oxide) were found on top of a deep (~258 µm) 'pit'. The origin of these oxides is not clear; however, Schroer et al. [12] had previously suggested that oxides might form above the dissolution-affected zone by the oxidation of steel alloying elements that are leached out of the steel. The same authors proposed that defective oxides act as sinks for outward diffusing steel alloying elements, maintaining concentration gradients that are favourable for the further steel depletion and keeping oxygen away from the depletion zone. In another study, Schroer et al. [13] suggested that LBE penetrations become very poor in oxygen as dissolution attack deepens, eventually inhibiting the reprecipitation of Cr-based oxides inside the depletion zone. This promotes the outward diffusion of Cr, which results in the formation of Cr-containing oxides similar to the ones observed in Fig. 7f on top of the depletion zone.

The formation of 'pits' similar to that in Fig. 7f is a concern for the reliable use of austenitic stainless steels in LBE-cooled nuclear systems, especially for thin-walled components such as heat exchanger tubes and fuel cladding tubes. Locally-enhanced dissolution, herein named dissolution 'pitting', has been reported to occur under a seemingly intact oxide scale, even in conditions of flowing, adequately-oxygenated LBE. The underlying cause of the occurrence of dissolution

'pitting' in 316L steels exposed to liquid LBE is the local failure of the oxide scale [12-14,17,18,21,59]. Oxide scale failure allows the LBE permeation to the oxide/steel interface, which is often enriched in highly-soluble species such as Cr and/or Ni [13,14]. The latter might account for the quick lateral expansion of the 'pit' and explain its typically large diameter (Fig. 7f). Once nucleated, the 'pit' grows by various possible mechanisms [12,13] and resealing by oxidation is practically impossible. The frequency of dissolution 'pitting' increases as the T and LBE flow velocity increase and the LBE C_O decreases, in agreement with the theories attributing its occurrence to local oxide failure, which is also promoted at high temperatures, high LBE flow velocities and low LBE oxygen concentrations. This study also demonstrates that the local steel microstructure can trigger dissolution 'pitting' (see section 3.4.2).

Dissolution corrosion usually started by LBE intergranular penetration into the grain boundaries with access to the steel surface (Figs. 9a-9c). Prior studies on the intergranular penetration of liquid metals into solid metals, in the absence of external stresses, suggested the existence of a wetting transition temperature, T_w, above which the liquid metal wets the grain boundaries and below which it diffuses into the grain boundaries [60-63]. The driving force for intergranular penetration is the reduction in the overall energy of the system, which is achieved when the surface energy of the solid/liquid interfaces (γ_{sl}) is smaller than the energy of the initial grain boundary (γ_{gb}), i.e., when $2\gamma_{sl} \leq \gamma_{gb}$. It falls outside the scope of this work to determine whether the intergranular LBE penetration into the exposed 316L steels qualifies as wetting or diffusion, also in view of the complexity of a dedicated investigation; such investigation is usually conducted by exposing pure (solid) metals to liquid metals saturated in the metals they contact, hence the steel/LBE system is clearly too complex to address, due to the presence of impurities in both steel and LBE and the forbidding cost of producing model alloys of high purity.

Intergranular LBE penetration into the near-surface layer of grains (Figs. 9a-9c) is followed by the further LBE penetration into the steel along preferential LBE ingress paths. The appearance of the dissolution-affected zone in the early stages of attack is very intricate, almost 'lace-like', whereupon planes of LBE penetration cross-link with grains that are intergranularly attacked (Fig. 9b). As dissolution corrosion advances, the continuous interplay of the steel microstructure with the dissolution process ensures the propagation of damage deeper into the steel (Fig. 10). This is reflected in the continuous change in the direction of attack, depending on the local orientation of the favourable paths for LBE ingress into the unaffected steel (Fig. 10).

3.2. Kinetic Data

Increasing the exposure time from 253 h to 3282 h increased the maximum depth of dissolution attack from 21 µm to 152 µm for the 316LSA steel, from 33 µm to 346 µm for the 316LH1 steel, and from 48 µm to 265 µm for the 316LH2 steel. The evolution of the maximum depth of dissolution attack as function of the exposure time is shown in Fig. 11a. As already mentioned, the maximum dissolution depth provides an estimate of the maximum dissolution rate of 316L steels at 500°C, which is important for the lifetime prediction of thin-walled components. The

experimental data were fitted based on a model that assumes a decrease in the dissolution rate, $\frac{dx}{dt}$, with the depth of dissolution, x, according to the following equation:

$$\frac{dx}{dt} = Kx^a \quad (4)$$

where K and a are two constants. Integration of equation (4) gives:

$$x = A(t - t_0)^c \quad (5)$$

where $c = \frac{1}{-a+1}$, $A = \left(\frac{K}{c}\right)^c$, and t_0 is the incubation time. Fitting of the three variables *A*, *c* and t_0, for both maximum and average dissolution depth, was performed using the Levenberg-Marquardt iteration algorithm. Note that $c \approx 0.5$ for the maximum depth, which means that the maximum dissolution rate is inversely proportionate to the dissolution depth:

$$\frac{dx}{dt} \approx \frac{K}{x} \quad (6)$$

The above analysis shows that LBE dissolution attack is decelerated as the dissolution depth increases, probably due to the fact that the outward diffusion of steel alloying elements must occur through an increasingly thicker dissolution zone. The instantaneous maximum dissolution rate decreased from 6.62×10^{-2}, 1.50 and 2.09×10^{-1} μm/h after 253 h to 1.75×10^{-2}, 4.56×10^{-2} and 3.58×10^{-2} μm/h after 3282 h for the 316LSA, 316LH1 and 316LH2 steels, respectively. The fact that 316LH1 dissolves faster than 316LH2 might partly be attributed to the fact that 316LH1 was finer-grained than 316LH2, as dissolution corrosion advances via intergranular LBE penetration. On the other hand, the faster attack in the cold-drawn steels as compared to the solution-annealed steel is associated with the acceleration of the dissolution process by the presence of deformation-induced defects in the steel microstructure (see section 3.4.2).

Yamaki et al. [15] have previously exposed specimens of the EUROTRANS-DEMETRA 316L steel heat, i.e., the 316LSA steel in this work, to oxygen-poor static LBE at 500°C for 170-3045 h. They reported linear dissolution kinetics and observed two modes of dissolution attack, a slower and a faster one. The determined by Yamaki et al. [15] corrosion rate for the faster mode was 147 μm/year, while the maximum dissolution rate determined for the 316LSA steel is 187 μm/year. The 21% faster dissolution rates observed in this work compared to the work of Yamaki et al. [15] might be associated with the fact they used a less reducing gas during testing (i.e., Ar-4%H_2 instead of the Ar-5%H_2 used here). In fact, Yamaki et al. [15] reported that the LBE oxygen concentration was kept at $C_O < 10^{-8}$ mass%, but did not actually measure it by oxygen sensors, so a direct comparison of the C_O conditions between the two studies is impossible. An indication that the exposure conditions were more reducing in the present work is that the maximum dissolution depth was ~100 μm after 3282 h, while Yamaki et al. [15] reported this to be ~60 μm after 3045 h. It is also worthwhile mentioning that linearity seems to be maintained up to a critical dissolution zone thickness, which is estimated to be ~70 μm in this study; for thicker dissolution zones, the rate decreases and the outward elemental diffusion becomes the rate-limiting step.

This agrees with the findings of Yamaki et al. [15] who suggested linear kinetics for dissolution depths < 60 µm.

Yamaki et al. [15] reported an incubation time of 112 h for the faster dissolution mode, while this study estimated the incubation time to be ~25 h; this might also be related with the fact that the exposure conditions were more reducing in this work than in the work by Yamaki et al. [15]. The different incubation times – with an uncertainty due to the limited data – determined for the maximum dissolution depth was 244 h, 161 h and 25 h for 316LH1, 316LH2 and 316LSA, respectively. It is not yet clear why the incubation time varied so much between steel heats. One might assume that this is caused by the different protectiveness of oxide scales on cold-deformed vs. solution-annealed steels; however, this assumption merits further investigation.

Prolonging the exposure from 253 h to 3282 h increased the average depth of dissolution attack from 6.5±3.9 µm to 73.5±13.3 µm for the 316LSA steel, from 12.9±6.6 µm to 286.8±29.7 µm for the 316LH1 steel, and from 18.1±8.5 µm to 177.5±25.5 µm for the 316LH2 steel (Fig. 11b). The scatter in the dissolution zone thickness values can partly be associated with the fact that the LBE oxygen concentration differed from test to test (Fig. 5). Moreover, during each test, local LBE oxygen concentration gradients cannot be excluded, due to the lack of efficient LBE mixing. Also, the observed scatter in dissolution depth can be associated with the local vulnerability of the oxide scale, steel microstructure (section 3.4) and steel chemical composition (section 3.3).

3.3. Dissolution Mechanisms: Selective Leaching vs. Non-Selective Leaching

3.3.1. Selective Leaching and Steel Ferritization

Dissolution attack usually started with intergranular LBE penetration, followed by the selective leaching of the Ni, Mn and Cr from the affected grains; the Fe-based residual grains were then consumed by LBE at a slower pace. Selective leaching of Ni, Mn and Cr is driven by the greater solubility of these elements in LBE when compared to the solubility of Fe. Martinelli et al. [64] has experimentally assessed the maximum solubility of Ni in LBE to be ~2.98 mass% at 500°C; the suggested Ni solubility (in mass%) in the 415-900°C range is given by the following equation:

$$\log S_{\mathrm{Ni}} = 1.7 \pm 0.08 - \frac{1009}{T} \quad (7)$$

where *T* is the absolute temperature in K.

Gossé [65] has performed a thermodynamic assessment of the Ni, Cr and Fe solubility limits in LBE in contact with the $Fe_{0.71}Cr_{0.18}Ni_{0.11}$ model alloy, which is compositionally similar to the 316L steel. He found that the Ni solubility is the highest; the Cr solubility is 10^2 times lower than that of Ni in the 227-727°C range; and the Fe solubility is 10^3 times lower than that of Ni at 227°C, this gap reducing with temperature. The Ni, Cr and Fe solubilities (in at.%) can be calculated using equations (8)-(10), where *T* is the absolute temperature in K:

$$\log S_{\mathrm{Ni}} = -11.904 + \frac{12662.2}{T} - \frac{6209 \times 10^3}{T^2} + \frac{794.55 \times 10^6}{T^3} + 2.725 \times 10^{-3} T \quad \text{(232-900°C)} \quad (8)$$

$$\log S_{Cr} = -1.2582 - \frac{2269.2}{T} \quad \text{(230-900°C)} \quad (9)$$

$$\log S_{\mathrm{Fe}} = 0.2224 - \frac{4104.2}{T} \qquad (126\text{-}900°C) \qquad (10)$$

The Ni, Cr and Fe solubilities at 500°C were calculated using equations (8)-(10) and converted to mass%; according to these calculations, the Ni, Cr and Fe solubilities are 2.30×10^{-1}, 1.60×10^{-3} and 2.19×10^{-4}, respectively. Even though the Ni solubility in LBE decreases when other elements (Cr, Fe) are also dissolved in the HLM, it remains high and capable of driving the Ni dissolution process. EDS line scans illustrating the selective leaching of Ni, Mn and Cr from intergranularly-attacked grains are shown in Figs. 12c and 14d. The selective removal of Ni, Mn and Cr increases the Fe content of the affected grains relative to the unaffected steel. The same EDS line scans show grain boundary decoration by Pb and Bi. A consequence of the selective removal of the austenite stabilizers Ni and Mn is steel ferritization, i.e., the transformation of the original austenitic (*fcc*) grains to ferritic (*bcc*) ones. A TEM proof of ferritization is provided in Figs. 9d-9f. Usually, ferritization is accompanied by grain refinement of the dissolution-affected zone with respect to the grain size of the unaffected steel (Figs. 15c-15d).

3.3.2. Non-Selective Leaching

Non-selective leaching was mainly observed locally in the solution-annealed 316LSA steel (Figs. 13b-13d). Interestingly, the alternation of areas of selective leaching with areas of non-selective leaching often occurred over a short distance (Fig. 13). This was quite puzzling and explaining it by suggesting a periodic failure of the oxide scale on the steel surface would be farfetched. The short-range transition from selective to non-selective leaching is currently attributed to local variations in the steel chemical composition. Compositional fluctuations in industrial-size steel heats are associated with interdendritic segregation during solidification from the melt, and are maintained during hot rolling of the casting [55]. It has been previously suggested [12,13,59] that there is a threshold concentration of highly-soluble elements, such as Ni, above which selective leaching is promoted and below which non-selective leaching prevails. However, recent ongoing studies have shown that steel compositional differences are associated with differences in the local steel deformability and, hence, in the local steel susceptibility to dissolution attack. The study of steel chemical banding on 316L dissolution corrosion is still ongoing and its results will be reported when this study is complete.

3.4. Effect of Steel Microstructure

3.4.1. Three-Dimensionality of Steel Microstructure

Corrosion quantification often involves measuring the depth of attack on metallographic cross-sections that give a two-dimensional impression of the three-dimensional steel microstructure. This may introduce errors in the estimation of the true corrosion rate, as the path of LBE ingress is non-linear and corrosion evolves by interconnecting LBE penetrations in the 3D steel volume. Interconnectivity is achieved by cross-linking paths of preferential LBE penetration into the base steel, such as grain boundaries and deformation twins (Figs. 10, 12, 14). Examples of the way LBE dissolution attack relies on the three-dimensionality of the steel microstructure to further

advance are shown in Fig. 14. Often, 'bridges' connect the main dissolution-affected zone with 'islands' of affected grains several micrometres from the main dissolution front (Figs. 14a-14b).

3.4.2. Grain Boundaries and Deformation Twin Boundaries

LBE dissolution attack usually starts with LBE intergranular penetration, especially in the case of selective leaching (Figs. 9, 12, 13a). Since grain boundaries are characterised by atomic disorder and many defects (dislocations, point defects, small voids, impurities), they become favourable paths for LBE penetration, presumably because they ensure faster elemental diffusion than the comparatively defect-free grain bulk [66]. As observed in this study, finer-grained steels are characterised by higher dissolution rates than coarser-grained ones (Fig. 11). The steel grain size distribution must thus be optimized before a 316L steel can be used in contact with LBE.

The LOM investigation of the dissolution front in cold-drawn steels revealed LBE penetrations that followed parallel, closely-spaced striations within the same grain (Figs. 15a-15b). The high-resolution EBSD study of such a grain showed that the micro-volumes confined between two consecutive striations had a different crystallographic orientation than the grain bulk (Fig. 15c). EBSD confirmed the ferritization of the dissolution-affected zone, illustrating grain refinement of the dissolution-affected zone with respect to the grain size of the unaffected steel (Fig. 15d). In order to elucidate the nature of the closely-spaced striations in the grain of Fig. 15c, two thin foils were prepared by FIB for further TEM study: one taken exactly at the dissolution front (area 1, Fig. 16a) and one away from the dissolution front (area 2, Fig. 16a), both along the same set of striations. The SEM image of Fig. 16b shows the FIB foil from area 1, revealing that an LBE penetration follows the edge of a set of parallel thin lines in the steel. Since these lines were also visible in the cross-section of Fig. 16a, it appeared they were actually planes extending deep into the base steel below the plane of the cross-section in Fig. 16a. The observed gaps are partly formed during FIBing, since LBE is easier to remove by ion beam milling than the steel, creating cavities in spaces filled by LBE. The gaps might have also formed by the post-freezing expansion of the LBE residues, which is associated with the formation of a mixture of phases β (Pb_7Bi_3) and γ (Bi with 0.4% Pb); after some time, the close-packed β-phase transforms into the less dense γ-phase, resulting in the opening of LBE-filled spaces [67]. The FIB foil from area 1 was studied by TEM, after thinning to electron transparency. Fig. 17a provides an overview of this foil. A selected area diffraction pattern (SADP) taken over the area outlined by a circle in Fig. 17a showed set of twins in the $<1\bar{1}0>$ orientation (Fig. 17b). This SADP is identical to the pattern in Fig. 3c, be it with a lower intensity and thus finer twin width for one of the variants, confirming the {111} twin nature. The FIB foil taken from area 2 showed the same set of twins as in area 1; the orientation of this set of twins was confirmed by selected area diffraction (not shown here).

Several BF images were taken at higher magnification along the LBE penetration path from the foil in area 1 and were assembled (Fig. 17c) to cover the zone within the rectangular frame in Fig. 17a. Several EDS point analyses were done along the LBE penetration and its surroundings (Fig. 17e): sites A-C correspond to pure LBE locations, while sites D-F correspond to unaffected steel

locations (i.e., no depletion in Ni or Cr). The overview BF image of Fig. 17c illustrates the mechanism of LBE penetration between twin laths: LBE travels in the direction parallel to the close-packed twinning planes, while remaining bounded by the two neighbouring twin boundaries and leaching out steel alloying elements only within the attacked twin lath. At several locations, steps are observed at the borders between LBE penetration and stainless steel matrix. The orientation of such steps with respect to the {111} twin plane is reflected in Fig. 17d: traces of slip planes at an angle of ~70° with the trace of the {111} twin plane are visible in some of the twin laths on the left hand side of Fig. 17d. The angle is consistent with the theoretical angle between close-packed planes {111} and $\{11\bar{1}\}$ along this zone axis. It appears that the steps are aligned parallel to the direction of the slip plane traces visible within the twin laths. The following mechanism can thus be tentatively proposed to describe the twin lath-facilitated LBE penetration in cold-worked 316L steels: LBE penetration starts from a preferential site within a narrow twin lath. While the LBE penetration remains constrained between consecutive twin walls at the penetration front, it can bear its way into a neighbouring twin lath by following close-packed slip planes crossing the twin walls along the length of the LBE penetration, where a faster diffusion of dissolved steel species is possible.

Experimental evidence of the contribution of the steel microstructure to dissolution 'pitting' is provided in Fig. 18. LOM located a 'pit' (maximum depth ~84 µm) in an area where the depth of dissolution did not exceed ~28 µm (Figs. 18a-18b). The surface relief achieved by OPS polishing revealed that the 'pit' growth was guided by the local convergence of certain boundaries in the steel. These boundaries were associated with large (160-220 µm) grains that resulted in a much deeper dissolution attack locally compared with the depth of attack in the immediate vicinity of the 'pit'. EBSD confirmed that these boundaries were twin boundaries (Fig. 18d), while EDS analysis of the same area identified the areas where LBE was present (Fig. 18e – Bi map).

3.4.3. Steel Precipitates

Manganese sulphide (MnS), oxides and δ-ferrite precipitates are often encountered in 316L stainless steels; hence, their interaction with the dissolution corrosion process is interesting, as it has been suggested that "near-surface inclusions, such as MnS or slag (i.e., oxide) particles, might account for the local breakdown of the protective oxide scales formed on 316L stainless steels during their exposure to liquid LBE" [13]. Fig. 19 shows typical examples of the observed lack of interaction between MnS, oxides and δ-ferrite precipitates and LBE. First, MnS inclusions remained immune to LBE dissolution attack even after prolonged exposures, as suggested by the presence of intact particles at large distances from the dissolution front (Fig. 19a). This means that MnS was practically insoluble in LBE at 500°C; therefore, particles close to the steel surface could not contribute to the local breakdown of oxide scales and the onset of 'pitting' by their own dissolution in LBE. It is possible, however, that the MnS/steel interface facilitated the LBE ingress into the steel, thus contributing to the onset of dissolution attack for inclusions situated close to the steel surface. Such hypothesis merits further investigation.

Oxide precipitates were also resilient to LBE dissolution attack, remaining intact while the steel matrix that envelops them is severely attacked (Fig. 19c). Elongated (stringer-like) oxide ('slag') precipitates aligned parallel to the steel rolling direction were only observed in the solution-annealed 316LSA steel. EDS elemental analysis showed them to be Al_2O_3-based with variable Mg, Si and Ca contents (Fig. 19d). Oxide 'stringers' were often observed in the centre of nodular perturbations of the dissolution front (Fig. 19c). This suggests that the oxide/steel interface is a path of preferential LBE ingress into the steel; once LBE decorates that interface, the dissolution front advances locally, forming nodular perturbations along the length of the oxide 'stringer'.

The interaction of δ-ferrite with LBE is similar to that of oxide inclusions: δ-ferrite resists better LBE dissolution attack than the base steel (Figs. 19e-19f), and the δ-ferrite/steel interface is a path of preferential LBE ingress into the steel. The better compatibility of δ-ferrite with LBE can be associated with the fact it contains less highly-soluble alloying elements than the base steel (i.e., ~9% Cr in δ-ferrite as opposed to 10-14% Ni, 2% Mn and 16-18% Cr in the base steel).

3.4.4. 'Notches'

Selective leaching of the austenite stabilizers Ni and Mn results in ferritization, i.e., the phase transformation of austenite (*fcc*) to ferrite (*bcc*). The *fcc*-to-*bcc* phase transformation is probably accompanied by a volumetric change, which will cause stress triaxiality in the immediate vicinity of sharp protuberances of the dissolution front, such as the ones shown in Fig. 20. Whether the volumetric change is expansion [67] or contraction, the stress field around sharp protrusions of the dissolution front is characterised by a stress intensity factor K_I that depends on the externally-applied load and the size of the protrusion, in agreement with linear-elastic fracture mechanics. When K_I approaches a critical value, K_c, fracture occurs due to unstable crack growth [68]. Such features may be considered as internal steel 'notches' that act as stress concentrators in notch-sensitive metals (e.g., pure Fe), interacting with dislocation motion under an externally-applied load that exceeds the yield strength, and initiating brittle failure [69]. Even though 316L steels (*fcc* alloys) are probably notch-insensitive, they suffer irradiation embrittlement [70-73], becoming notch-sensitive in service. Hence, the presence of corrosion-induced sharp notches (Fig. 20) is expected to be a concern for irradiated 316L steels and, in particular, for thin-walled components, where unstable crack propagation might easily lead to failure.

Even non-irradiated austenitic stainless steels show a greater propensity towards brittle fracture after dissolution-induced ferritization, as reported by Müller et al. [19] and Schroer et al. [12], but the cracks are arrested in the ductile austenitic matrix of the unaffected steel. This is not surprising considering that the dissolution-affected zone is ferritized and that ferritic steels (e.g., T91 and similar steels) are known to be susceptible to liquid metal embrittlement (LME) [74-76]. The onset of brittle fracture in the LME-prone dissolution-affected zone is expected to propagate fast in irradiation-hardened steels, as the capacity of the steel matrix to blunt cracks reduces in a neutron environment. Naturally, these assumptions must be validated by means of a dedicated study on the potential synergy of dissolution corrosion, LME, and irradiation.

4. Conclusions

In this work, different 316L austenitic stainless steel heats, both solution-annealed and cold-deformed, were exposed to oxygen-poor (C_O < 10^{-8} mass%), static liquid LBE for 253-3282 h at 500°C, so as to understand the grade-specific dissolution corrosion behaviour of 316L steels. Under the specific exposure conditions (T = 500°C, C_O < 10^{-8} mass%), dissolution corrosion was the prevailing liquid metal corrosion mechanism, indicating that any possible oxide scales were not protective. The dissolution zone thickness was non-uniform and deep pit-like features formed in various locations on the steel surface; some of the 'pits' were covered by FeCr-containing oxide residues. The main findings of this work could be summarised as follows:

1. Corrosion was invariably deeper in the cold-drawn steels than in the solution-annealed one for identical exposure conditions. The higher susceptibility of the cold-drawn steels to dissolution attack was associated with the presence of deformation-induced defects, such as twin laths, that acted as paths of preferential LBE ingress into the steel.
2. The prevailing dissolution mechanism for all steels was selective leaching of Ni, Mn and Cr, which resulted in ferritization of the dissolution-affected zone. Non-selective leaching was observed in the solution-annealed steel together with selective leaching. The manifestation of non-selective leaching in the solution-annealed steel was attributed to compositional inhomogeneities typical of industrial-size steel heats.
3. Analysis of the experimental data showed that the maximum dissolution rate was inversely proportionate to the dissolution depth. Deceleration of dissolution corrosion is observed when the dissolution zone exceeds a critical thickness (~70 μm), i.e., when the outward diffusion of dissolved elements becomes the rate-limiting step. The short incubation times (25-250 h) confirmed the effectiveness of the testing approach in promoting dissolution.
4. A strong interplay of the dissolution corrosion process with the steel microstructure was observed, whereupon LBE penetration occurred along preferential paths in the steel, such as grain boundaries and deformation twins. Dissolution corrosion progressed fastest in the finer-grained cold-drawn steel and slowest in the solution-annealed steel.

Acknowledgments

The authors would like to acknowledge the following 316L stainless steel suppliers: Industeel, ArcelorMittal Group, for the 316LSA plate procured and characterised in the FP6 EUROTRANS-DEMETRA project (Contract no. FI6W-CT-2004-516520); OLARRA Aceros Inoxidables, Spain, for the 316LH1 rod; and SIDERO STAAL nv, Belgium, for the 316LH2 rod. K. Lambrinou would like to thank J. Joris for technical support during the launching and follow up of all corrosion tests, J. Lim for the manufacturing and calibration of the oxygen sensors used in these tests, T. Lapauw for the XRD measurements on the pristine steels, and S. Van den Broeck for the FIB sample preparation. Special thanks to S. Gavrilov for fruitful and intense discussions. The authors gratefully acknowledge the funding provided in the framework of the ongoing development of the MYRRHA

irradiation facility. The research leading to these results falls within the framework of the European Energy Research Alliance Joint Programme on Nuclear Materials (EERA JPNM).

References

[1] F.J. Martín-Muñoz, A. Heinzel, A. Weisenburger, G. Müller, S. Gavrilov, K. Lambrinou, Compatibility of structural materials with lead-bismuth eutectic and lead: Standardisation of data, corrosion mechanism and rate, in: Handbook on lead-bismuth eutectic alloy and lead properties, materials compatibility, thermal hydraulics and technologies, 2015 edition, OECD/NEA, 2015, pp. 431-485.

[2] N. Li, Lead-alloy coolant technology and materials – technology readiness level evaluation, Prog. Nucl. Energ. 50 (2008) 140-151.

[3] J. Zhang, A review of steel corrosion by liquid lead and lead-bismuth, Corros. Sci. 51 (2009) 1207-1227.

[4] J. Konys, W. Krauss, C. Schroer, H. Steiner, Z. Voß, O. Wedemeyer, Corrosion of structural materials in liquid lead alloys for nuclear applications, Corrosion 63 (2007) 1124-1137.

[5] A. Weisenburger, C. Schroer, A. Jianu, A. Heinzel, J. Konys, H. Steiner, G. Müller, C. Fazio, A. Gessi, S. Babayan, A. Kobzova, L. Martinelli, K. Ginestar, F. Balbaud-Célerier, F.J. Martín-Muñoz, L. Soler-Crespo, Long term corrosion on T91 and AISI1 316L steel in flowing lead alloy and corrosion protection barrier development: Experiments and models, J. Nucl. Mater. 415 (2011) 260-269.

[6] L.A. Weinstein, J. Loomis, B. Bhatia, D.M. Bierman, E.N. Wang, G. Chen, Concentrating solar power, Chem. Rev. 115 (2015) 12797-12838.

[7] H. Aït Abderrahim, D. De Bruyn, G. Van den Eynde, S. Michiels, Transmutation of high-level nuclear waste by means of accelerator driven system, in: R. Stock (Ed.), Encyclopedia of Nuclear Physics and its Applications, 1st edition, 2013, Wiley-VCH Verlag GmbH & Co. KGaA, pp. 689-704.

[8] C. Schroer, O. Wedemeyer, J. Konys, Aspects of minimizing steel corrosion in liquid lead-alloys by addition of oxygen, Nucl. Eng. Des. 241 (2011) 4913-4923.

[9] M. Caro, K. Woloshun, F. Rubio, S.A. Maloy, P. Hosemann, Heavy liquid metal corrosion of structural materials in advanced nuclear materials, JOM 65 (2013) 1057-1066.

[10] P. Hosemann, R. Dickerson, P. Dickerson, N. Li, S.A. Maloy, Transmission electron microscopy (TEM) on oxide layers formed on D9 stainless steel in lead bismuth eutectic (LBE), Corros. Sci. 66 (2013) 196-202.

[11] C. Schroer, J. Konys, Physical chemistry of corrosion and oxygen control in liquid lead and lead-bismuth eutectic, Wissenschaftliche Berichte FZKA 7364, Forschungszentrum Karlsruhe in der Helmholtz-Gemeinschaft, 2007, pp. 17-28.

[12] C. Schroer, O. Wedemeyer, J. Novotny, A. Skrypnik, J. Konys, Selective leaching of nickel and chromium from type 316 austenitic steel in oxygen-containing lead-bismuth eutectic (LBE), Corros. Sci. 84 (2014) 113-124.

[13] C. Schroer, E. Nold, J. Konys, Micro-analysis of 316L stainless-steel after long-term exposure to lead-bismuth eutectic at 550°C, in: Proc. European Corrosion Congress (EUROCORR 2009), CEFRACOR, 2010, Vol. 3, pp. 2062-2069.
[14] C. Schroer, J. Konys, Quantification of the long-term of steels T91 and 316L in oxygen-containing flowing lead-bismuth eutectic at 550°C, J. Eng. Gas Turb. Power 132 (2010) 082901-1 – 082901-7.
[15] E. Yamaki, K. Ginestar, L. Martinelli, Dissolution mechanism of 316L in lead-bismuth eutectic at 500°C, Corros. Sci. 53 (2011) 3075-3085.
[16] Y. Kurata, Corrosion behaviour of cold-worked austenitic stainless steels in liquid lead-bismuth eutectic, J. Nucl. Mater. 448 (2014) 239-249.
[17] V. Tsisar, C. Schroer, O. Wedemeyer, A. Skrypnik, J. Konys, Corrosion behavior of austenitic steels 1.4970, 316L and 1.4571 in flowing LBE at 450 and 550°C with 10^{-7} mass% dissolved oxygen, J. Nucl. Mater. 454 (2014) 332-342.
[18] M. Roy, L. Martinelli, K. Ginestar, J. Favergeon, Dissolution and oxidation behaviour of various austenitic steels and Ni rich alloys in lead-bismuth eutectic at 520°C, J. Nucl. Mater. 468 (2016) 153-163.
[19] G. Müller, A. Heinzel, J. Konys, G. Schumacher, A. Weisenburger, F. Zimmermann, V. Engelko, A. Rusanov, V. Markov, Behavior of steels in flowing liquid PbBi eutectic alloy at 420-600°C after 4000-7200 h, J. Nucl. Mater. 335 (2004) 163-168.
[20] M. Kondo, M. Takahashi, Metallurgical analysis of a tube ruptured in the lead bismuth corrosion test facility, J. Nucl. Sci. Technol. 43 (2006) 174-178.
[21] C. Schroer, O. Wedemeyer, J. Novotny, A. Skrypnik, J. Konys, Long-term service of austenitic steel 1.4571 as a container material for flowing lead-bismuth eutectic, J. Nucl. Mater. 418 (2011) 8-15.
[22] Y. Kurata, M. Futukawa, S. Saito, Corrosion behavior of steels in liquid lead-bismuth with low oxygen concentrations, J. Nucl. Mater. 373 (2008) 164-178.
[23] D. Sapundjiev, S. Van Dyck, W. Bogaerts, Liquid metal corrosion of T91 and A316L materials in Pb-Bi eutectic at temperatures 400-600°C, Corros. Sci. 48 (2006) 577-594.
[24] Ph. Deloffre, A. Terlain, F. Barbier, Corrosion and deposition of ferrous alloys in molten lead-bismuth, J. Nucl. Mater. 301 (2002) 35-39.
[25] G. Benamati, C. Fazio, H. Piankova, A. Rusanov, Temperature effect on the corrosion mechanism of austenitic and martensitic steels in lead-bismuth, J. Nucl. Mater. 301 (2002) 23-27.
[26] F. Gnecco, E. Ricci, C. Bottino, A. Passerone, Corrosion behaviour of steels in lead-bismuth at 823 K, J. Nucl. Mater. 335 (2004) 185-188.
[27] Y. Kurata, M. Futakawa, Excellent corrosion resistance of 18Cr-20Ni-5Si steel in liquid Pb-Bi, J. Nucl. Mater. 325 (2004) 217-222.
[28] Y. Kurata, Corrosion experiments and materials developed for the Japanese HLM systems, J. Nucl. Mater. 415 (2011) 254-259.

[29] Y. Kurata, S. Saito, Temperature dependence of corrosion of ferritic/martensitic and austenitic steels in liquid lead-bismuth eutectic, Mater. Trans. 50 (2009) 2410-2417.
[30] Y. Kurata, M. Futukawa, S. Saito, Comparison of the corrosion behavior of austenitic and ferritic/martensitic steels exposed to static liquid Pb-Bi at 450 and 550°C, J. Nucl. Mater. 343 (2005) 333-340.
[31] F.J. Martín-Muñoz, L. Soler-Crespo, D. Gómez-Briceño, Assessment of the influence of surface finishing and weld joints on the corrosion/oxidation behaviour of stainless steels in lead bismuth eutectic, J. Nucl. Mater. 416 (2011) 80-86.
[32] O. Yeliseyeva, V. Tsisar, G. Benamati, Influence of temperature on the interaction mode of T91 and AISI 316L steels with Pb-Bi melt saturated by oxygen, Corros. Sci. 50 (2008) 1672-1683.
[33] F.J. Martín, L. Soler, F. Hernández, D. Gómez-Briceño, Oxide layer stability in lead-bismuth at high temperature, J. Nucl. Mater. 335 (2004) 194-198.
[34] Ph. Deloffre, A. Terlain, Influence of Zn as a spallation product on the behaviour of martensitic steel T91 and austenitic steel 316L in liquid Pb-Bi, J. Nucl. Mater. 335 (2004) 244-248.
[35] G. Benamati, A. Gessi, P-Z. Zhang, Corrosion experiments in flowing LBE at 450°C, J. Nucl. Mater. 356 (2006) 198-202.
[36] A. Gessi, G. Benamati, Corrosion experiments of steels in flowing Pb at 500°C and in flowing LBE at 450°C, J. Nucl. Mater. 376 (2008) 269-273.
[37] K. Kikuchi, Y. Kurata, S. Saito, M. Futakawa, T. Sasa, H. Oigawa, E. Wakai, K. Miura, Corrosion-erosion test of SS316 in flowing Pb-Bi, J. Nucl. Mater. 318 (2003) 348-354.
[38] S. Saito, K. Kikuchi, D. Hamaguchi, M. Tezuka, M. Miyagi, H. Kokawa, S. Watanabe, Corrosion-erosion test of SS316L grain boundary engineering material (GBEM) in lead bismuth flowing loop, J. Nucl. Mater. 431 (2012) 91-96.
[39] F.J. Martín-Muñoz, L. Soler-Crespo, D. Gómez-Briceño, Corrosion behaviour of martensitic and austenitic steels in flowing lead-bismuth eutectic, J. Nucl. Mater. 416 (2011) 87-93.
[40] I.V. Gorynin, G.P. Karzov, V.G. Markov, V.S. Lavrukhin, V.A. Yakovlev, Structural materials for power plants with heavy liquid metals as coolants, in: Proc. Heavy Liquid Metal Coolants in Nuclear Technology (HLMC-98), 1999, Vol. 1, pp. 120-132.
[41] G. Ilinčev, D. Kárník, M. Paulovič, A. Doubková, The impact of the composition of structural steels on their corrosion stability in liquid Pb-Bi at 500 and 400°C with different oxygen concentrations, J. Nucl. Mater. 335 (2004) 210-216.
[42] M. Takahashi, K. Ishikawa, T. Suzuki, S. Yoshida, T. Yano, H. Sekimoto, N. Sawada, K. Hata, S. Qiu, M. Imai, Experimental study on flow technology and steel corrosion of lead-bismuth, in: Proc. 10th International Conference on Nuclear Engineering (ICONE 10-22226), 2002, Vol. 2, pp. 607-615.
[43] M. Kondo, M. Takahashi, N. Sawada, K. Hata, Corrosion of steels in lead-bismuth flow, J. Nucl. Sci. Technol. 43 (2006) 107-116.

[44] M. Takahashi, M. Kondo, N. Sawada, K. Hata, Corrosion of steels in lead-bismuth flow, in: Proc. Global 2003 Int'l Conf. Nuclear Science and Technology, Nov. 16-23, 2003, New Orleans, LA, USA.
[45] M. Kondo, M. Takahashi, T. Suzuki, K. Ishikawa, K. Hata, S. Qiu, H. Sekimoto, Metallurgical study on erosion and corrosion behaviors of steels exposed to liquid lead-bismuth flow, J. Nucl. Mater. 343 (2005) 349-359.
[46] A. Doubková, F. Di Gabriele, P. Brabec, E. Keilová, Corrosion behavior of steels in flowing lead-bismuth under abnormal conditions, J. Nucl. Mater. 376 (2008) 260-264.
[47] J. Zhang, N. Li, Y. Chen, A.E. Rusanov, Corrosion behaviors of US steels in flowing lead-bismuth eutectic (LBE), J. Nucl. Mater. 336 (2005) 1-10.
[48] F. Balbaud-Celerier, P. Deloffre, A. Terlain, A. Rusanov, Corrosion of metallic materials in flowing liquid lead-bismuth, J. Phys. IV 12 (2002) Pr8-177 – Pr8-190.
[49] G. Müller, A. Heinzel, J. Konys, G. Schumacher, A. Weisenburger, F. Zimmermann, V. Engelko, A. Rusanov, V. Markov, Results of steel corrosion tests in flowing liquid Pb/Bi at 420-600°C after 2000 h, J. Nucl. Mater. 301 (2002) 40-46.
[50] N. Li, Active control of oxygen in molten lead-bismuth eutectic to prevent steel corrosion and coolant contamination, J. Nucl. Mater. 300 (2002) 73-81.
[51] J. Zhang, N. Li, Review of the studies on fundamental issues in LBE corrosion, J. Nucl. Mater. 373 (2008) 351-377.
[52] K. Lambrinou, V. Koch, G. Coen, J. Van den Bosch, C. Schroer, Corrosion scales on various steels after exposure to liquid lead–bismuth eutectic, J. Nucl. Mater. 450 (2014) 244-255.
[53] J. Van den Bosch, A. Almazouzi, EUROTRANS-DEMETRA-Task 4.1.2: Reference materials procurement, dispatching and characterisation, Restricted Contract Report SCK•CEN-R-4197, 2005.
[54] Metals Handbook, Desk Edition, second ed., J.R. Davis, Davis & Associates (Eds.), ASM International, 1998, pp. 153-173 and 375-379.
[55] G. Krauss, Steels: Processing, structure, and performance, fourth ed., ASM International®, Ohio, USA, 2008, pp. 161-175 and 510-512.
[56] R.E. Schramm, R.P. Reed, Stacking fault energies of seven commercial austenitic stainless steels, Metall. Trans. A 6 (1975) 1345-1351.
[57] J. Lim, A. Mariën, K. Roseel, A. Aerts, J. Van den Bosch, Accuracy of potentiometric oxygen sensors with Bi/Bi_2O_3 reference electrode for use in liquid LBE, J. Nucl. Mater. 429 (2012) 270-275.
[58] J. Lim, G. Manfredi, A. Mariën, J. Van den Bosch, Performance of potentiometric oxygen sensors with LSM-GDC composite electrode in liquid LBE at low temperatures, Sensor. Actuator. B 188 (2013) 1048-1054.

[59] V. Tsisar, C. Schroer, O. Wedemeyer, A. Skrypnik, J. Konys, Long-term corrosion of austenitic steels in flowing LBE at 400°C and 10^{-7} mass% dissolved oxygen in comparison with 450 and 550°C, J. Nucl. Mater. 468 (2016) 305-312.
[60] N. Marié, K. Wolski, M. Biscondi, Grain boundary penetration of nickel by liquid bismuth as a film of nanometric thickness, Scripta Mater. 43 (2000) 943-949.
[61] N. Marié, K. Wolski, M. Biscondi, Intergranular penetration and embrittlement of solid nickel through bismuth vapour condensation at 700°C, J. Nucl. Mater. 296 (2001) 282-288.
[62] K. Wolski, V. Laporte, Grain boundary diffusion and wetting in the analysis of intergranular penetration, Mater. Sci. Eng. A 495 (2008) 138-146.
[63] D. Empl, L. Felberbaum, V. Laporte, D. Chatain, A. Mortensen, Dihedral angles in Cu-1 wt.% Pb: grain boundary energy and grain boundary triple line effects, Acta Mater. 57 (2009) 2527-2537.
[64] L. Martinelli, Nickel solubility limit in liquid lead-bismuth eutectic, J. Nucl. Mater. 400 (2010) 232-239.
[65] S. Gossé, Thermodynamic assessment of solubility and activity of iron, chromium, and nickel in lead bismuth eutectic, J. Nucl. Mater. 449 (2014) 122-131.
[66] M. Mizouchi, Y. Yamazaki, Y. Iijima, K. Arioka, Low temperature grain boundary diffusion of chromium in SUS316 and 316L stainless steels, Mater. Trans. 45 (2004) 2945-2950.
[67] P. Hosemann, D. Frazer, E. Stergar, K. Lambrinou, Twin boundary-accelerated ferritization of austenitic stainless steels in liquid lead-bismuth eutectic, Scripta Mater. 118 (2016) 37-40.
[68] J.M. Barsom, S.T. Rolfe, Fracture and fatigue control in structures – Applications in fracture mechanics, third ed., ASTM Manual Series: MNL 41, ASTM International, West Conshohocken, USA, 1999, pp. 10-14.
[69] K. Lambrinou, Factors affecting the bulk embrittlement of Pb-free solder joints, in: G. Grossmann, Ch. Zardini (Eds.), ELFNET Handbook on Failure Mechanisms & Testing Methods for Lead-Free Solder Interconnects, Springer, 2011, pp. 19-63.
[70] K. Farrell, T.S. Byun, Tensile properties of candidate SNS target container materials after proton and neutron irradiation in the LANSCE accelerator, J. Nucl. Mater. 296 (2001) 129-138.
[71] S.A. Maloy, M.R. James, W.R. Johnson, T.S. Byun, K. Farrell, M.B. Toloczko, Comparison of fission neutron and proton/spallation neutron irradiation effects on the tensile behaviour of type 316 and 304 stainless steel, J. Nucl. Mater. 318 (2003) 283-291.
[72] C. Pokor, Y. Brechet, P. Dubuisson, J.-P. Massoud, X. Averty, Irradiation damage in 304 and 316 stainless steels: experimental investigation and modelling. Part II: Irradiation induced hardening, J. Nucl. Mater. 326 (2004) 30-37.
[73] J.D. Elen, P. Fenici, Fast neutron irradiation hardening of austenitic stainless steel at 250°C, J. Nucl. Mater. 191-194 (1992) 766-770.
[74] J. Van den Bosch, P. Hosemann, A. Almazouzi, S.A. Maloy, Liquid metal embrittlement of silicon enriched steel for nuclear applications, J. Nucl. Mater. 398 (2010) 116-121.

[75] G. Coen, J. Van den Bosch, A. Almazouzi, J. Degrieck, Investigation of the effect of lead-bismuth eutectic on the fracture properties of T91 and 316L, J. Nucl. Mater. 398 (2010) 122-128.
[76] T. Auger, G. Lorang, Liquid metal embrittlement susceptibility of T91 steel by lead-bismuth, Scripta Mater. 52 (2005) 1323-1328.

FIGURE 1

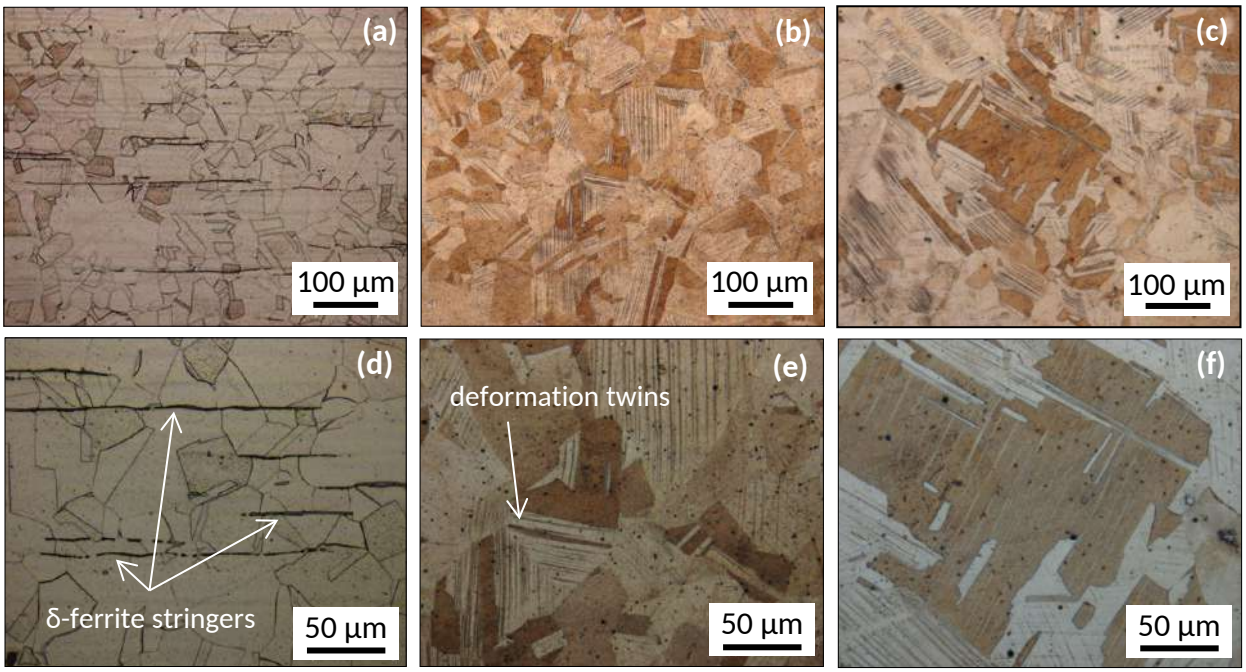

Fig. 1. LOM images of etched cross-sections of the as-received 316L steel heats: (a, d) 316LSA, (b, e) 316LH1, and (c, f) 316LH2.

FIGURE 2

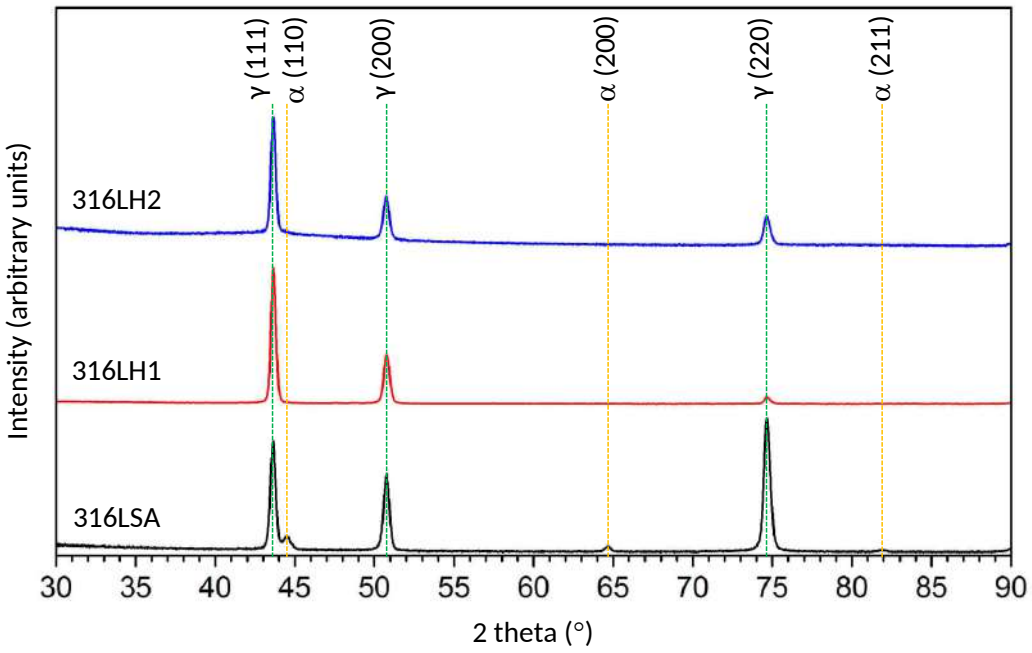

Fig. 2. XRD patterns of the as-received 316L steel heats: the main phase is γ-Fe (austenite; *fcc*, $Fm\bar{3}m$), while a small fraction of α-Fe (α-ferrite; *bcc*, $Im\bar{3}m$) is detected only in the 316LSA heat.

FIGURE 3

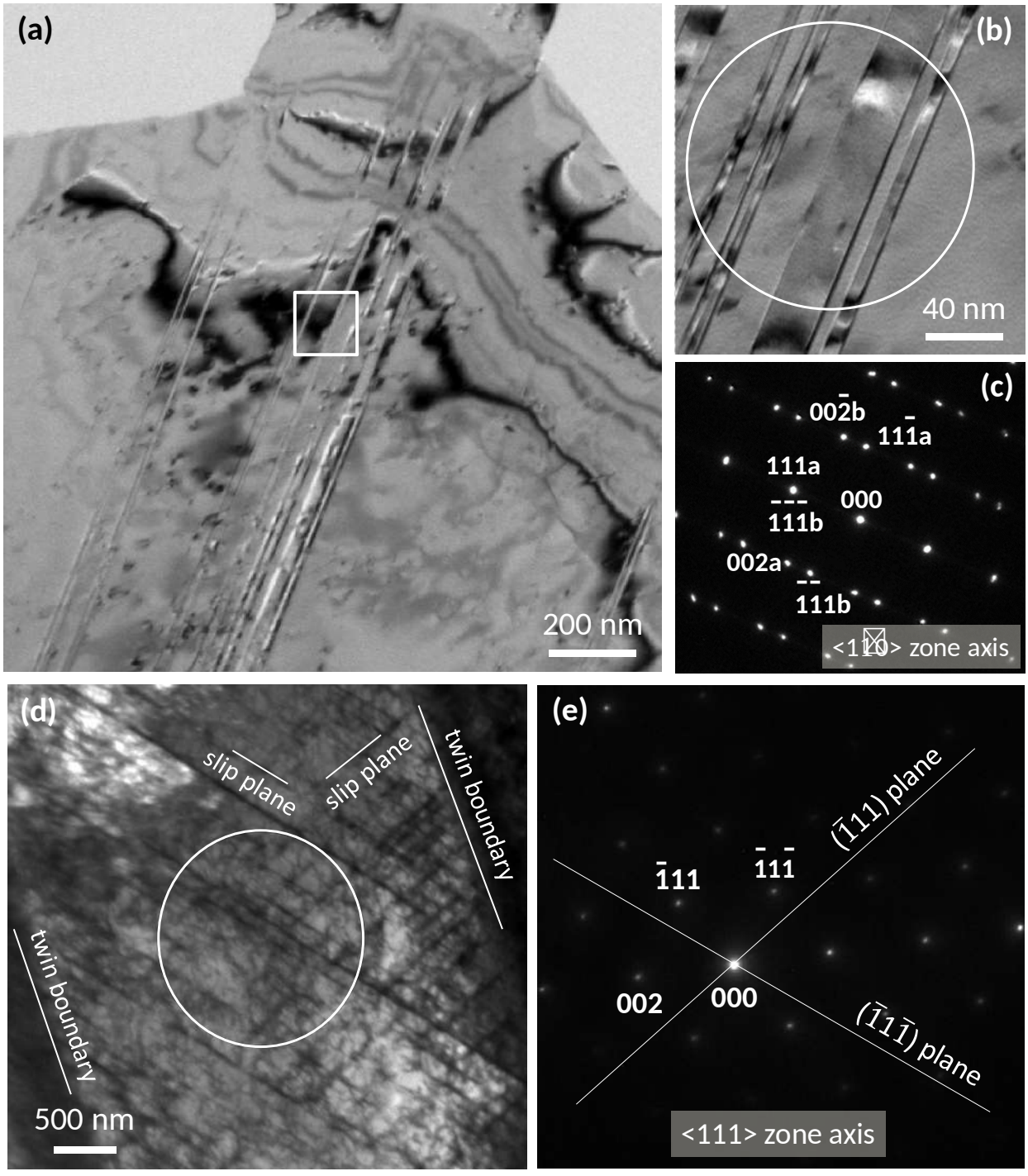

Fig. 3. TEM analysis of defects introduced in the 316LH2 steel during cold deformation. (a) BF image of fine deformation twin laths. (b) Magnified BF image of the framed area in Fig. 3a. (c) Selected area diffraction pattern (SADP) of the twin laths inside the circle in Fig. 3b. (d) BF image of dislocation pile-up on the $\{\bar{1}11\}$ and $\{1\bar{1}1\}$ slip planes in a large twinless zone between two twin boundaries. (e) SADP of the circled area in Fig. 3d.

FIGURE 4

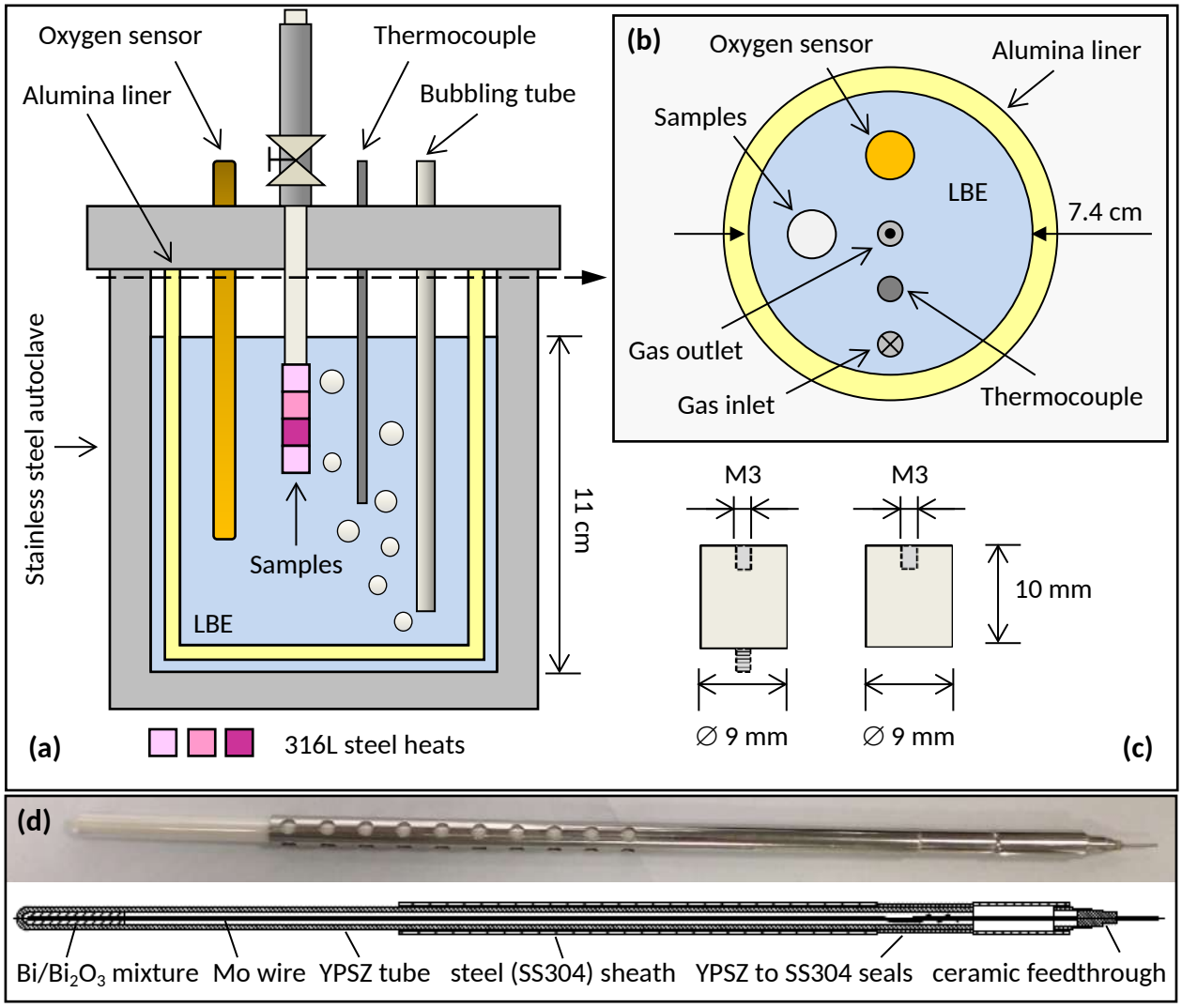

Fig. 4. (a) Experimental setup used for the exposure of 316L steels to oxygen-poor, static LBE. (b) Cross-section just under the lid, showing the relative position of the alumina liner to that of the setup inserts: large openings (∅ 12 mm) for samples and oxygen sensor; small openings (∅ 6 mm) for gas inlet/outlet tubing and thermocouple. (c) Specimen geometry and dimensions. (d) Electrochemical oxygen sensor (Bi/Bi_2O_3 reference electrode) used during the steel exposure.

FIGURE 5

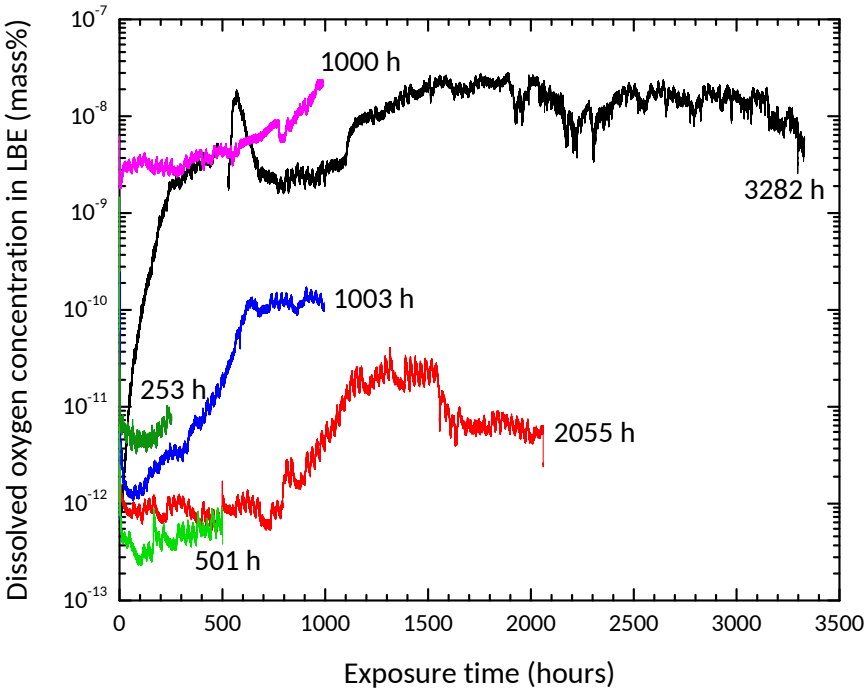

Fig. 5. Concentration of dissolved oxygen in liquid LBE during 316L steel testing at 500°C. The maximum monitored oxygen concentration was 2.2×10^{-8} mass% (end of 1000 h-long exposure).

FIGURE 6

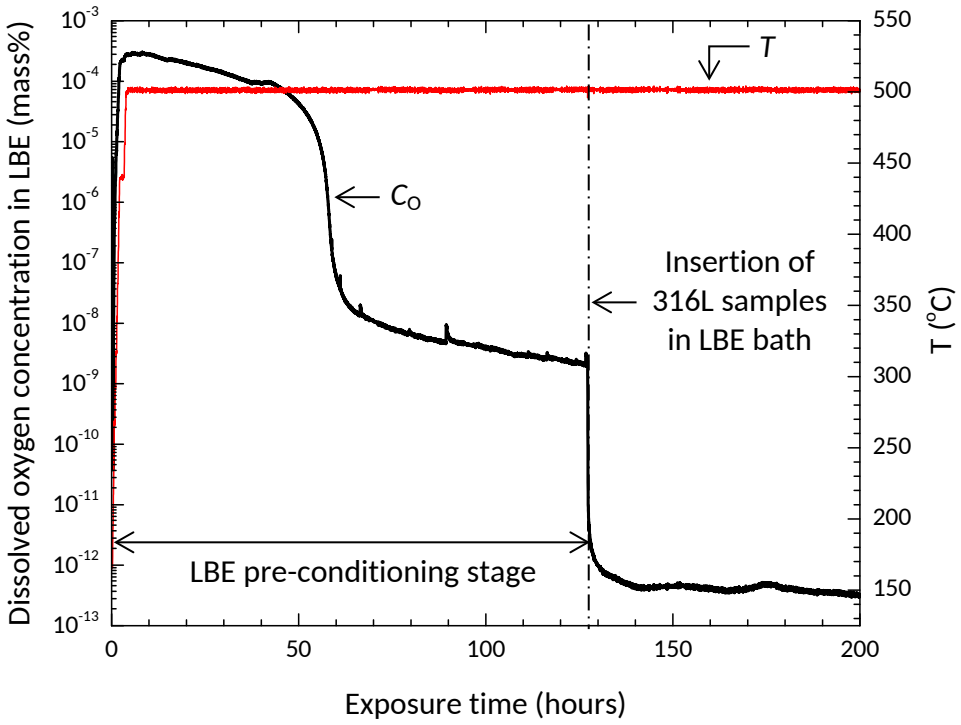

Fig. 6. Temperature (T) and LBE oxygen concentration (C_O) profiles during 316L steel testing at 500°C for 501 h. Purging with Ar-5%H_2 during LBE pre-conditioning lowers C_O below 10^{-8} mass%, while the immersed samples act as oxygen getters, further lowering C_O below 10^{-12} mass%.

FIGURE 7

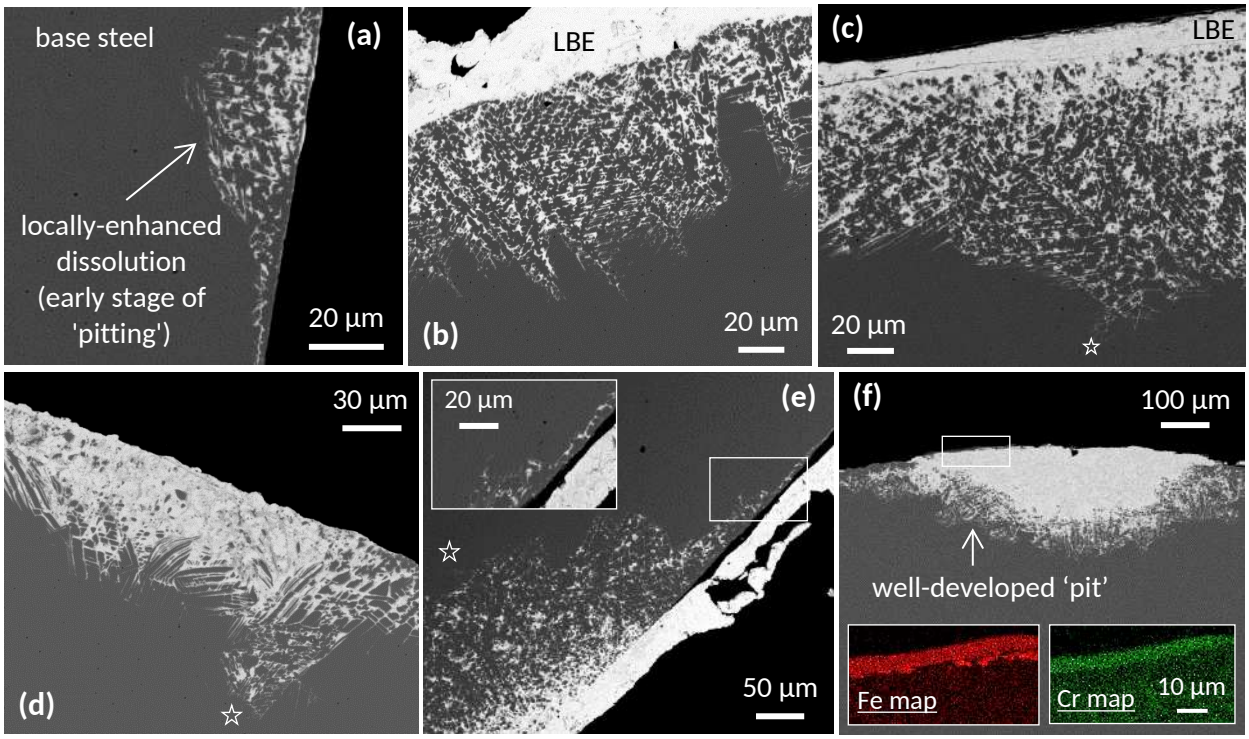

Fig. 7. Backscattered electron (BSE) images of 316LH1 samples exposed for: (a) 253 h – locally-enhanced dissolution (max depth: 33 µm); (b) 501 h – variable dissolution depth (25-100 µm); (c) 1003 h – max dissolution depth: 125 µm (star); (d) 1000 h – max dissolution depth: 91 µm (star); (e) 2055 h – non-uniform dissolution depth, from few grains (magnified inset) to over 185 µm (star); (f) 3282 h – locally-enhanced dissolution leads to the formation of a 'pit' of ~258 µm. EDS elemental mapping shows FeCr-containing oxide scale remnants on top of the ‘pit’ (frame).

FIGURE 8

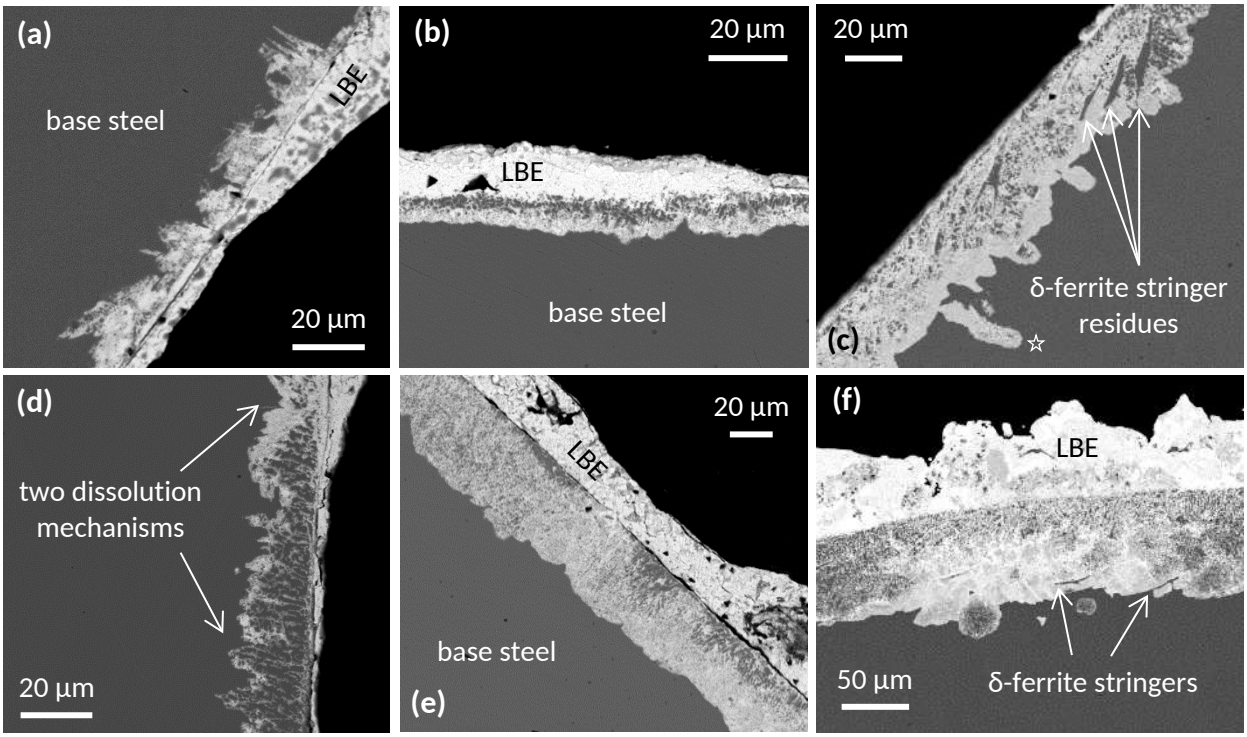

Fig. 8. BSE images of 316LSA samples exposed for: (a) 253 h – variable dissolution depth (10-20 µm); (b) 501 h – variable dissolution depth (7-12 µm); (c) 1003 h – the dissolution depth reaches locally 54 µm (star), δ-ferrite stringers residues; (d) 1000 h – variable dissolution depth (10-27 µm); (e) 2055 h – uniform dissolution zone (30-41 µm); (f) 3282 h – well-developed dissolution zone (62-92 µm), nodular dissolution front perturbations, δ-ferrite stringer residues.

FIGURE 9

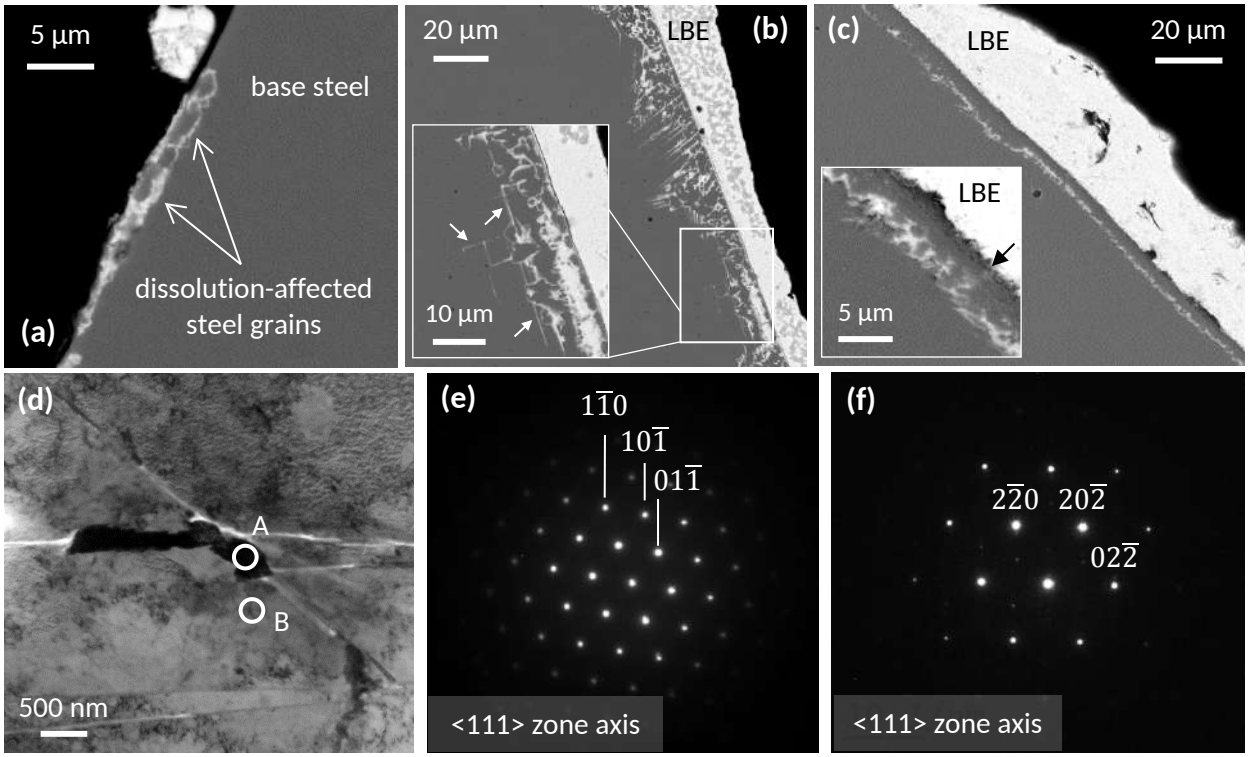

Fig. 9. BSE images of the onset of LBE dissolution attack. (a) 316LSA sample (253 h): only few sub-surface grains are affected, shallow attack (1-2 µm). (b) 316LH1 sample (253 h): limited attack (max 27 µm), LBE penetration intergranular and along certain planes (arrows). (c) 316LH2 sample (1003 h): only the sub-surface layer of grains is affected (max ~8 µm), LBE ingress via grain boundaries accessing the surface (arrow). (d) TEM BF image of a ferritized grain inside the steel bulk. (e) SADP of area A: ferrite (*bcc*, *a*=2.9 Å). (f) SADP of area B: austenite (*fcc*, *a*=3.5 Å).

FIGURE 10

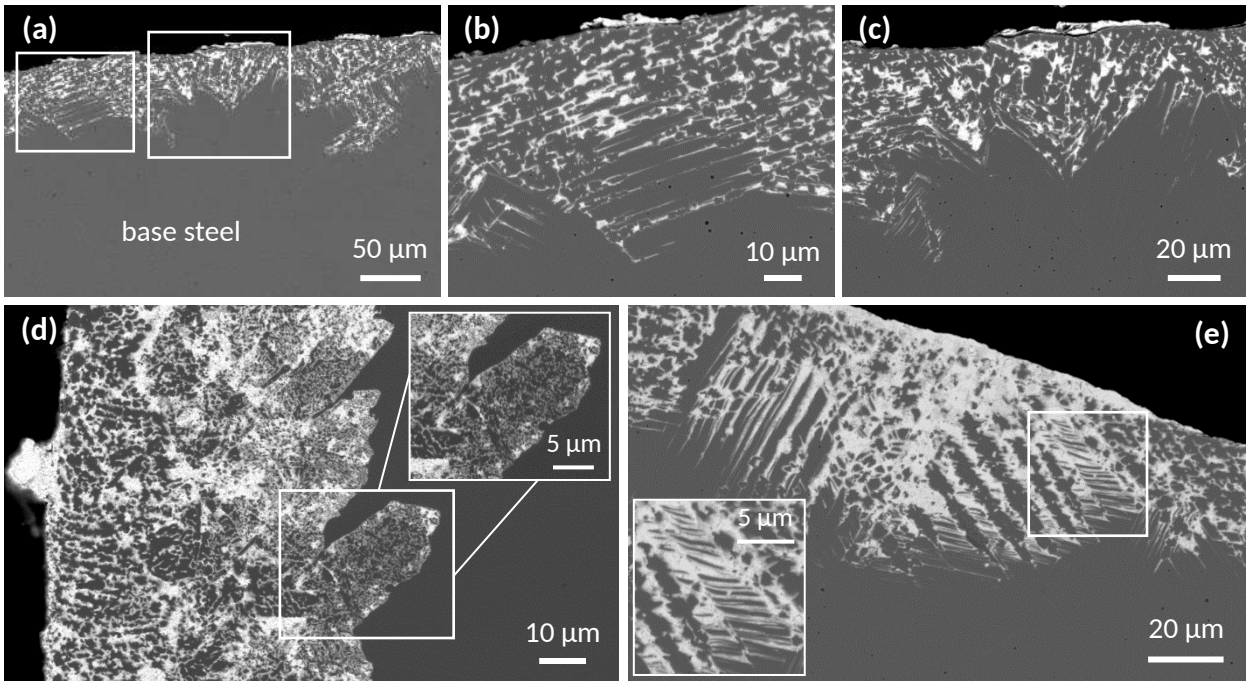

Fig. 10. BSE images of the progress of LBE dissolution attack. (a-c) 316LH1 sample (1003 h): LBE penetrates into the steel following preferred paths in the steel microstructure: overview (a) and details (b-c). (d) 316LSA sample (3282 h): the dissolution front protuberances appear parallel, following the local steel microstructure. (e) 316LH1 sample (1000 h): the intricate network of LBE penetrations shows the interplay of the dissolution process with the steel microstructure.

FIGURE 11

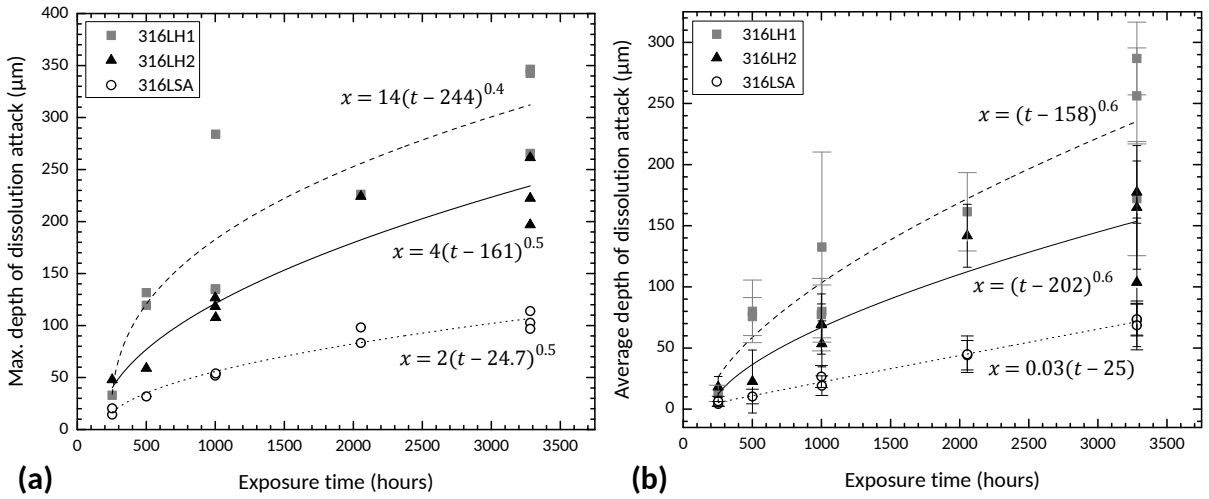

Fig. 11. (a) Maximum and (b) average depth of LBE dissolution attack as function of the exposure time for the 316L steels exposed to oxygen-poor, static LBE at 500°C in this study.

FIGURE 12

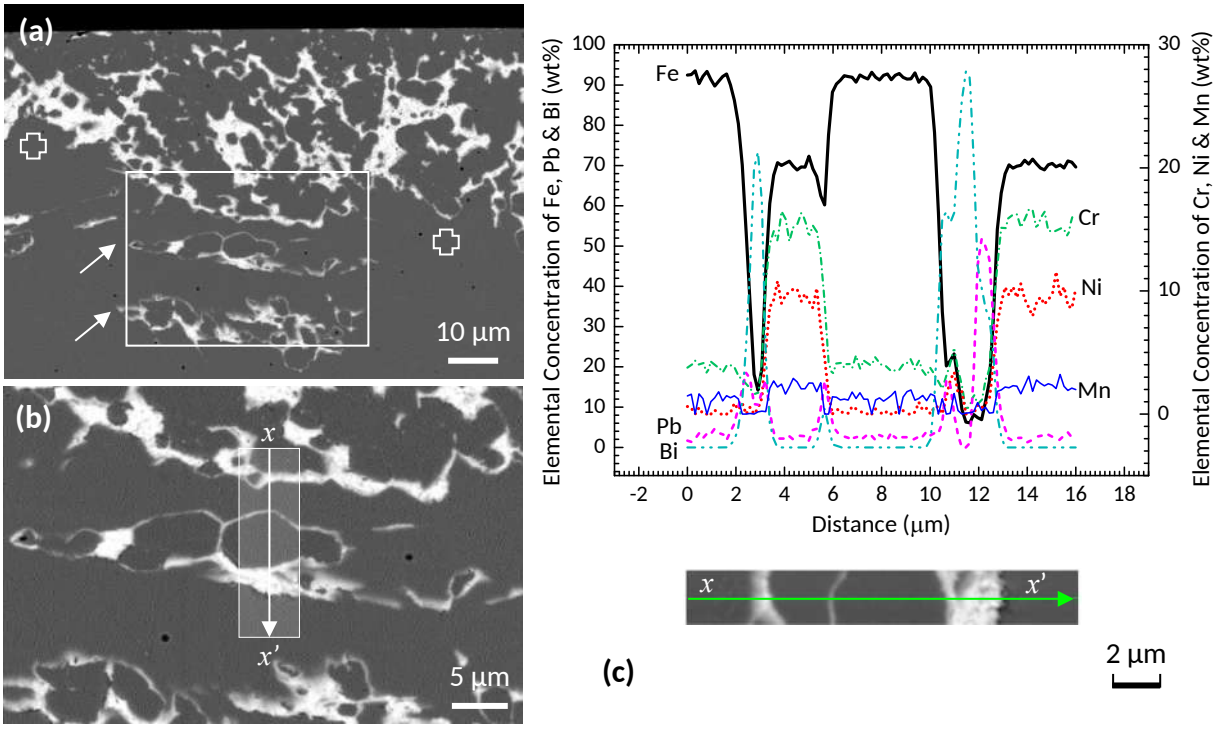

Fig. 12. BSE images of the progress of LBE dissolution attack in a 316LH1 sample (3282 h): (a) this cross-section shows 'islands' of attacked grains (arrows) at a distance of few µm from the main dissolution front (crosses). (b) Detail of one 'island'. (c) EDS line scan across an attacked grain: selective leaching of Ni, Mn and Cr; Fe enrichment; Pb and Bi grain boundary decoration.

FIGURE 13

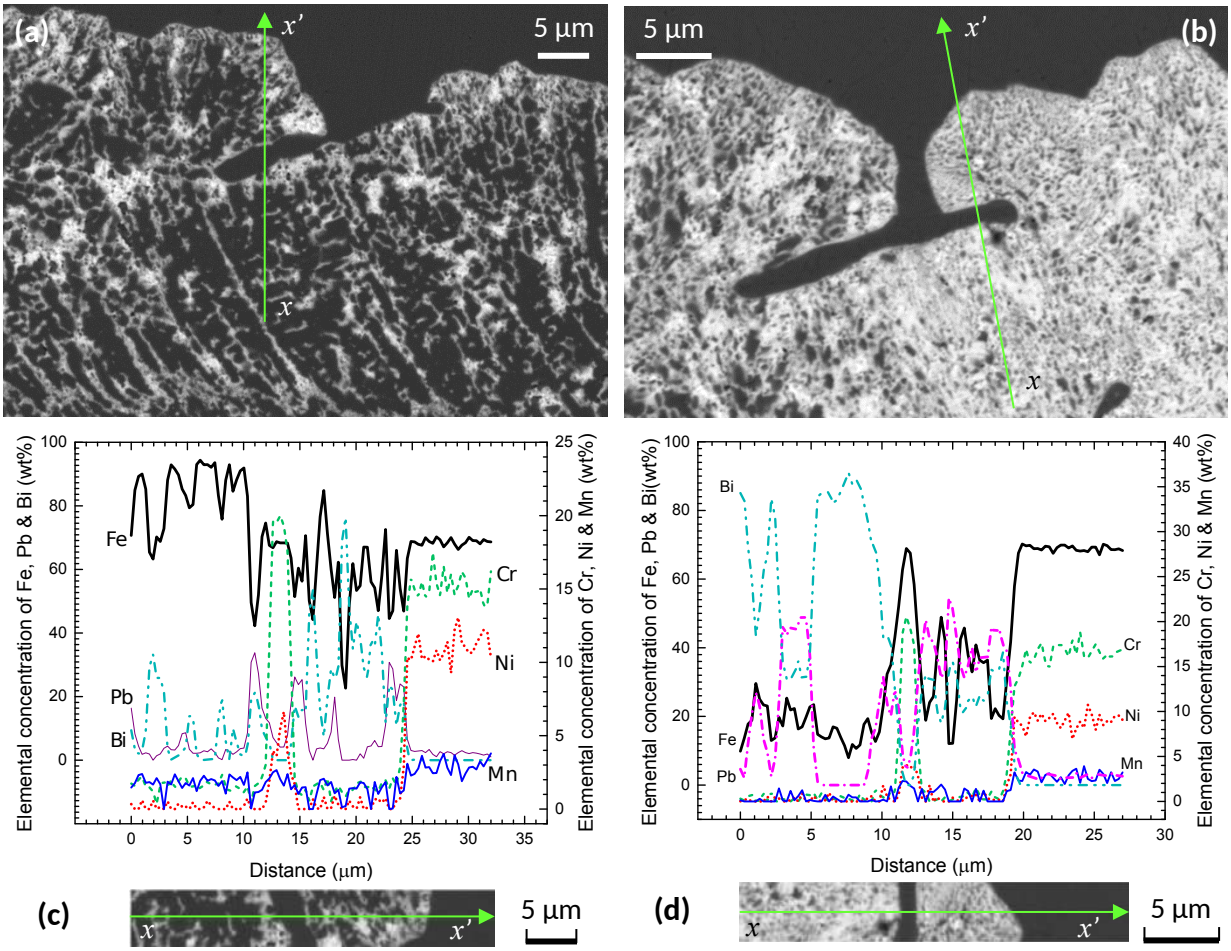

Fig. 13. BSE images and EDS line scans of two sites situated at a distance of ~45 µm at the dissolution front of a 316LSA sample (3282 h): (a, c) selective leaching of Ni, Mn and Cr; (b, d) non-selective leaching of all elements (Ni, Mn, Cr and Fe).

FIGURE 14

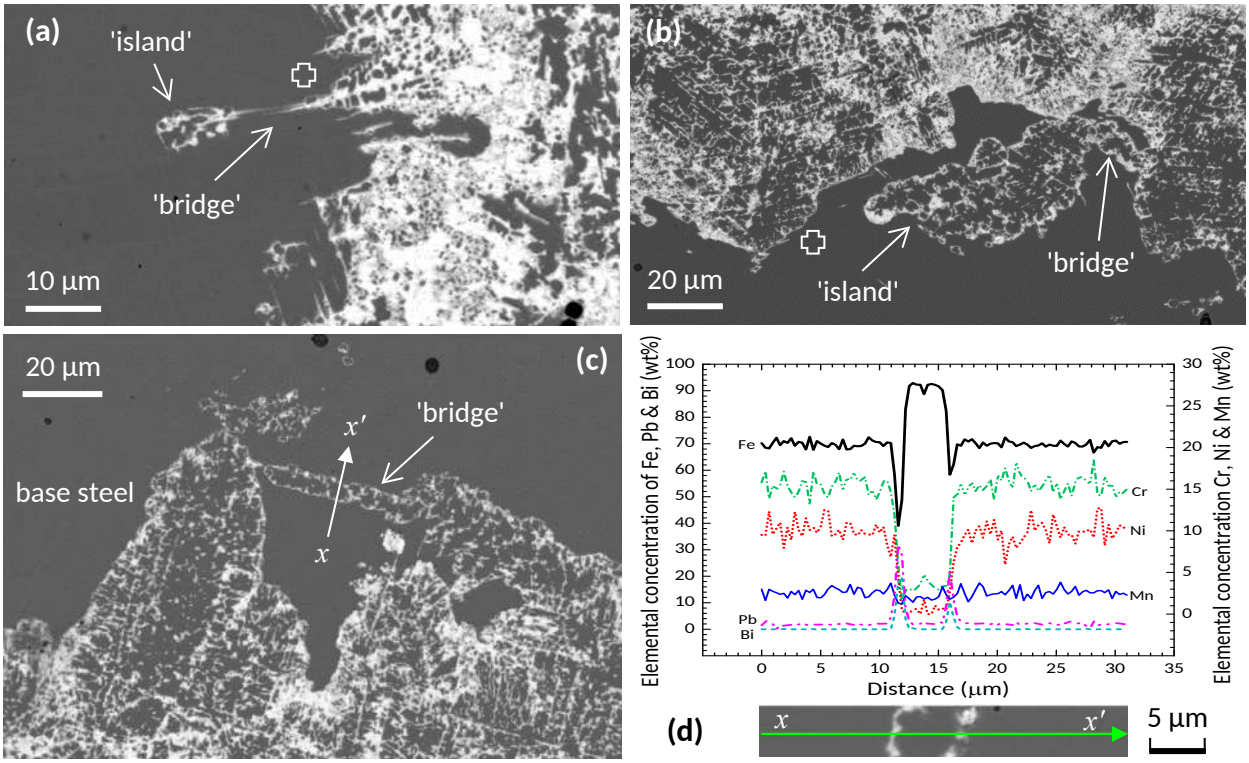

Fig. 14. BSE images of 'bridges' between the main dissolution front (crosses) and 'islands' of attacked grains: (a) 316LH2 sample (1000 h), (b) 316LH2 sample (3282 h). (c-d) 316LH2 sample (3282 h): 'bridge' between unconnected areas in the dissolution-affected zone and EDS line scan: selective leaching of Ni, Mn and Cr; Fe enrichment; Pb and Bi grain boundary decoration.

FIGURE 15

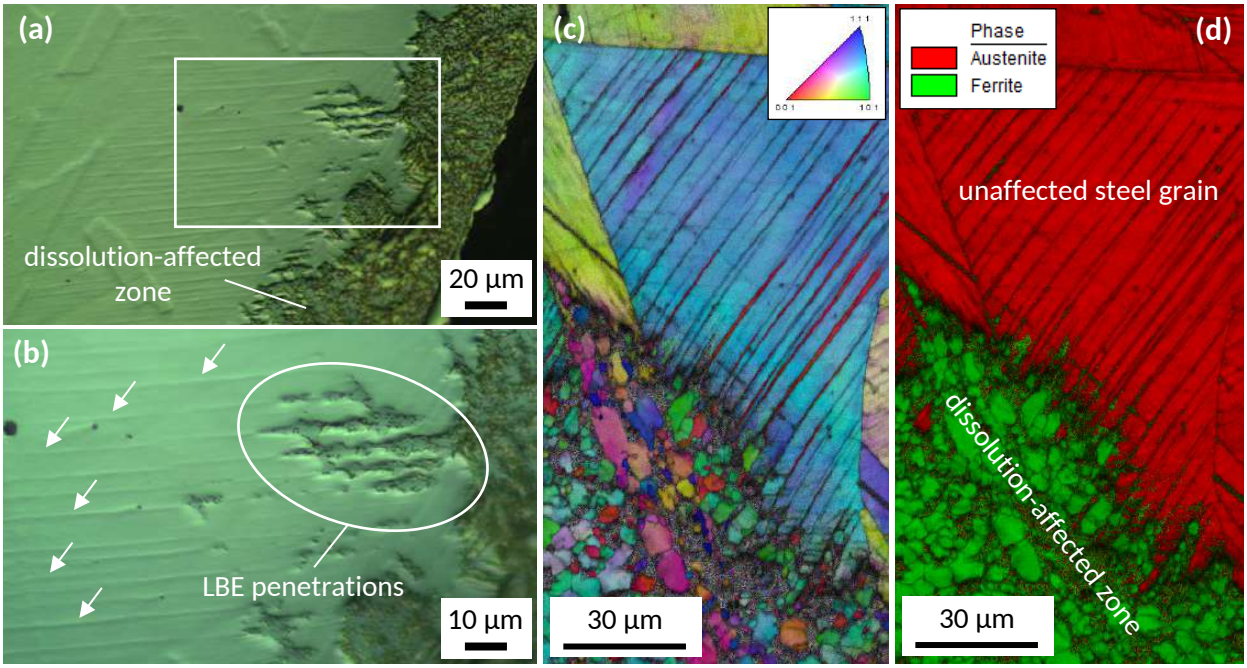

Fig. 15. LOM images of an OPS-polished cross-section of a 316LH2 sample (1000 h). (a) Overview and (b) detail of parallel steel grain striations (arrows) that guide locally the LBE penetration. (c-d) EBSD data from a 316LH1 sample (3282 h): orientation map showing LBE penetration along closely-spaced grain striations (c), and phase map showing ferritization of the dissolution-affected zone, while the unaffected steel grains are austenitic (d).

FIGURE 16

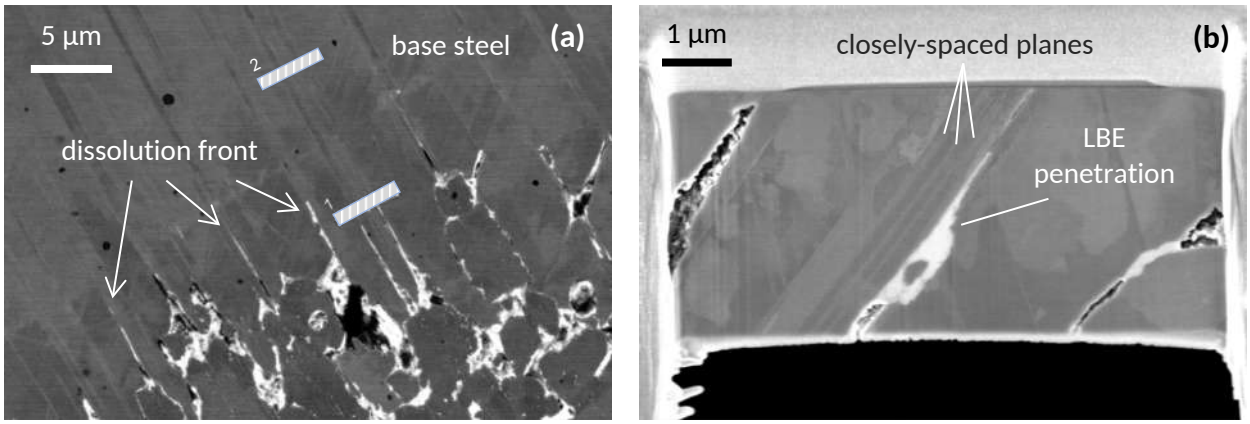

Fig. 16. Thin foil preparation by FIB from the steel grain in Fig. 15. (a) BSE image of two areas of interest for thin foil extraction: area 1 is situated close to LBE penetration tips, and area 2 is in the unaffected part of the grain. (b) SEM image of the thin foil from area 1: a set of closely-spaced, parallel planes is adjacent to an LBE penetration.

FIGURE 17

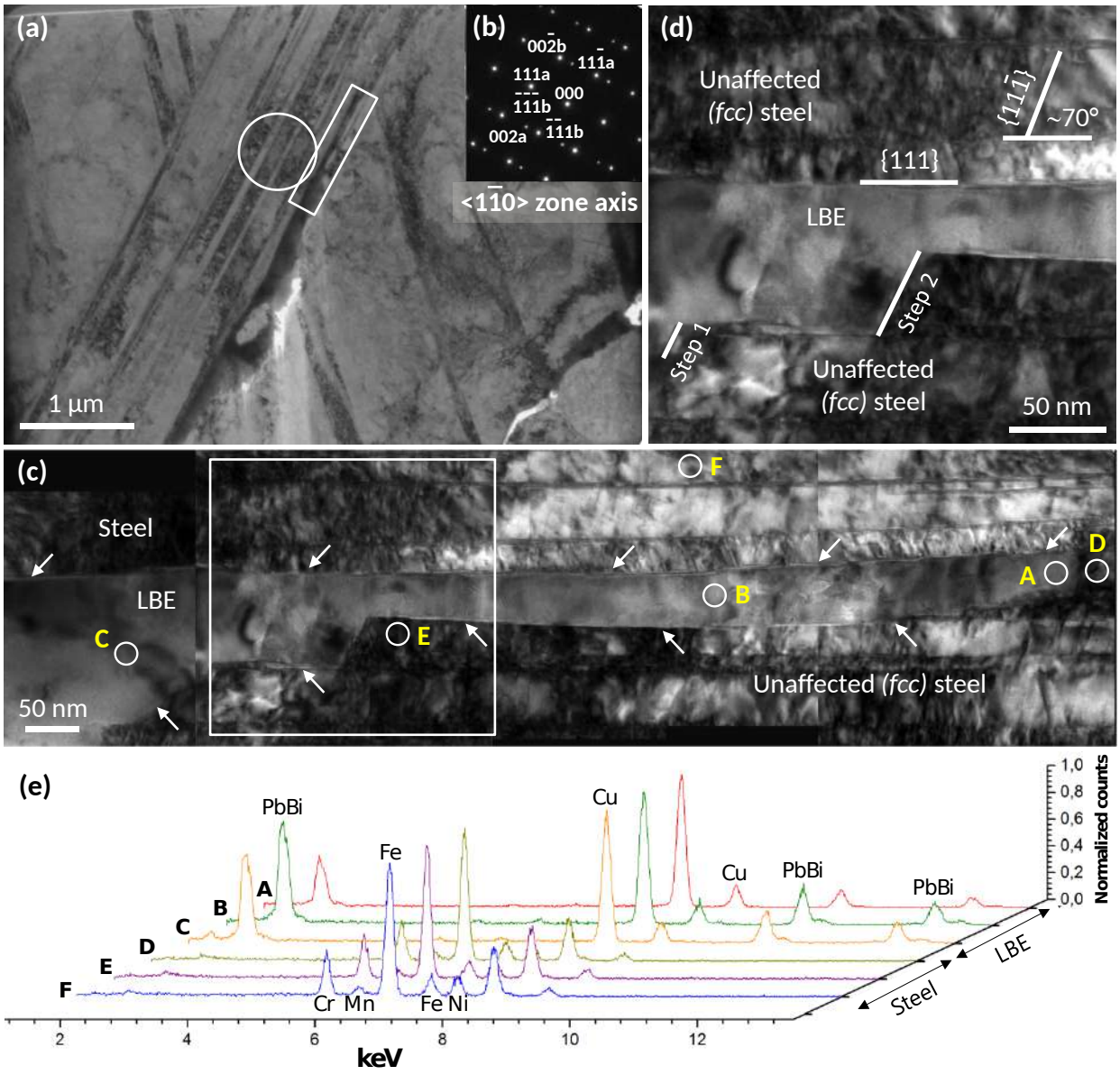

Fig. 17. (a) BF image of the FIB foil in Fig. 16b. (b) SADP of the twin laths in the circle of Fig. 17a along the <1$\bar{1}$0> zone axis, showing typical twin spot splitting. (c) BF image of the rectangle in Fig. 17a: LBE penetration occurs via a stepwise removal of steel layers. Arrows outline the border between unaffected steel and LBE penetration. (d) BF image of the rectangle in Fig. 17c: higher magnification of the stepwise removal of steel layers by LBE. (e) Results of EDS point analysis on LBE sites (A-C) and steel sites (D-F).

FIGURE 18

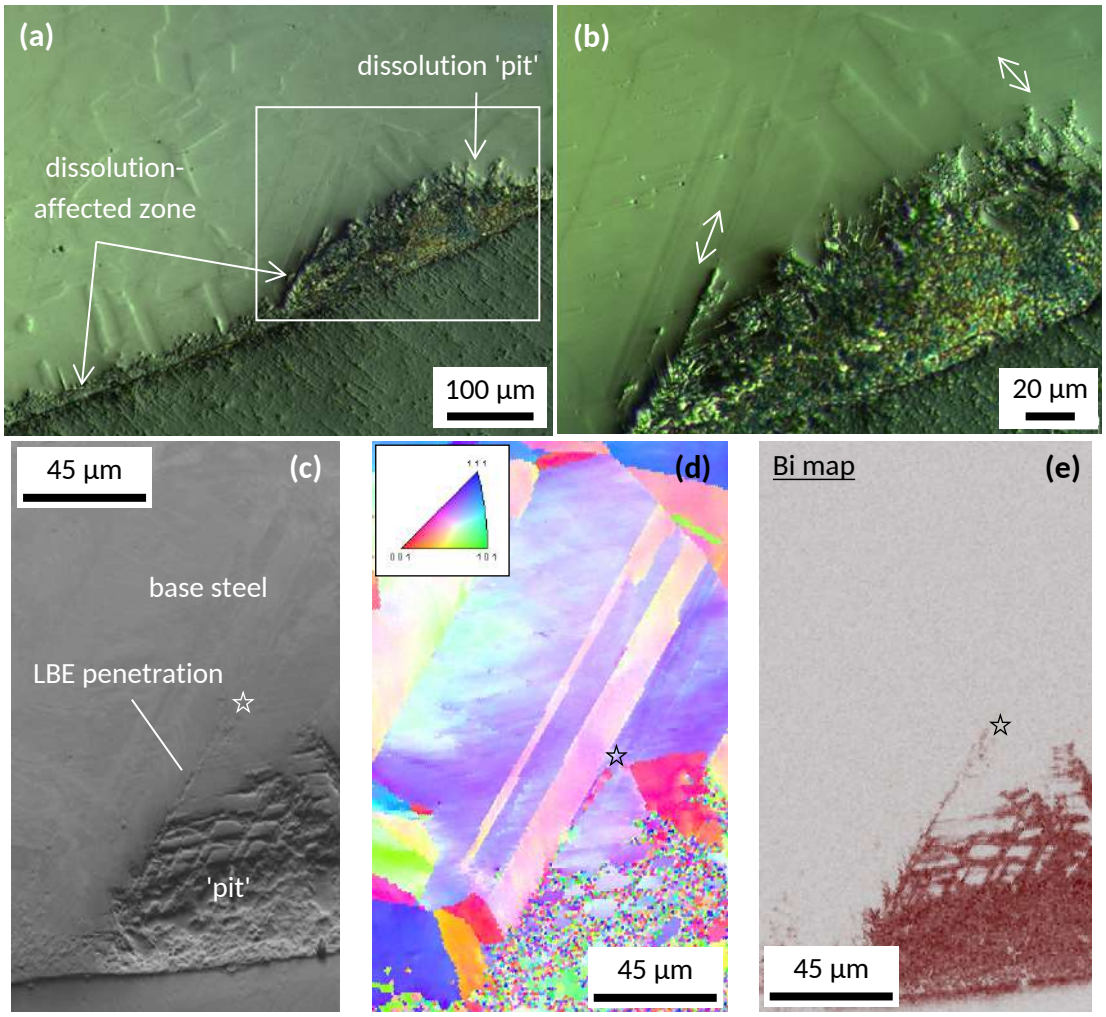

Fig. 18. LOM images of an OPS-polished cross-section of a 316LH2 sample (1000 h). (a) The depth of dissolution attack in this area is < 30 µm, but exceeds 80 µm at the 'pit'. (b) The 'pit' growth is guided by the convergence of certain boundaries in the steel (arrows). (c) SEM image of the left 'pit' corner. (d) EBSD orientation map: twin boundary guiding LBE penetration (star) into the steel. (c) EDS map showing the presence of Bi in the dissolution-affected zone.

FIGURE 19

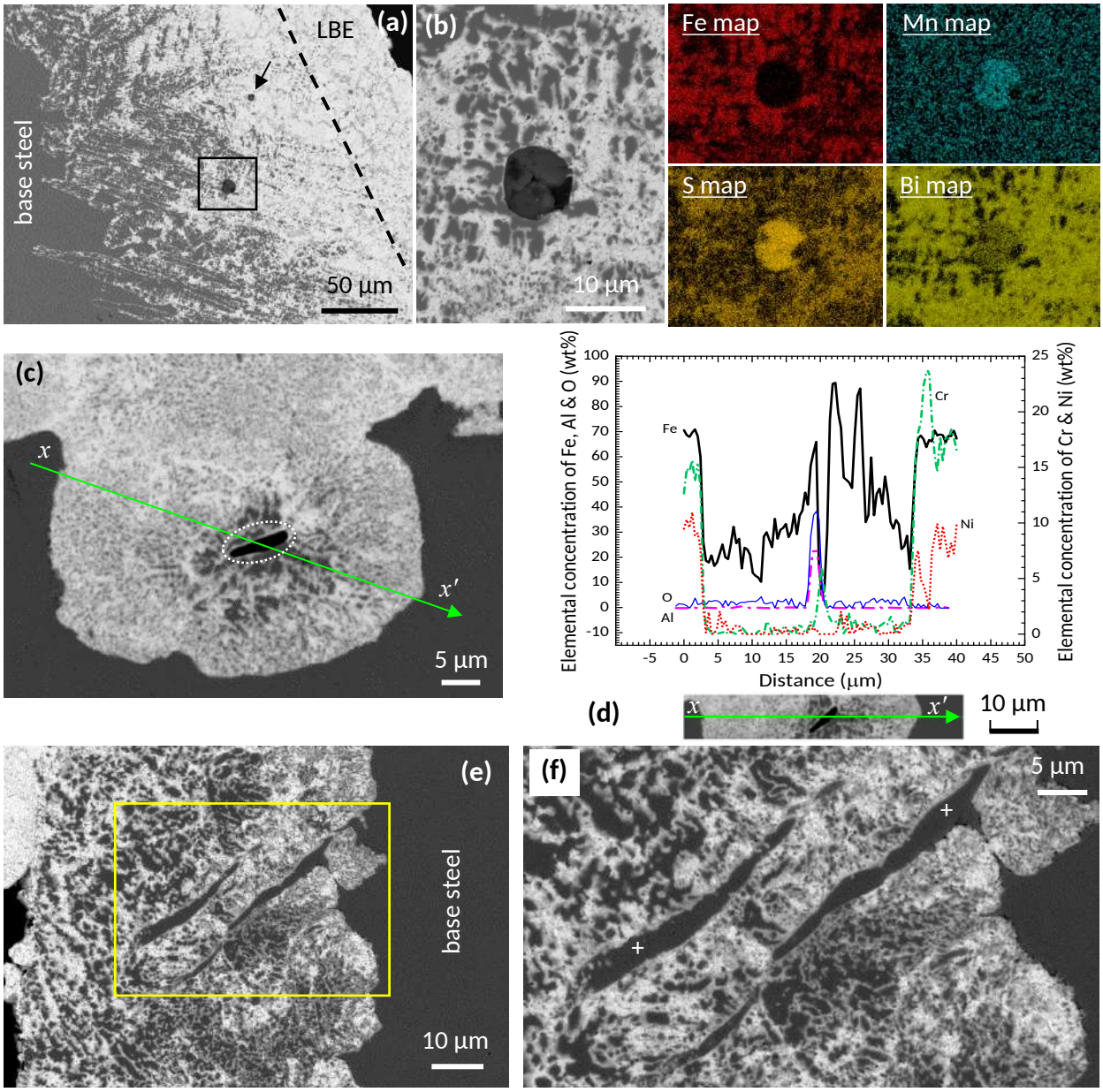

Fig. 19. Unaffected MnS precipitates in a 316LH2 sample (3282 h): (a) the largest lies far from the original specimen surface (dashed line); a small one is pointed by an arrow. (b) Detail of the large precipitate; EDS elemental mapping shows that the precipitate is MnS. (c) Unaffected oxide precipitate in a 316LSA sample (3282 h). (d) EDS line scan shows that the precipitate is an Al-rich oxide. Unaffected δ-ferrite stringers in a 316LSA sample (3282 h): (e) the stringers are clearly visible in the dissolution-affected zone. (f) Detail of the δ-ferrite stringers (crosses).

FIGURE 20

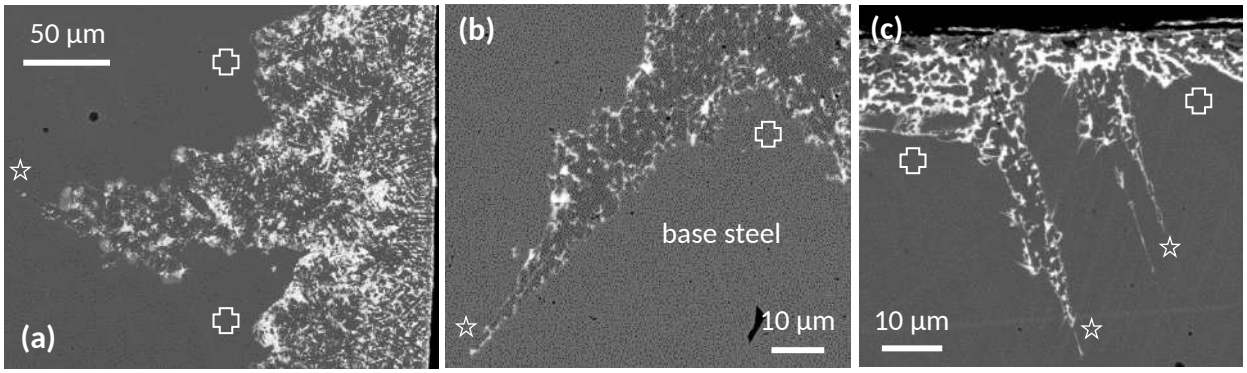

Fig. 20. BSE images showing that sharp protuberances of the dissolution front (stars) advance the main dissolution front (crosses) locally by: (a) ~150 µm (316LH2 sample; 3282 h), (b) ~77 µm (316LH2 sample; 2055 h), and (c) ~46 µm (316LH2 sample; 501 h).

TABLE 1

Table 1

Comparison of the chemical composition of the 316LSA, 316LH1 and 316LH2 steel heats to the AISI 316L chemical specification. All elemental concentrations are in mass%; the balance is Fe.

Element	316LSA	316LH1	316LH2	AISI 316L
C	0.019	0.028	0.022	≤ 0.03
Si	0.67	0.34	0.51	≤ 0.75
Mn	1.81	1.85	1.58	≤ 2.0
P	0.032	0.033	0.029	≤ 0.045
S	0.004	0.027	0.016	≤ 0.03
Cr	16.73	16.7	16.0	16.0-18.0
Ni	9.97	10.1	10.1	10.0-14.0
Mo	2.05	2.06	2.1	2.0-3.0

Mol, 16/02/2017

Dear Editor,

The Highlights of Manuscript entitled "Dissolution corrosion of 316L austenitic stainless steels in contact with static liquid lead-bismuth eutectic (LBE) at 500°C" may be summarised as follows:

- Dissolution corrosion was more severe in cold-deformed than solution-annealed 316L steels
- LBE penetration occurred along preferential paths in the steel microstructure
- The maximum dissolution rate was inversely proportionate to the depth of dissolution

Sincerely yours,

Dr. Konstantina Lambrinou on behalf of all authors